

The Pennsylvania State University
The Graduate School
Department of Materials Science and Engineering

**DEVELOPMENT OF STABLE HIGH-CAPACITY SILICON-BASED ANODE AND
LITHIUM METAL ANODE FOR LITHIUM-ION BATTERY**

A Dissertation in

Materials Science

by

Qingquan Huang

© 2018 Qingquan Huang

Submitted in Partial Fulfillment
of the Requirements
for the Degree of

Doctor of Philosophy

December 2018

The dissertation of Qingquan Huang was reviewed and approved* by the following:

Donghai Wang
Professor of Mechanical Engineering
Dissertation Advisor
Chair of Committee

Chao-Yang Wang
William E. Diefenderfer Chair of Mechanical Engineering
Professor of Materials Science and Engineering

Adri van Duin
Professor of Mechanical Engineering

Long-qing Chen
Donald W. Hamer Professor of Materials Science and Engineering,
Professor of Engineering Science and Mechanics, and Mathematics,

Suzanne Mohny
Professor of Materials Science and Engineering and Chemistry
Head of the Department of Materials Science and Engineering

*Signatures are on file in the Graduate School

ABSTRACT

High-capacity Si-based anode is being considered as promising anode material for next generation of Li-ion battery. The energy density could be increased from 250-260 Wh kg⁻¹ to 300-330 Wh kg⁻¹ via replacing graphite with Si-based anode. However, for high-loading Si-based anode, the huge volume change of Si (400%) or SiO (200%) particles during lithiation/delithiation will arise large electrode thickness change. After repeated electrode expansion and contraction, the electrode integrity is seriously damaged, including large electrode cracking, electrode delamination or peeling-off from Cu current collector, as well as continuous growth of solid electrolyte interphase (SEI) layer. When pairing it with commercial cathode, the damage of electrode integrity results in large amount of irreversible lithium ions loss in each cycle and low full-cell Coulombic efficiency of 99.5-99.7%. Thus the full-cell exhibits fast capacity fading and limited cycle life. Another challenge of SiO anode is its low first cycle Coulombic efficiency of 50-60%, which causes huge irreversible lithium ions loss for the first cycle of full-cell and dramatically decreases the cell capacity.

In Chapter 1, we will give an introduction to lithium-ion battery, cell energy density, and advantages and challenges of Si-based anode. The Chapter 2 introduces two strategies to solve the challenges of Si-based anode: including design of nanostructured Si and advanced polymer binder. Also we will also talk about the importance of electrode integrity and the previous work on improving electrode integrity.

In Chapter 3, we reported an elastic and stretchable polyurethane-urea (PUU) gel polymer electrolyte (GPE) coating strategy to improve cycling stability of high-areal-capacity SiO anode. The PUU GPE functions as intra-electrode cushion to accommodate the volume change of SiO electrode. It can alleviate electrode thickness change, inhibit electrode cracking, and improve electrode adhesion strength on Cu current collector. The improved electrode structure integrity

reduces the continuous growth of SEI layer. The half-cell of SiO electrode with PUU coating shows a reversible capacity of 3.0 mAh cm^{-2} for 280 cycles. When paring with commercial cathode, the full-cell shows a reversible capacity of 2.1 mAh cm^{-2} for 200 cycles and 80% capacity retention for 500 cycles with improved full-cell Coulombic efficiency of 99.9%.

In Chapter 4, we demonstrate chemical vapor deposition (CVD) growth of carbon layer on SiOx (C-SiOx). The carbon coating is composed of dense graphene layers. It can not only increase the electronic conductivity, but also decrease the amount of electrolyte decomposition. Thus the first cycle Coulombic efficiency increases to 74.1%. Moreover, when blending C-SiOx with graphite anode, the composite anode shows high first cycle CE of 86.4%.

In Chapter 5, we report a composite LixSi/gel polymer electrolyte composite protection film on the top of lithium meal via simple cast coating approach. The LixSi functions as seeds for lithium nucleation and it has large surface area, thus it can reduce local current density and prevent lithium dendrite growth. When paring with lithium iron phosphate cathode, the cell with composite protection films shows stable capacity at 2.0 mAh cm^{-2} for 400 cycles.

TABLE OF CONTENTS

LIST OF FIGURES	vi
ACKNOWLEDGEMENTS	xiii
Chapter 1 Introduction to high-capacity anode material for Li-ion battery	1
1.1 What's Li-ion battery?.....	1
1.2 Advantages and challenges of Si-based anode	7
Chapter 2 Literature review on Si-based anode	17
2.1 Nanostructured Si active material and advanced functional polymer binder ...	17
2.2 How to improve electrode structure integrity for long-term cycling?	25
Chapter 3 A stretchable intra-electrode cushion for high-loading silicon monoxide anodes in lithium-ion batteries	33
3.1 Introduction	34
3.2 Characterization of PUU polymer	36
3.3 Characterization of SiO electrode with PUU polymer cushion	40
3.4 PUU polymer cushion can help maintain electrode structure integrity	45
3.5 Electrochemical performance of half-cell and full-cell	52
3.6 Discussion	57
3.7 Methods	63
Chapter 4 Development of stable high-capacity carbon-coated SiO _x /Graphite composite anode for lithium ion battery	66
4.1. Introduction	67
4.2. Characterization of graphene wrinkles	68
4.3. Electrochemical performance of C-SiO _x	70
Chapter 5 Seeded growth of lithium metal on Li _x Si-gel polymer electrolyte composite protection film.....	73
5.1. Introduction	74
5.2. Preparation of PPOPI gel polymer electrolyte	76
5.3. Preparation of Li _x Si/PPOPI composite protection film	79
5.4. Lithium deposition morphology	81
5.5. Electrochemical performance	82
5.6. Discussion	83
Reference	84

LIST OF FIGURES

Figure 1. 1 Comparison of different energy storage technique in specific and volumetric energy density, including lead acid battery, Ni-Cd battery, Ni-metal hydride battery, and lithium-ion battery. Ref [2]	1
Figure 1. 2 Typical configuration of Li-ion battery with transition metal oxide cathode, graphite anode, and liquid electrolyte. Ref [2].....	2
Figure 1. 3 Weight percentage of commercial 18650-type lithium-ion battery: (a) high-energy type, (b) high-power type, (c) the corresponding cell information. Ref [6].....	3
Figure 1. 4 The specific capacity of electrode material (C_E) as a function of the specific capacity of cathode (C_C) and anode (C_A).	6
Figure 1. 5 (a) The volumetric capacities of pure Si film, theoretically packed Si NP film, 5 wt%-Graphene-Si electrode and graphite electrode. (b) Cross-sectional SEM images of the 5 wt%-Graphene-Si and commercial graphite electrodes (left). (c) The cycling performance of the 5 wt%-Graphene-Si/LiCoO ₂ and graphite//LiCoO ₂ full cells. The 5 wt%-Graphene-Si electrode in b and c is the one with 3.0 mAh/cm ² . Ref [20].....	8
Figure 1. 6 Challenges of silicon anode. (a) At the particle level, huge volume leads to particle pulverization and loss of electronic contact; (b) At the electrode level, continuous expansion and contraction leads to loss of conductive network and electrode delamination from current collector. (c) At the SEI level, huge volume change of silicon particle leads to continuous SEI cracking and formation of new SEI. Ref [21]	9
Figure 1. 7 The full-cell capacity retention as a function of Columbic efficiency and cycle number.	11
Figure 1. 8 Material characterization of pristine SGC and other anode materials. (a) particle size distribution, citing D10, D50, and D90, (b) specific surface area based on BET theory, and (c) tap density after mechanically tapping a container. Morphological characterization of (d–g) C-SiO _x , (h–k) Si-G/C, and (l–o) SGC. Ref [22].....	13
Figure 1. 9 Electrochemical performances of G/C-SiO _x , G/Si-G/C, and G/SGC in half-cell tests. (a) Voltage profiles of the first cycle. (b) Cycling performance at 0.5 C (1C = 450 mAh g ⁻¹). (c) Rescaled form of CE at each cycle. (d–f) Voltage profiles of (d) G/C-SiO _x , (e) G/Si-G/C, and (f) G/SGC at the 1 st , 50 th , and 100 th cycle. Ref [22]....	15
Figure 1. 10 Electrochemical performances of G/C-SiO _x , G/Si-G/C, and G/SGC in full-cell tests. (a) Voltage profiles of the first formation cycle. (b) Cycling performance at 0.5 C (1C = 450 mAh g ⁻¹) for 400 cycles. (c) Rescaled form of CE at each cycle for 100 cycles. (d-f) Voltage profiles of (d) G/C-SiO _x , (e) G/Si-G/C, and (f) G/SGC at the 1 st , 100 th , 200 th , and 400 th cycle. Ref [22].....	16

- Figure 2. 1 Schematic of Si–C nanocomposite granule formation through hierarchical bottom-up assembly: Annealed carbon-black dendritic particles (a) are coated by Si nanoparticles (b) and then assembled into rigid spheres with open interconnected internal channels during C deposition (c). Morphology characterization of Si-C nanocomposite via SEM (e) and TEM (f and g) analysis. (g) Electrochemical chemical performance of Si-C nanocomposite. Ref [35]..... 17
- Figure 2. 2 Schematic of Si–C nanocomposite granule formation via three steps: heating at 950 °C for 6h; etching of SiO₂ with hydrofluoric acid; carbon coating via CVD decomposition of acetylene. (b) Voltage profile and (c-e) electrochemical performance of Si-C composites. Ref [37] 18
- Figure 2. 3 (a) Electrochemical performance of Si nanoparticles electrode with c-PAA-CMC, CMC, PAA, and PVDF binder. (b) Chemical reaction between polymer binder and Si nanocrystals. (c) Formation mechanism of cross-linked PAA-CMC binder. Ref [54] 19
- Figure 2. 4 (a) Electrochemical performance of Si nanoparticles electrode with c-PAA-PVA binder. (b) Formation mechanism of cross-linked PAA-CMC binder, including chemical reaction between polymer binder and Si nanocrystals. Ref [55] 20
- Figure 2. 5 Proposed stress dissipation mechanism of PR-PAA binder for SiMP anodes. (A) The pulley principle to lower the force in lifting an object. (B) The PR-PAA binder can keep the SiMP electrode integrated after long-term cycling. (C) The PAA binder cannot keep the pulverized Si particles integrated and result in thick SEI formation. Ref [56] 21
- Figure 2. 6 Mechanical properties of PR-PAA and PAA. (A) Stress-strain behaviors of three representative modes. (B) Comparison of stress-strain curves of PR-PAA and PAA films at three strain points. (C) Stress-strain curves of PR-PAA for 10 stretch-recovery cycles with different strain limits. Ref [56]..... 22
- Figure 2. 7 Electrochemical performances of SiMP electrodes with PR-PAA and PAA as binders. (A) Voltage profiles of half-cell for the first cycle. (B) Cycling performance at 0.2C and the CE of electrode with PR-PAA binder. (C) Cycling performance at 0.4C with/without lithium metal change after 200 cycles. (D) The initial charge-discharge profile of the SiMP- LiNi_{0.8}Co_{0.15}Al_{0.05}O₂ full-cell at 0.03C (1C = 190 mA g⁻¹ NCA) and (E) its cycling performance at 0.2C. The n/p ratio based on the capacities of both electrodes is 1.15. Ref [56] 23
- Figure 2. 8 Schematic of key degradation mechanisms in a lithium-ion battery. Graphitic carbon negative electrode on the left. Lithium metal oxide structure on the right. Separator mesh layer in the middle. Green for lithium. Red for metal. Blue for electrolyte. Ref [57] 25
- Figure 2. 9 Schematic solid electrolyte interphase (SEI) layer on graphite anode. Ref [59]... 26

Figure 2. 10 Damage of electrode structure integrity. (a) Particle pulverization; (b) Electrode cracking and delamination; (c) Accumulated growth of SEI layer. Ref [60] ..	27
Figure 2. 11 Morphology and composition of cathode electrolyte interphase (CEI) at cathode surface: (a) TOF-SIMS mapping on $\text{LiNi}_{0.7}\text{Co}_{0.15}\text{Mn}_{0.15}\text{O}_2$ composite electrode after cycling, and (b) a schematic illustration. Ref [61]	28
Figure 2. 12 Crack formation and pulverization of $\text{LiNi}_{0.76}\text{Co}_{0.14}\text{Al}_{0.10}\text{O}_2$ cathode at different depth of discharge (DOD) cycles. (a) pristine cathode; (b) cathode after 2500 cycles with 10-70% DOD at 60°C ; (c) cathode after 350 cycles with 0-100% DOD at 60°C . Ref [61].....	28
Figure 2. 13 Fabrication and characterization of the yolk-shell $\text{Si}@\text{TiO}_2$ cluster electrode. (a) Schematic of the synthesis of the yolk-shell $\text{Si}@\text{TiO}_2$ cluster. (b) STEM image and elemental mapping of Ti, O and Si, confirming the yolk-shell structure. (c) XRD data of the commercial silicon nanocrystals, $\text{Si}@\text{C}$ after hydrothermal treatment and the as-obtained $\text{Si}@\text{TiO}_2$ after 550°C heat treatment in air. (d) SEM image of $\text{Si}@\text{C}@\text{TiO}_2$ after titanium ion adsorption. (e and f) SEM and TEM images of the yolk-shell $\text{Si}@\text{TiO}_2$ cluster after heating at 550°C in air for 2 h. (g) High resolution TEM image of TiO_2 shell. Ref [39].....	30
Figure 2. 14 Electrochemical characterization of the $\text{Si}@\text{TiO}_2$ yolk-shell anode. (a) Half-cell cycling performance and the corresponding coulombic efficiency for 1500 cycles. The mass loading of all active materials was about 0.8 mg cm^{-2} . (b) Full-cell performance of the $\text{Si}@\text{TiO}_2$ yolk-shell anode (2.1 mg cm^{-2}) paired with a lithium cobalt oxide cathode. Ref [39]	30
Figure 2. 15 (a) Scheme 1: schematic illustration of the design and behavior of a conventional silicon electrode. Scheme 2: schematic illustration of the design and behavior of the stretchable self-healing electrode. (b) Chemical structure of the self-healing polymer (SHP). Ref [63]	31
Figure 3. 1 Schematic illustration of the improved integrity of a SiO electrode enabled by the use of a PUU polymer cushion. (a) For bare SiO electrode, large volume change arises a huge electrode expansion upon lithiation, causes electrode cracking, and even peeling-off current collector after many cycles. (b) The stretchable PUU polymer cushion can reduce the electrode expansion upon lithiation, alleviate electrode cracking and delamination, and prevent electrode peeling-off from current collector after many cycles.....	36
Figure 3. 2 Schema of synthesis of polyurethane-urea (PUU) polymer.	37
Figure 3. 3 Fourier transform infrared (FTIR) spectrum of PUU polymer.....	37

- Figure 3. 4 Structure and mechanical and physical properties of PUU cushion polymer. (a) Structure of PUU cushion polymer, which contains poly(tetramethylene ether) glycol (PTMG) as soft domains and (4,4'-methylene diphenyl diisocyanate)-ethylenediamine (MDI-EDA) as hard domains. There are intra-domain interactions (hydrogen bonding and π - π interactions) between hard domains. (b) Stress-strain curve of PUU cushion polymer. (c) Swelling experiment of PUU cushion polymer membrane in a 1 M LiPF₆ in EC/DEC electrolyte. (d) Ionic conductivity of the formed gel polymer electrolyte and liquid electrolyte as a function of temperature.....38
- Figure 3. 5 Electrochemical impedance of PUU cushion polymer gel polymer electrolyte at different temperature (500 μ m in thickness and 1.2 cm² in area).....39
- Figure 3. 6 Cyclic voltammetry of PUU cushion polymer GPE (a) and liquid electrolyte (1M LiPF₆/EC-DEC) (b) with stainless steel working electrode and lithium metal counter electrode at a scan rate of 0.5 mV s⁻¹ between -0.2 V and 4.6 V.40
- Figure 3. 7 Schema of coating PUU solution on SiO electrode.....41
- Figure 3. 8 Cross section SEM image (a) and EDS mapping of pristine SiO electrode with PUU coating for corresponding elements of (b) Si, (c) C, and (d) N.....41
- Figure 3. 9 SEM characterization of pristine SiO electrode with different amount of PUU coating: (a-d) 0.4 mg cm⁻²; (e-h) 0.8 mg cm⁻². (a), (b), (e) and (f) are the top-view images; (c), (d), (g), and (h) are cross-section images.42
- Figure 3. 10 The atomic force microscope (AFM) height images pristine bare SiO electrode (a-c) and pristine SiO electrode with PUU cushion polymer (d-f).....43
- Figure 3. 11 X-ray photoelectron spectroscopy (XPS) analysis of SiO electrode without/with PUU polymer cushion. (a), (b), and (c) pure PUU; (d), (e), and (f) pristine SiO electrode without PUU polymer cushion; (g), (h), and (i) pristine SiO electrode with PUU polymer cushion.44
- Figure 3. 12 Characterization of SiO electrodes with PUU polymer cushion. (a) In-situ measurement of thickness changes of a bare SiO electrode and a SiO electrode with PUU polymer cushion in the initial three lithiation/delithiation cycles at current density of 0.3 mA cm⁻² between 0.01 V and 1.5 V. (b,c) Top-view (b) and cross-sectional (c) SEM images of the bare SiO electrode after 10 cycles. (d and e) Top-view (d) and cross-sectional (e) SEM images of the SiO electrode with polymer cushion after 10 cycles. (f) Peel adhesion test of SiO electrodes with and without polymer cushion, which were peeled-off from Cu foil using a 90 degree dragging force.46
- Figure 3. 13 Morphology characterization of SiO electrode after different cycles. (a-c) SEM images of SiO electrode without PUU polymer cushion after 1 discharge/charge cycle; (d-f) SEM images of SiO electrode with PUU polymer cushion after 1 discharge/charge cycle; (g-i) SEM images of SiO electrode without PUU polymer cushion after 10 discharge/charge cycles; (j-k) SEM images of SiO electrode with PUU polymer cushion after 10 discharge/charge cycles; (m-o) SEM

images of SiO electrode without PUU polymer cushion after 10 discharge/charge cycles; (p-r) SEM images of SiO electrode with PUU polymer cushion after 10 discharge/charge cycles.....	47
Figure 3. 14 Electrode stability test under magnetic stirring: SiO electrode without PUU coating (a) pristine electrode and (c) electrode after 10 discharge cycles; SiO electrode with PUU coating (b) pristine electrode and (d) electrode after 10 discharge cycles.	48
Figure 3. 15 X-ray photoelectron spectroscopy (XPS) analysis of SiO electrode without/with PUU polymer cushion: (a-c) SiO electrode without PUU polymer cushion after 10 discharge/charge cycles; (d-f) SiO electrode with PUU polymer cushion after 10 discharge/charge cycles.	50
Figure 3. 16 Electrochemical impedance spectroscopy (EIS) of SiO electrode without (a) and with (b) PUU polymer cushion at 1 cycle, 10, 50, and 100 cycles; (c) and (d) are the detailed analysis of each impedance data following equivalent circuit (e).	51
Figure 3. 17 Electrochemical performance of SiO anodes. (a) Half-cell discharge capacities of a bare SiO electrode and a SiO electrode with polymer cushion at 0.3 mA cm ⁻² for the first cycle and 1.0 mA cm ⁻² for rest cycles between 0.01 and 1.5 V, along with the Coulombic efficiency of SiO electrode with polymer cushion. (b) Electrochemical impedance spectroscopy (EIS) of a bare SiO electrode and a SiO electrode with polymer cushion after 1, 10, 50, and 100 cycles. (c) Full-cell discharge capacities of bare SiO NCM 523 and SiO with polymer cushion NCM 523 cells at 0.3 mA cm ⁻² for the initial 3 cycles and 1.0 mA cm ⁻² for rest cycles between 2.8 and 4.2 V, along with the Coulombic efficiency of SiO with polymer cushion NCM 523 cell. (d and e) Corresponding voltage profiles of SiO NCM 523 cells without (d) and with (e) polymer cushion. The SiO electrodes were precycled for full cell assembling.....	53
Figure 3. 18 The full-cell capacity retention as a function of Columbic efficiency (CE) and cycle number: 99.5% is full-cell of NCM/SiO electrode without PUU coating; 99.9% is full-cell of NCM/SiO electrode with PUU coating; 99.95% is full-cell of commercial NCM/Graphite cell.	55
Figure 3. 19 Electrochemical performances of pre-cycled NCM cathode paired with pre-cycled SiO electrode with/without PUU polymer cushion: NCM cathode on discharged state (5 cycles, 2.2 mAh cm ⁻²) and pre-cycled SiO anode on lithiated state (10 cycles, 2.9 mAh cm ⁻²), with a current density of 0.3 mA cm ⁻² for the 3 cycles and 1.0 mA cm ⁻² for rest cycles, between 3.8-4.2 V.	56
Figure 3. 20 Electrochemical performance of SiO electrode with different amount of PUU polymer cushion (the mass loading of SiO is 2.6 mg cm ⁻²) at a current density of 0.3 mA cm ⁻² for the first cycle and 1.0 mA cm ⁻² for rest cycles between 0.01-1.5 V.	57
Figure 3. 21 Electrochemical performance of SiO electrode with/without PUU polymer cushion at different areal capacity: (a) 2 mAh cm ⁻² , the mass loading of SiO is 1.8	

mg cm ⁻² , the PUU coating is 0.3-0.4 mg cm ⁻² ; (b) 3 mAh cm ⁻² , the mass loading of SiO is 2.6 mg cm ⁻² , the PUU coating is 0.3-0.4 mg cm ⁻² ; (c) 4 mAh cm ⁻² , the mass loading of SiO is 3.3 mg cm ⁻² , the PUU coating is 0.6-0.7 mg cm ⁻²	58
Figure 3. 22 Electrochemical performance of SiO electrode with different polymer coating and the polymer coating amount is fixed to 0.3-0.4 mg cm ⁻² (the mass loading of SiO is 2.6 mg cm ⁻² , at a current density of 0.3 mA cm ⁻² for the first cycle and 1.0 mA cm ⁻² for rest cycles).	59
Figure 3. 23 Electrochemical performance of full-cell of Si microparticle electrode without/with PUU polymer cushion NCM. (a) full-cell cycling performance at 0.12 mA cm ⁻² for the first cycle and 0.45 mA cm ⁻² for rest cycles under constant-current-constant-voltage mode between 2.4-4.2 V; Voltage profiles of (b) bare Si microparticles electrode NCM full-cell and (c) Si microparticles electrode with PUU polymer cushion NCM full-cell.	61
Figure 4. 1 Microscopic characterization of carbon coated SiO _x (C-SiO _x). (a) (b) TEM and (c) high-resolution TEM images of graphene wrinkles. (d) STEM image and (e-g) EDS elemental mapping of C-SiO _x	68
Figure 4. 2 Raman spectra of raw SiO and C-SiO _x	69
Figure 4. 3 X-ray diffraction of raw SiO and C-SiO _x	70
Figure 4. 4 Electrochemical performance of C-SiO _x electrode. (a) Voltage profile of SiO electrode and C-SiO _x electrode for the first cycle. (b) Discharge capacity of SiO electrode and C-SiO _x electrode with the corresponding CE. The mass loading electrode is 2.6 mg cm ⁻²	71
Figure 4. 5 Electrochemical performance of C-SiO _x /graphite composite anode. (a) Voltage profile of SiO/graphite composite anode and C-SiO _x /graphite composite anode for the first cycle. (b) Discharge capacity of SiO/graphite composite anode and C-SiO _x /graphite composite anode with the corresponding CE. The mass loading electrode is 6.0 mg cm ⁻²	72
Figure 5. 1 Schema of synthesis of PPOPI polymer.	76
Figure 5. 2 Swelling experiments of PPOPI membrane in carbonate electrolyte (a) and the corresponding change in polyimide (PI) content, membrane thickness, membrane diameter, and electrolyte uptake amount.....	77

Figure 5. 3 Ionic conductivity of PPOPI gel polymer electrolyte at different temperature.	78
Figure 5. 4 Shema of coating composite protection film on lithium meal.....	79
Figure 5. 5 XRD patterns of composite protection film coated on stainless steel (SS) and lithium metal chip.	80
Figure 5. 6 Morphology characterization of composite of protection on lithium metal chip. (a-c) Top-viewed SEM images and (d) Cross-sectional SEM images.	81
Figure 5. 7 Characterization of lithium deposition morphology in LFP cell after 10 cycles.....	81
Figure 5. 8 Electrochemical performance of LFP cathode paring different lithium metal anode (a) and the corresponding voltage profile of LFP cell with blank lithium (b), lithium coated with PPOPI-13 polymer, and lithium coated with composite protection film(c). The mass loading of LFP cathode is 15 mg cm^{-2} with an areal capacity of 2.0 mAh cm^{-2}	82

ACKNOWLEDGEMENTS

I would like to thank Prof. Donghai Wang to give me a chance to go on my PhD study in Penn State. Thanks a lot for his guidance, encouragement, patience, and tremendous support on my research. I have learned lots of knowledge on scientific research during past five years.

I would like to thank my other committee members: Prof. Chao-Yang Wang, Prof. Adri van Duin, Prof. Long-qing Chen, and Prof. James Runt, for graciously serving on my committee.

I would like to thank all the colleagues in my lab, past and present, for their stimulating discussions on research, their kind help, and the camaraderie we have shared. I would like appreciate Dr. Jiangxuan Song's for his countless help and great guidance at the beginning of PhD study. I would thank Yue Gao and Daiwei Wang for their kind help on my research and manuscript. I would also like to thank Dr. Mikhail Gordin, Dr. Tianren Xu, Dr. Shuru Chen, Dr. Ran Yi, Dr. Dr. Guoxing Li, Dr. Yuming Zhao, Dr. Jiantao Zai, Dr. Duihai Tang, Dr. Shi Hu, Dr. Hiesang Sohn, Dr. Adnan Mousharraf Michael Melnyk, Michael Regula, Tianhang Chen and Artif AlZahrani, and Yushen Wang.

I would like to thank to Shufu Peng and Alan E Goliaszewski from Ashland Specialty Ingredients Wilmington Research Center for their kind support and nice help on the research on Si-based anode.

I would like to thank the funding projects from Energy Efficiency and Renewable Energy, Office of Vehicle Technologies of the U.S. Department of Energy to support my PhD study.

Finally, my deep thanks to my parents for supporting me throughout the entire PhD study. Thanks for their kindness, patience and endless love.

Chapter 1

Introduction to high-capacity anode material for Li-ion battery

1.1 What's Li-ion battery?

Electrochemical energy storage devices is playing an important role in our daily life. Among the many candidates, lithium-ion battery (LIB) offers much higher energy density and specific energy than that of lead-acid battery (as shown in **Figure 1-1**); it shows little memory effect and low self-discharge rate in comparison with Ni-Cd battery; it can also provide relatively high power capability and good cycle life¹⁻⁵. Thus lithium-ion battery dominates the market of portable personal electronics (smart phones and laptops), electric vehicles (EVs) and energy storage devices for smart grid.

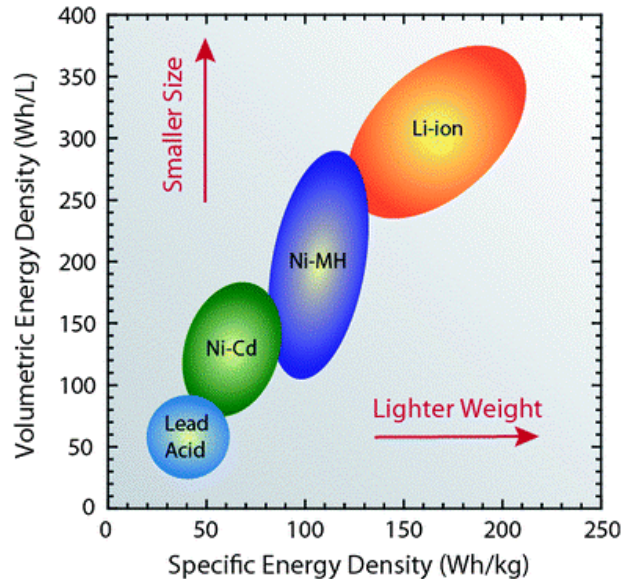


Figure 1. 1 Comparison of different energy storage technique in specific and volumetric energy density, including lead acid battery, Ni-Cd battery, Ni-metal hydride battery, and lithium-ion battery. Ref [2]

The lithium-ion battery is mainly composed of four parts: cathode and anode function as a host to store lithium ions; liquid electrolyte is prepared by dissolving lithium salts in organic solvent to conduct lithium ions; the porous and insulate polymer separator absorbs liquid electrolyte and

electrically isolates cathode and anode from cell short-circuit¹⁻³. As shown in **Figure 1-2**, when charging the battery, the lithium ions deintercalate from the layered transition metal oxide cathode, dissolve in liquid electrolyte and migrate towards the anode side, and intercalate into graphene interlayer of graphite anode. Upon discharging, the lithium ions move in the opposite direction.

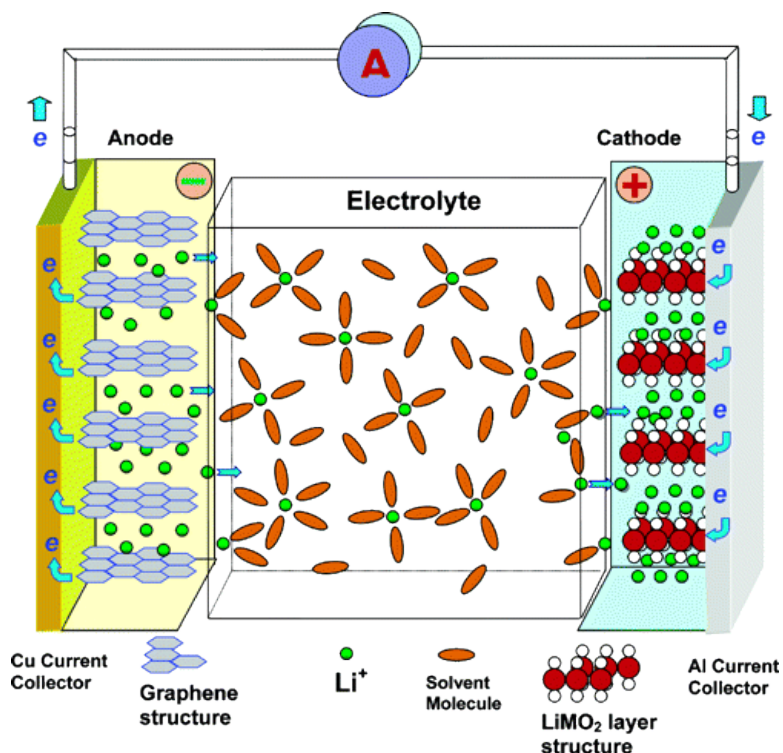


Figure 1. 2 Typical configuration of Li-ion battery with transition metal oxide cathode, graphite anode, and liquid electrolyte. Ref [2]

The energy density defines the total energy stored in lithium-ion battery per unit mass/volume. The energy density is determined by specific capacity of cathode, specific capacity of anode, voltage difference between cathode and anode, and battery energizing design (electrode formulation, porosity and areal loading, dead weight of current collector, electrolyte, separator, tabs and battery case). **Figure 1-3** shows typical compositions the corresponding weight percentage of commercial 18650-type lithium-ion battery: (a) is high-energy type lithium-ion battery with high capacity of 2.6 Ah, (b) is high-power type lithium-ion battery with low capacity of 1.5 Ah⁶. The

total cell energy is determined by cell capacity multiplying cell voltage. Thus the cell energy of high-energy type lithium-ion battery is 9.62 Wh and that of high-power type lithium-ion battery is 5.55 Wh. By dividing the cell weight listed in table, the cell energy density of high-energy type lithium-ion battery is 217 Wh kg⁻¹ and that of high-power type lithium-ion battery is 129 Wh kg⁻¹. For high-energy type lithium-ion battery, the weight percentage of cathode and anode is as high as 59 wt% due to the high areal mass loading of active material and relatively low porosity of electrode. For high-power type lithium-ion battery, the mass ration of cathode and anode is only 41 wt%, because the areal mass loading of active material is low and the porosity is high.

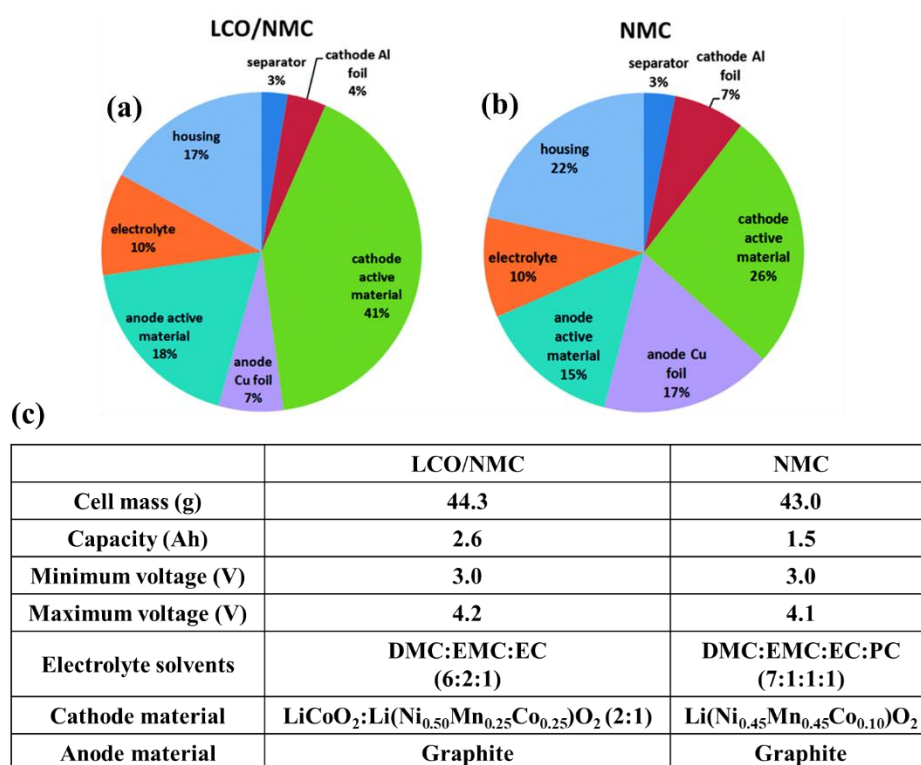


Figure 1. 3 Weight percentage of commercial 18650-type lithium-ion battery: (a) high-energy type, (b) high-power type, (c) the corresponding cell information. Ref [6]

The energy density of lithium-ion battery can also be calculated from the specific capacity of electrode material (C_E), voltage difference between cathode and anode or average cell voltage

(V_C), and the weight percentage of cathode and anode electrode in lithium-ion battery (W_E). The energy density is calculated via following equation:

$$\text{Energy density} = C_E * V_C * W_E$$

The specific capacity of electrode material (C_E) is calculated from the specific capacity of cathode (C_C) and anode (C_A) following equation:

$$\frac{1}{C_E} = \frac{1}{C_C} + \frac{1}{C_A}$$

As an example of high-energy type lithium-ion battery, the LiCoO_2 cathode has a specific capacity of 140 mAh g^{-1} and $\text{LiNi}_{0.5}\text{Co}_{0.25}\text{Mn}_{0.25}\text{O}_2$ cathode has a specific capacity of 164 mAh g^{-1} ; the cathode electrode is composed cathode power, conductive carbon, and polymer binder, in which the cathode mass ratio can reach as high as 94%. Thus the specific capacity of total cathode is:

$$C_C = (140 \text{ mAh/g} * 1/3 + 164 \text{ mAh/g} * 2/3) * 0.94 = 146.6 \text{ mAh/g}$$

For the graphite anode, it has a specific capacity of 370 mAh g^{-1} and the mass ratio of active material is 96%. When paring graphite anode with cathode, the anode capacity is usually 5% higher than that of cathode, so as to prevent lithium plating on graphite anode during charging process at high rate or at low temperature (lithium dendrite may short-circuit the battery and cause safety issues). Thus the specific capacity of total anode is:

$$C_A = 340 \text{ mAh/g} * 0.96/1.05 = 310.8 \text{ mAh/g}$$

The specific capacity of total electrode (C_E) is:

$$C_E = \frac{1}{\frac{1}{C_C} + \frac{1}{C_A}} = 99.6 \text{ mAh/g}$$

Considering the average cell of voltage (V_C) is 3.7 V and the weight percentage of cathode and anode electrode in lithium-ion battery (W_E) is 59%. Then cell energy density is:

$$\text{Energy density} = C_E * V_C * W_E = 99.6 \text{ mAh/g} * 3.7 \text{ V} * 0.59 = 217.5 \text{ Wh/kg}$$

In order to increase the energy density of lithium-ion battery, great efforts have been devoted to increasing the weight percentage of cathode and anode electrode in lithium-ion battery⁷⁻¹¹. For example, higher-mass-loading electrode material and thinner current collector lead to smaller relative weight percentage of current collector in total electrode; lower porosity of electrode and thinner separator indicate smaller amount of liquid electrolyte in lithium-ion battery. The overall weight percentage of cathode and anode material in a lithium-ion battery can reach as high as 55 wt% to 60 wt%. For a given cathode and anode material, when weight percentage of cathode and anode material reach its maximum, the cell energy density cannot achieve further improvement. Thus another effective method to increase cell energy density is to design new high-capacity cathode and anode material so as to increase the specific capacity of total electrode (C_E).

As shown in **Figure 1-4**, the specific capacity of electrode material (C_E) is plotted as a function of the specific capacity of cathode (C_C) and anode (C_A) material. In 1991, the SONY cooperation commercialized the first generation of lithium ion battery, which is composed of LiCoO_2 cathode (140 mAh g^{-1}) and graphite anode (370 mAh g^{-1}). Then the specific capacity of electrode material is 101.6 mAh g^{-1} . Even though the theoretical capacity of LiCO_2 is 274 mAh g^{-1} , only 50% of lithium ions can be reversibly extracted/inserted from the layered structure, otherwise further extraction of lithium ions will damage the layered structure and sacrifice cycling stability¹². The substitution of Co with Ni, Mn, Al can stabilize the layered structure upon lithium extraction and thus more than 50% lithium ion can be reversibly extracted/inserted to increase the specific capacity of cathode material. For example, the NCM-111 ($\text{LiNi}_{1/3}\text{Co}_{1/3}\text{Mn}_{1/3}\text{O}_2$) and NCM-532 ($\text{LiNi}_{0.5}\text{Co}_{0.3}\text{Mn}_{0.2}\text{O}_2$) show a reversible capacity of 154 mAh g^{-1} and 164 mAh g^{-1} at 0.1C; the high-nickel NCM-622 ($\text{LiNi}_{0.6}\text{Co}_{0.2}\text{Mn}_{0.2}\text{O}_2$) and NCM-811 ($\text{LiNi}_{0.8}\text{Co}_{0.1}\text{Mn}_{0.1}\text{O}_2$) even have a reversible capacity 178 mAh g^{-1} and 185 mAh g^{-1} at 0.1C. Another example is NCA ($\text{LiNi}_{0.8}\text{Co}_{0.15}\text{Al}_{0.05}\text{O}_2$) type cathode, which also shows layered structure with a reversible capacity 200 mAh g^{-1} .

When pairing graphite anode with NCM (170 mAh g^{-1}) and NCA cathode (200 mAh g^{-1}), the specific capacity of electrode material is 113.3 mAh g^{-1} and 125.9 mAh g^{-1} , which shows in improvement of 11% and 24% electrode specific capacity than that of $\text{LiCoO}_2/\text{graphite}$ battery. Considering that the average cell voltage of 3.7 V and the weight percentage of cathode and anode material is 60 wt%, the corresponding cell energy density for the three types of lithium-ion battery are 225 Wh kg^{-1} ($\text{LiCoO}_2/\text{graphite}$), 251 Wh kg^{-1} (NCM/graphite), and 279 Wh kg^{-1} (NCA/graphite). The increasing cathode specific capacity can dramatically increase the electrode specific capacity and cell energy density.

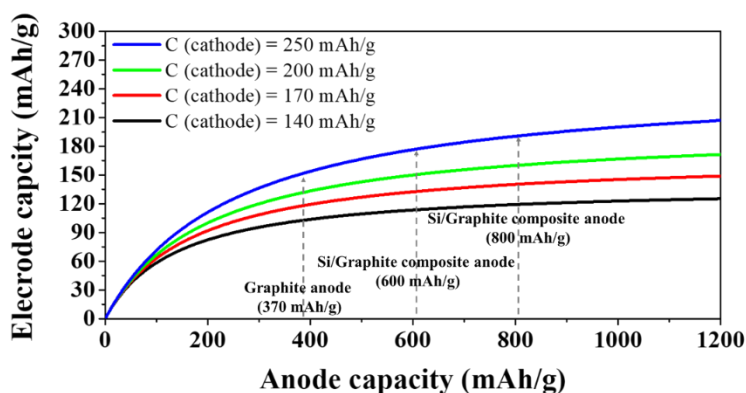


Figure 1. 4 The specific capacity of electrode material (C_E) as a function of the specific capacity of cathode (C_C) and anode (C_A).

Except the development of new type of high-capacity cathode material, the development of high-capacity anode material is also promising to increase electrode capacity and cell energy density. When pairing LiCoO_2 cathode with Si-Graphite-600 and Si-Graphite-800 composite anode, the specific capacity of electrode material is 113.5 mAh g^{-1} and 119.1 mAh g^{-1} , which shows in improvement of 12% and 17% electrode specific capacity than that of $\text{LiCoO}_2/\text{graphite}$ battery. Considering that the average cell voltage of 3.7 V and the weight percentage of cathode and anode material is 60 wt%, the corresponding cell energy density for the three types of lithium-ion battery are 225 Wh kg^{-1} ($\text{LiCoO}_2/\text{graphite}$), 252 Wh kg^{-1} (NCM/Si-graphite-600), and 264 Wh kg^{-1}

(NCM/Si-graphite-800). When the anode specific capacity reach above 800 mAh g⁻¹, the electrode specific capacity increase slowly with further increasing anode specific capacity.

Both the development of high-capacity cathode and high-capacity anode can improve the electrode specific capacity and cell energy density. In order to increase the standby time of smart phones and enlarge the millage of EVs per charge, it requires developing lithium-ion battery with high energy density, pushing forward development of both high-capacity cathode and high-capacity anode material. For example, when pairing NCA with Si-graphite-800 composite anode, is shows an electrode specific capacity of 160 mAh g⁻¹. Assuming that the average cell voltage of 3.7 V and the weight percentage of cathode and anode material is 60 wt%, the corresponding cell energy density is 355 Wh kg⁻¹. The Chinese government is planning to increase the cell energy density to 300 Wh kg⁻¹ by 2020 and 350 Wh kg⁻¹ by 2025 for electric vehicle application. The first-step is to commercialize high-nickel (> 80%) NCM cathode, the combination with graphite can improve cell energy density to 250-280 Wh kg⁻¹. The second-step is to commercialize Si-graphite anode with a specific capacity of 600-800 mAh g⁻¹, the combination of high-nickel NCM cathode can improve cell energy density to 333-355 Wh kg⁻¹.

In summary, the growing demand of lithium-ion battery with high energy density requires the development of high-capacity cathode and anode material, as well as improvement of cell engineering design to reduce dead weight and increase weight percentage of electrode material. To reach to target of 300-350 Wh kg⁻¹ lithium-ion battery cell, both high-nickel NCM cathode and Si-graphite anode are preferred for practical application.

1.2 Advantages and challenges of Si-based anode

Graphite is composed of graphene layers stacking parallel to each other via van der Waals bonds. In the 1980s, researcher found that lithium ions can reversibly intercalate into graphene

interlayer. The electrochemical intercalation of lithium ions in graphite shows excellent reversibility and also low electrochemical potential, thus graphite is the commercial anode material for lithium-ion battery. However, graphite anode shows limited specific capacity of 370 mAh g^{-1} and the further intercalation of lithium ions will lead to lithium plating on the surface of graphite electrode, which may pierce through separator and short circuit the battery, causing serious safety issues.

Silicon is one of the most promising anode material being considered as next generation high-energy and high-power lithium ion battery. Silicon anode shows a high theoretic specific capacity of 4200 mAh g^{-1} , which is 10 times higher than that of conventional graphite anode, meanwhile it also shows a relatively low average potential ($0.4 \text{ V vs. Li}^+/\text{Li}$)^{8,10,13–19}. The replacement of graphite anode with Si anode can greatly improve the volumetric energy density of lithium-ion battery.

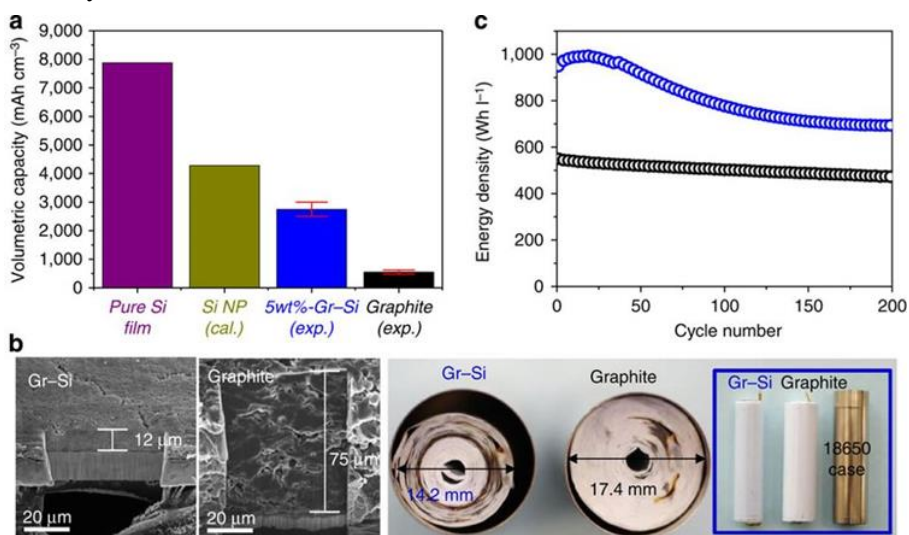


Figure 1. 5 (a) The volumetric capacities of pure Si film, theoretically packed Si NP film, 5 wt%-Graphene-Si electrode and graphite electrode. (b) Cross-sectional SEM images of the 5 wt%-Graphene-Si and commercial graphite electrodes (left). (c) The cycling performance of the 5 wt%-Graphene-Si//LiCoO₂ and graphite//LiCoO₂ full cells. The 5 wt%-Graphene-Si electrode in b and c is the one with 3.0 mAh/cm^2 . Ref [20]

As shown in **Figure 1-5**, two types of anodes are paired with LiCoO₂ cathode to wind into cylindrical cell: one is graphite electrode with a thickness of 75 μm and an areal capacity of 3.0 mAh cm⁻²; the other is Si anode composed of silicon nanoparticles coated with 5 wt% graphene carbon layer, and the 5 wt%-Graphene-Si electrode with an areal capacity of 3.0 mAh cm⁻² is only 12 μm in thickness, which is much thinner than that of graphite electrode²⁰. As a result, the cylindrical cell of 5 wt%-Graphene-Si//LiCoO₂ is much smaller than that of graphite//LiCoO₂ full cells with the same total energy (9.0 Wh). In Figure 1-5c, the 5 wt%-Graphene-Si//LiCoO₂ cell shows above 900 Wh L⁻¹ for initial 50 cycles, which is remarkable since it is 1.8 times as large as that (550Wh L⁻¹) of widely used current commercial LIBs of graphite//LiCoO₂ cell. However, the cycling stability of the 5 wt%-Graphene-Si//LiCoO₂ cell is not good, and its volumetric energy density drops to 700 Wh L⁻¹ after 200 cycles²⁰.

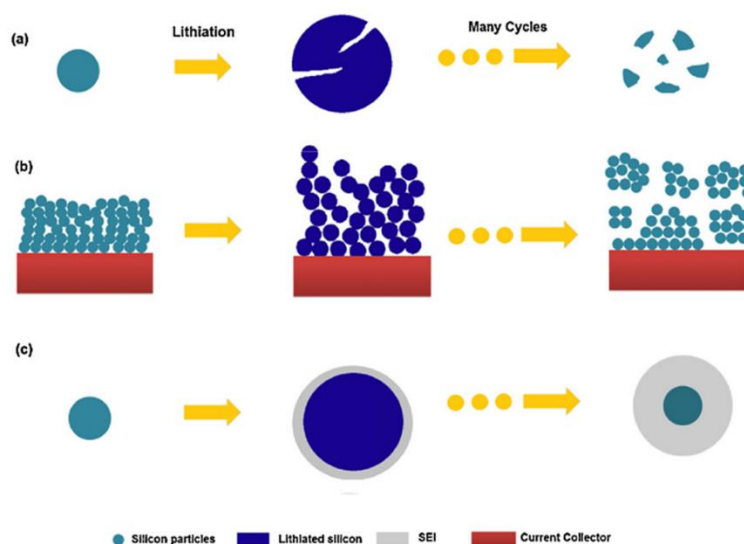


Figure 1. 6 Challenges of silicon anode. (a) At the particle level, huge volume leads to particle pulverization and loss of electronic contact; (b) At the electrode level, continuous expansion and contraction leads to loss of conductive network and electrode delamination from current collector. (c) At the SEI level, huge volume change of silicon particle leads to continuous SEI cracking and formation of new SEI. Ref [21]

However, Si-based anode still encounters issues of fast fading capacity, poor cycling stability and short cycle life, as a result of the huge volume change of Si particle (>300%) during

charge/discharge cycles, as shown in **Figure 1-6**. At the particle level, huge volume change generates large strain inside Si particle and the repeated expansion/shrinkage results in Si particle pulverization²¹. At the electrode level, huge volume change of Si particle causes large swelling/contraction of whole electrode (electrode thickness change); upon long-term cycling, some of pulverized Si particles may lose conductive network and some parts of electrode may delaminate from Cu current collector, resulting in damaging electrode structure integrity²¹. At the SEI (solid electrolyte interface) level, the SEI layer on the surface of Si particle is only tens of nanometer thick, which is difficult to accommodate the huge volume change of Si particle; thus the SEI layer keeps cracking and new SEI layer forms on fresh pulverized Si particle surface in contact with liquid electrolyte²¹. To above, the particle pulverization and electrode swelling/contraction issues lead to the loss of conductive network, damage of electrode structure integrity, and unstable SEI layer, which is the primary reason of fast fading capacity, poor cycling stability and short cycle life of Si anode.

Besides, for practical application of Si-based anode in Li-ion battery, it still encounters several challenges. The first challenge of Si-based anode is its low first cycle coulombic efficiency. For Si anode (nanoparticles, microparticles, and porous Si), the first cycle coulombic efficiency is 80-85%, which is lower than that of graphite anode with 92%. As we know, the commercial Li-ion battery has limited amount of lithium ions resource from transition metal oxide cathode. The lower first cycle coulombic efficiency indicates that much more lithium ions take parts in the SEI layer formation and less lithium ions is able to shuttle between cathode and anode, which will decrease the cell capacity and sacrifice cell energy density. For SiO anode, the first cycle Coulombic efficiency is even as low as 60%, due to the formation of inactive lithium oxide and lithium silicate phase. The irreversible reaction will traps lots of lithium ions and dramatically decrease full-cell capacity. The first cycle coulombic efficiency should match with that of cathode, so as to improve lithium ions unitization ratio and increase cell energy density.

The second change of Si-based anode is its low full-cell Coulombic efficiency of below 99.7%. The full-cell Coulombic efficiency indicates the amount of lithium ions that is trapped in the formation of new SEI layer in each charge/discharge cycle. As we know, the total amount of lithium ions that shuttles between cathode and anode is fixed. If more lithium ions was trapped in each cycle, the full-cell capacity will drops faster. **Figure 1-7** shows the full-cell capacity retention as a function of full-cell Coulombic efficiency. Supposed that the initial capacity is fixed to unit 1; the full-cell Coulombic efficiency (CE) is defined as $C(N+1)/C(N)$, whereas the $C(N)$ is the cell capacity at N^{th} cycle; the CE are the same at different cycles. Then the cell capacity can be calculated via following equation.

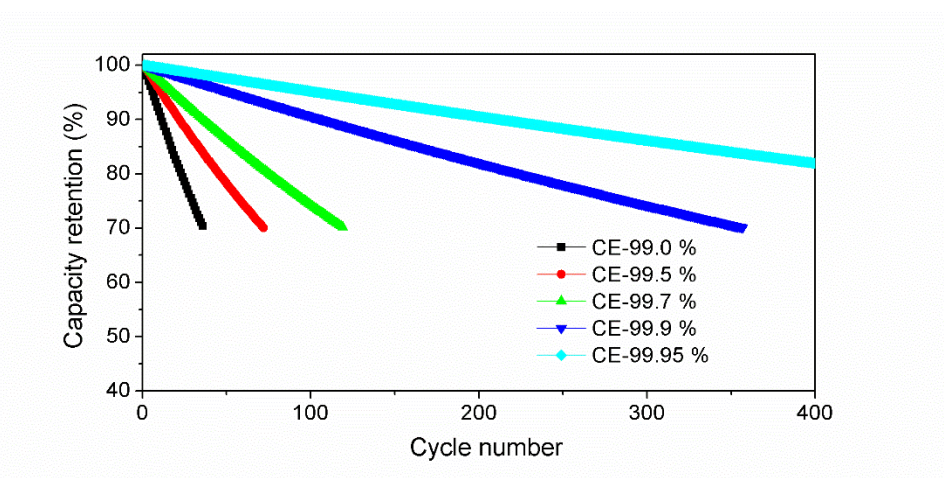


Figure 1. 7 The full-cell capacity retention as a function of Coulombic efficiency and cycle number.

$$C(2) = C(1) * CE$$

$$C(3) = C(2) * CE = C(1) * CE^2$$

$$C(4) = C(3) * CE = C(1) * CE^3$$

.....

$$C(N) = C(N-1) * CE = C(1) * CE^N$$

As we can see from the figure:

If the CE is 99.0%, the capacity retention drops below 80% after 24 cycles;

If the CE is 99.5%, the capacity retention drops below 80% after 46 cycles;

If the CE is 99.7%, the capacity retention drops below 80% after 76 cycles.

If the CE is 99.9%, the capacity retention drops below 80% after 225 cycles.

If the CE is 99.95%, the capacity retention drops below 80% after 448 cycles.

From the figure, the full-cell CE of 99.0%, 99.5%, 99.7%, and 99.9% is very low, the full-cell lithium ion battery cannot meet the demand of application in portable personal electronics that requires at least 80% capacity retention after 500 cycle. For EV application like Tesla Model 3, the battery shows 70% capacity retention after 600 cycles (120000 miles). The calculated full-cell CE should be above 99.95%. For commercial Li-ion battery of NCM cathode paring with graphite anode, the full-cell Coulombic efficiency reaches as high as 99.98% when using specific type of electrolyte additives, and the capacity retention drops below 80% after 1115 cycles. When paring NCM cathode with LTO ($\text{Li}_4\text{Ti}_5\text{O}_{12}$) anode, the full-cell Coulombic efficiency reaches as high as 99.99%, and the capacity retention drops below 80% after 2231 cycles.

When paring Si-based anode with commercial NCM cathode, the full-cell CE is usually lower than 99.6%. As a result, the full-cell shows limited cycle life of less than 100 cycles for 80% capacity retention, which is the main reason that hinder that application of Si-based anode for Li-ion battery. For pure Si anode, the SEI layer cannot tolerate such large volume change of Si (400%) that the SEI layer keeps cracking and forming new SEI layer, resulting in large amount of irreversible lithium ions loss. For SiO electrode, it can deliver a specific capacity of 1400 mAh g^{-1} and the volume change of SiO is around 150%. However, the first cycle CE is too low of 60% and SiO cannot directly used as anode for Li-ion battery. To solve the low first cycle CE and cycling stability issues, one effective way is to mix small amount of Si (nanoparticles, porous Si) or c-SiO (with carbon coating) with graphite anode. Because the first cycle CE of graphite is as high as 92% and it also shows good cycling stability. The composite anode shows stable specific capacity of

450-600 mAh g⁻¹ with high first cycle CE of 83-88%. Below is an example of Si/graphite composite anode²².

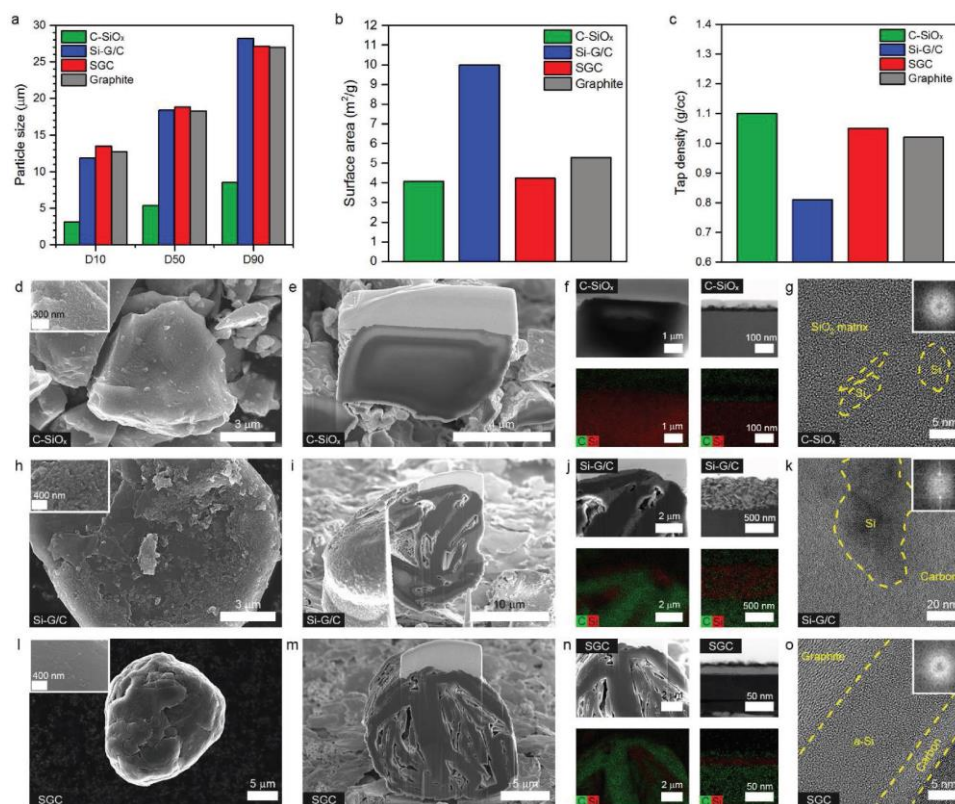


Figure 1. 8 Material characterization of pristine SGC and other anode materials. (a) particle size distribution, citing D10, D50, and D90, (b) specific surface area based on BET theory, and (c) tap density after mechanically tapping a container. Morphological characterization of (d–g) C-SiO_x, (h–k) Si-G/C, and (l–o) SGC. Ref [22]

Figure 1-8 shows three types of different of Si-based anode²². The first type is C-SiO_x. Figure 1-8d shows irregularly shaped C-SiO_x with an uneven coating layer on the surface. It is composed of Si nanoparticles embedded within SiO₂ matrix and the whole particles is coated with a carbon layer of 25 nm. The size of crystalline Si is 5-8 nm as shown Figure 1-8g. The second type is Si-G/C (Si containing graphite/carbon composites), which is prepared by mixing Si with graphite at mass ratio of 1:9 via high-energy milling. The Si-G/C particles shows spherical-shaped graphite

particles comprising Si nanocrystals embedded within disordered carbon. However, the EDS mapping shows that Si nanocrystals exist both on the inner side and surface of graphite particles, thus the carbon coating is not uniform. And the size of Si nanocrystals is around 150 nm. The structure will not tolerate the volume change of Si upon cycling and it undergoes mechanical failure after many cycles. The third type is SGC (Si nanolayer-embedded graphite/carbon). It is prepared via two steps: firstly, graphite is coated with Si nanolayer via CVD (chemical vapor deposition); secondly, the Si nanolayer coated graphite is further coated with carbon layer. The SEM images of the SGC in Figure 1-8l shows a smooth surface texture. From the EDS mapping analysis of the cross-section SGC particle, a thin and homogenous Si nanolayer is uniformly coated on the surface of graphite. The TEM image in Figure 1-8o shows the Si nanolayer is around 25 nm in thickness and the carbon coating layer is uniformly formed on the outmost surface of the Si nanolayer, where the thickness of the carbon coating is around 5 nm. The sandwiched structure can tolerate the volume change of Si during charge/discharge cycles²².

The half-cell performance of the above three types of Si-based anode is shown in **Figure 1-9**²². The C-SiOx shows a discharge capacity of 2100 mAh g⁻¹ and a charge capacity of 1600 mAh g⁻¹ with a CE of 76% fist for the first cycle. The Si-G/C shows a discharge capacity of 800 mAh g⁻¹ and a charge capacity of 680 mAh g⁻¹ with a CE of 85% fist for the first cycle. The C-SiOx shows a discharge capacity of 568 mAh g⁻¹ and a charge capacity of 523 mAh g⁻¹ with a CE of 92% fist for the first cycle. By blending with certain amount of graphite, the specific capacity of whole capacity is fixed to 400 mAh g⁻¹. The areal of capacity of each electrode is fixed to 3.4 mAh cm⁻² to pair with industry commercial cathode. As shown in Figure 1-9, the SGC electrode shows highest first cycle of 91.6%, compared with that of 89.3% for C-SiOx and 91.0% for Si-G/C. Also the SGC electrode shows the best cycling stability with 97.2% capacity retention after 100 cycles, compared with that of 92.6% capacity retention after 100 cycles for Si-G/C and 84.2% capacity retention after

100 cycles for C-SiOx. After mixing with graphite, all the three electrode shows good cycling stability in half-cell with high areal capacity of 3.4 mAh cm^{-2} .²²

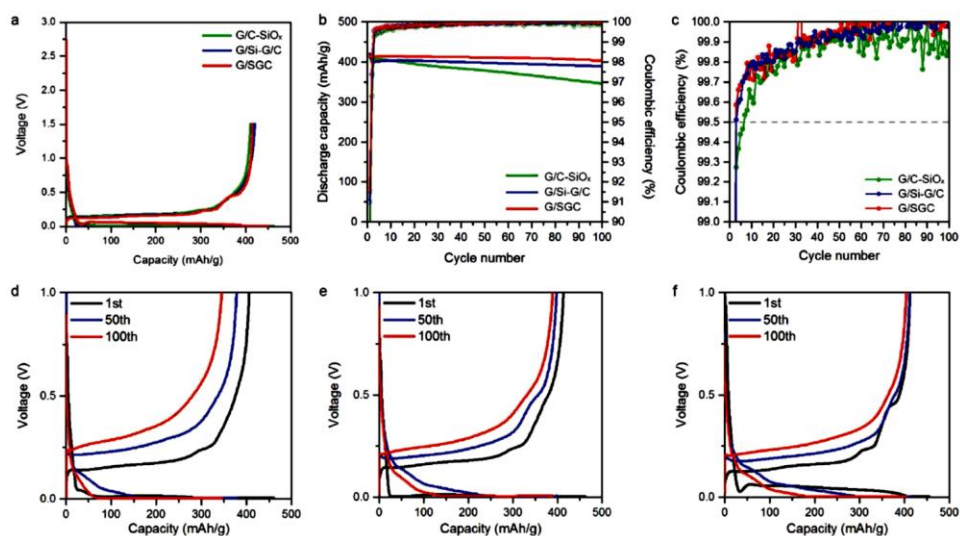


Figure 1.9 Electrochemical performances of G/C-SiOx, G/Si-G/C, and G/SGC in half-cell tests. (a) Voltage profiles of the first cycle. (b) Cycling performance at 0.5 C ($1\text{C} = 450 \text{ mAh g}^{-1}$). (c) Rescaled form of CE at each cycle. (d-f) Voltage profiles of (d) G/C-SiOx, (e) G/Si-G/C, and (f) G/SGC at the 1st, 50th, and 100th cycle. Ref [22]

To further test the cycling stability of three types of Si-based anode, each anode is paired with LiCoO₂ cathode²². As we know, there are excessive amount of lithium ions in a half-cell test as the thick lithium metal can provide lots lithium ions; while in the full-cell test, the lithium ions come from layered LiCoO₂ cathode and the total amount is fixed. In the full-cell, the LiCoO₂ cathode shows good cycling stability when pairing with graphite anode. When pairing Si-based anode with LiCoO₂ cathode, the full-cell cycling stability is determined by the cycling stability of Si-based anode. In **Figure 1-10a**, the full-cell with SGC anode shows the highest first cycle CE of 89.3%, as a comparison, the first cycle CE of full-cell with Si-G/C anode and C-SiOx anode are 88.0% and 85.9%. Figure 1-10b, the full-cell with SGC anode shows best cycling stability of 67.1% capacity retention after 400 cycles, and average full-cell CE is 99.9%. Interestingly, the full-cell with Si-G/C anode and C-SiOx anode shows fast capacity fading for 50 cycles, because the SEI

layer is not stable and the formation of new SEI layer traps lots of lithium ions, which result in low full-cell CE and fast capacity fading. As shown in Figure 1-10c, the CE of full-cell with SGC anode shows fast increase to 99.5% after 8 cycles; while CE of full-cell with Si-G/C anode and C-SiOx anode requires 22 cycles before reaching 99.5%.²²

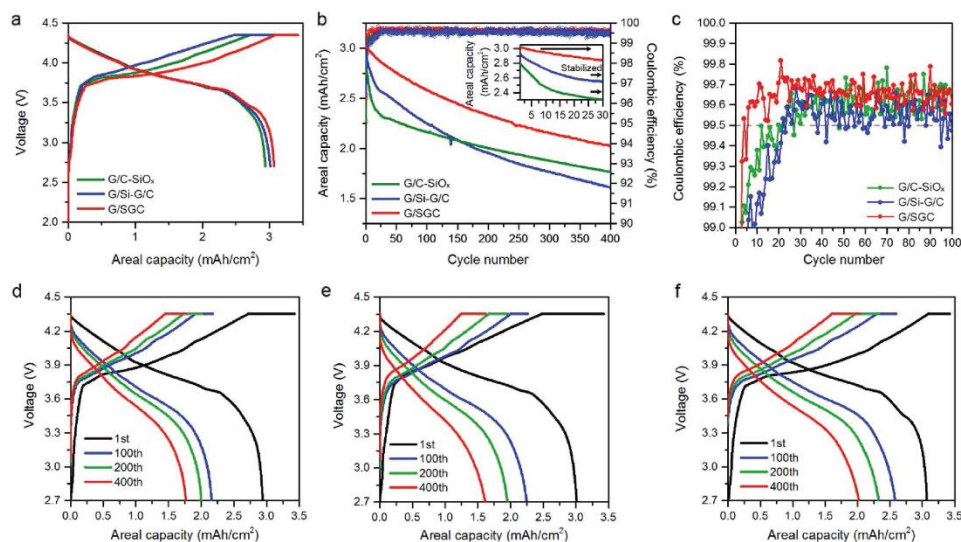


Figure 1. 10 Electrochemical performances of G/C-SiO_x, G/Si-G/C, and G/SGC in full-cell tests. (a) Voltage profiles of the first formation cycle. (b) Cycling performance at 0.5 C (1C = 450 mAh g⁻¹) for 400 cycles. (c) Rescaled form of CE at each cycle for 100 cycles. (d-f) Voltage profiles of (d) G/C-SiO_x, (e) G/Si-G/C, and (f) G/SGC at the 1st, 100th, 200th, and 400th cycle. Ref [22]

In summary, one major challenge of Si-based anode is the low full-cell CE of <99.9% and the resulting poor full-cell cycling stability. Even though some Si-based anode shows stable half-cell cycling stability, they shows poor cycling stability in full-cell test. Because the lithium metal anode always provides large amount of excessive lithium ions in half-cell. In order to evaluate the cycling performance of Si-based anode, both the half-cell and full-cell tests should be taken to evaluate the true cycling performance.

Chapter 2

Literature review on Si-based anode

2.1 Nanostructured Si active material and advanced functional polymer binder

Last decade has witness tremendous progress on solving huge volume change issue to improve the cycling stability and cycle life of Si anode. Great efforts has been devoted to develop nanostructured Si that can tolerate the volume change of Si and it will not crack during charge/discharge cycles. Another strategy is to develop functional polymer binder that can bind Si active material tightly to accommodate the volume change of Si and greatly improve the electrode structure integrity during charge/discharge cycles.

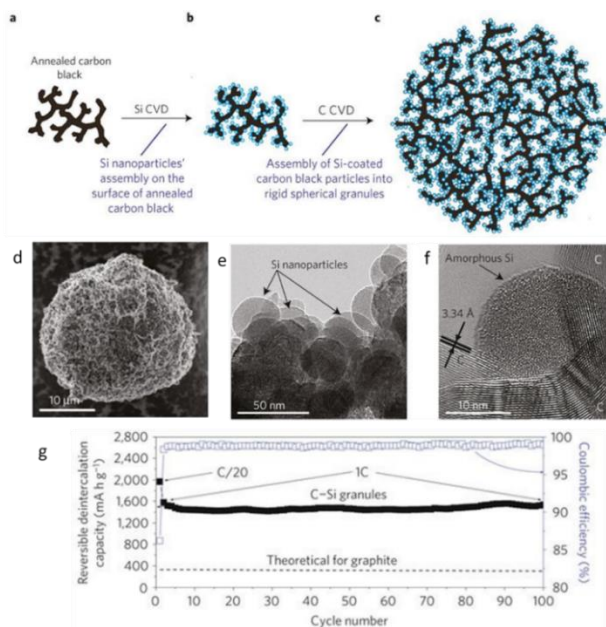


Figure 2. 1 Schematic of Si–C nanocomposite granule formation through hierarchical bottom-up assembly: Annealed carbon-black dendritic particles (a) are coated by Si nanoparticles (b) and then assembled into rigid spheres with open interconnected internal channels during C deposition (c). Morphology characterization of Si-C nanocomposite via SEM (e) and TEM (f and g) analysis. (g) Electrochemical chemical performance of Si-C nanocomposite. Ref [35]

The first strategy is to develop various silicon nanostructure to alleviate the pulverization of silicon particles. The nanostructured Si active material, including nanoparticles^{23,24}, nanowires¹⁰, porous Si^{25–29}, porous Si/carbon composite^{30–38}, and core-shell structure^{31–33,39,40}, are designed to accommodate volume change of Si, alleviate particle pulverization, and stabilize SEI layer to improve cycling stability. Yushin et al. reported the synthesis of micro-sized porous carbon/Si nanoparticles composite by CVD growth of Si nanoparticles into microporous carbon black and then assembling the Si-coated carbon black particles into rigid spherical granules as shown in **Figure 2-1**³⁵. There are three advantages of this type of cathode: the Si nanoparticles is 10-30 nm (Figure 2-1e and 2-1f); the particle's internal porosity allows large volume changes of Si on Li insertion and extraction; the carbon matrix provides fast electrons conduction pathway. As shown in Figure 2-1g, the Si/C composite electrode shows high first cycle CE of 85% and stable capacity of 1600 mAh g⁻¹ for 100 cycles³⁵.

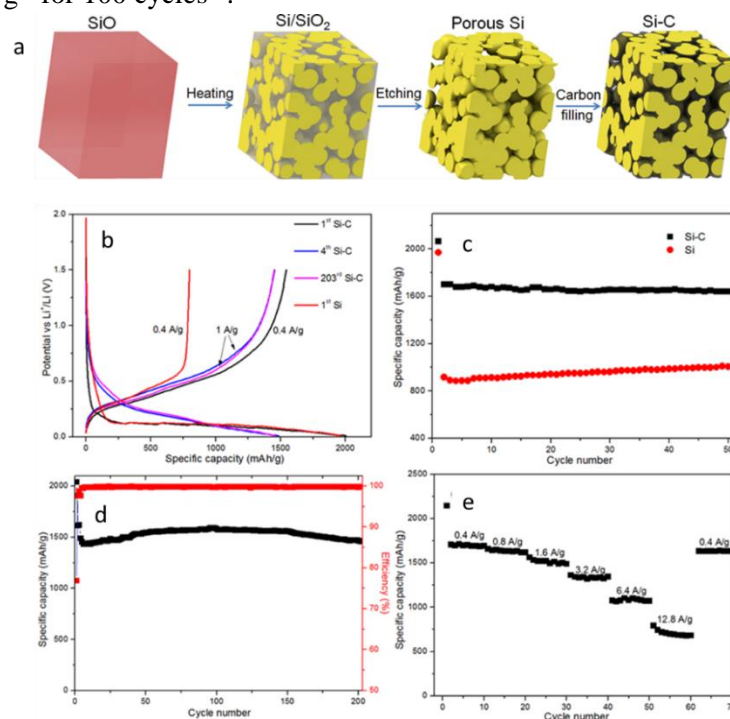


Figure 2. 2 Schematic of Si–C nanocomposite granule formation via three steps: heating at 950 °C for 6h; etching of SiO₂ with hydrofluoric acid; carbon coating via CVD decomposition of acetylene. (b) Voltage profile and (c-e) electrochemical performance of Si-C composites. Ref [37]

Previously we reported the synthesis of micro-sized Si-C composite composed of interconnected Si and carbon nanoscale building blocks as shown in **Figure 2-2a**.³⁷ In the first step, SiO undergo disproportionation at 950 °C to form Si nanoparticles embedded within SiO₂ matrix. Then after etching with hydrofluoric acid to remove SiO₂, it forms porous Si composed of interconnected nanocrystals. Finally, the porous Si is coated with carbon via decomposition of acetylene gas at 620 °C. The Si/C anode shows a reversible capacity of 1459 mAh g⁻¹ after 200 cycles at 1 A/g with a capacity retention of 97.8% after 200 cycles (Figure 2-2d)³⁷.

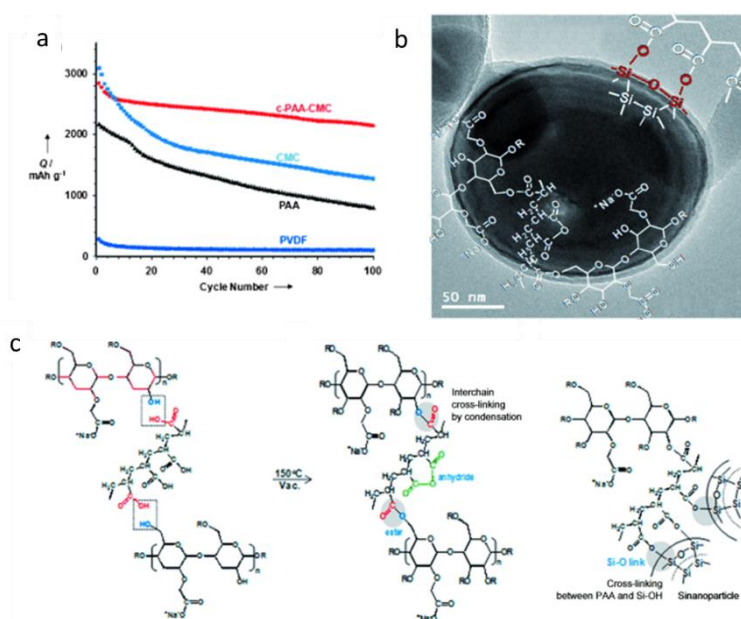


Figure 2. 3 (a) Electrochemical performance of Si nanoparticles electrode with c-PAA-CMC, CMC, PAA, and PVDF binder. (b) Chemical reaction between polymer binder and Si nanocrystals. (c) Formation mechanism of cross-linked PAA-CMC binder. Ref [54]

The second strategy is to develop a new polymer binder^{41–53}. The polymer binder plays an important role in large scale manufacturing of silicon electrode. To improve the cycling stability and cycle life of silicon anode, the polymer binder should bind strongly to silicon particle and becomes mechanically robust and strong via crosslinking to tolerate the huge volume change of silicon electrode. Previously, it is reported that the cross-linked polymer binder, like PAA

(polyacrylic acid)-NaCMC (sodium carboxymethylcellulose), PAA-PVA (polyvinyl alcohol) and PAA-polydopamine, can effectively improve the cycling stability of silicon anode^{54,55}. As shown in **Figure 2-3c** and **Figure 2-4b**, the carboxyl groups (-COOH) react with hydroxyl group (-OH) at high temperature to form ester bonds⁵⁴. In Figure 2-3a, the Si nanoparticles electrode with c-PAA-CMC binder shows the better cycling stability than electrode with CMC, PAA, and PVDF binder, with 80% capacity retention after 100 cycles. In Figure 2-4a, the Si nanoparticles electrode with PAA-PVA binder shows 80% capacity retention after 300 cycles⁵⁵. The improved cycling performance is ascribed to two reasons: polymer binder is rich of carboxyl group which form covalent ester bond with silanol group (-Si-OH) on the surface of silicon particle, as shown in Figure 2-3b and Figure 2-4b; the cross-linking of polymer binder can improve the mechanical property of whole silicon electrode to tolerate the huge volume change⁵⁵.

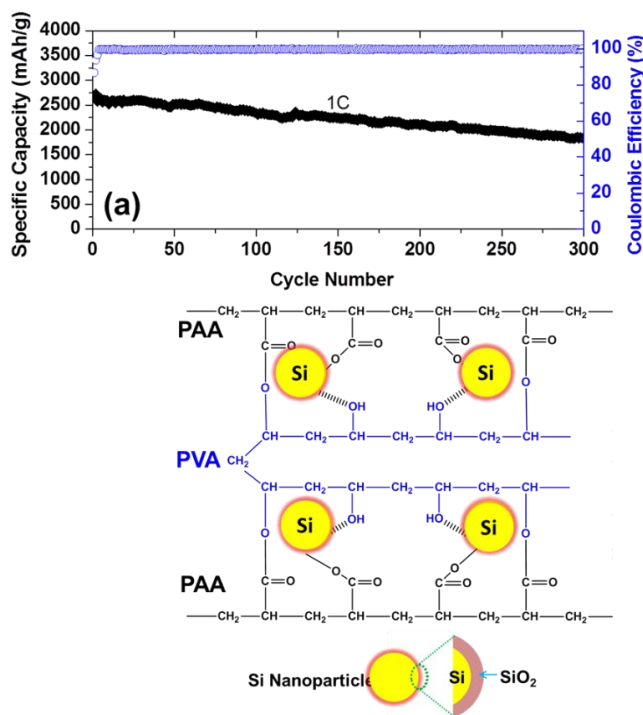


Figure 2. 4 (a) Electrochemical performance of Si nanoparticles electrode with c-PAA-PVA binder. (b) Formation mechanism of cross-linked PAA-CMC binder, including chemical reaction between polymer binder and Si nanocrystals. Ref [55]

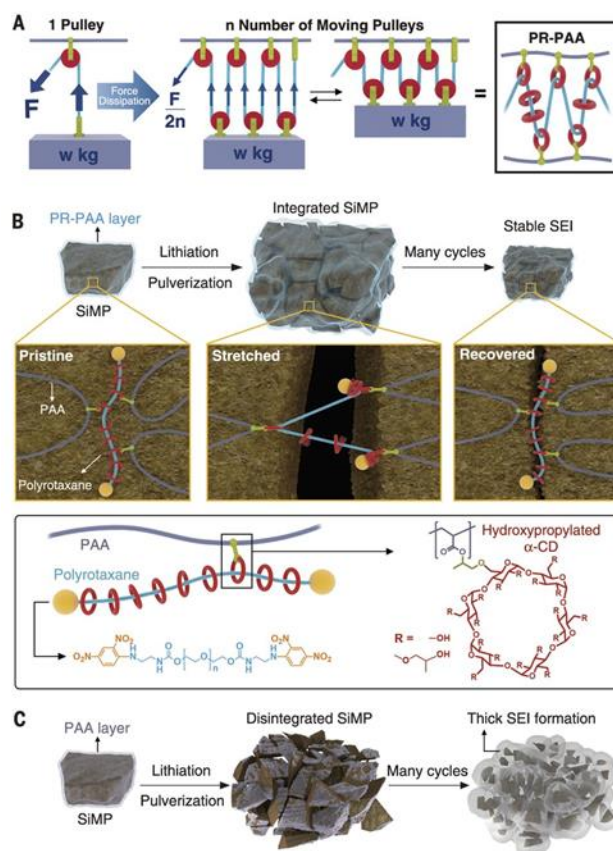


Figure 2. 5 Proposed stress dissipation mechanism of PR-PAA binder for SiMP anodes. (A) The pulley principle to lower the force in lifting an object. (B)The PR-PAA binder can keep the SiMP electrode integrated after long-term cycling. (C) The PAA binder cannot keep the pulverized Si particles integrated and result in thick SEI formation. Ref [56]

Another example is highly elastic binders integrating polyrotaxanes for silicon microparticles anodes⁵⁶. As shown in Figure 2-5b, the polyrotaxanes is prepared by self-assembly of polyethylene glycol (PEG) threads and α -cyclodextrin (α -CD) rings via supramolecular interaction. The outer surface of α -CD is hydrophilic while the inner surface is hydrophobic. The PEG chain is hydrophobic, thus it can go into α -CD rings. After reacting PEG two ends with big molecules, the α -CD rings cannot move out of PEG chain. Then PAA binder is cross-linked with 5 wt% of polyrotaxanes to form cross-linked polymer binder (PR-PAA). Even though some of the polyrotaxane's ring components are covalently bonded to the PAA chains, they can still move

freely along the thread PEG, thus serving like molecular pulleys to lower the tension on the PAA chains⁵⁶. As shown in Figure 2-5b, the elastic and stretchable polymer binder can help maintain electrode structure integrity and improve SEI layer stability; as a comparison in Figure 2-5c, the conventional PAA binder cannot hold the cracked Si particles tightly and some exposed new surface will react with liquid electrolyte to form new SEI layer during cycling, leading to deintegrated Si electrode with damage of electrode structure integrity⁵⁶.

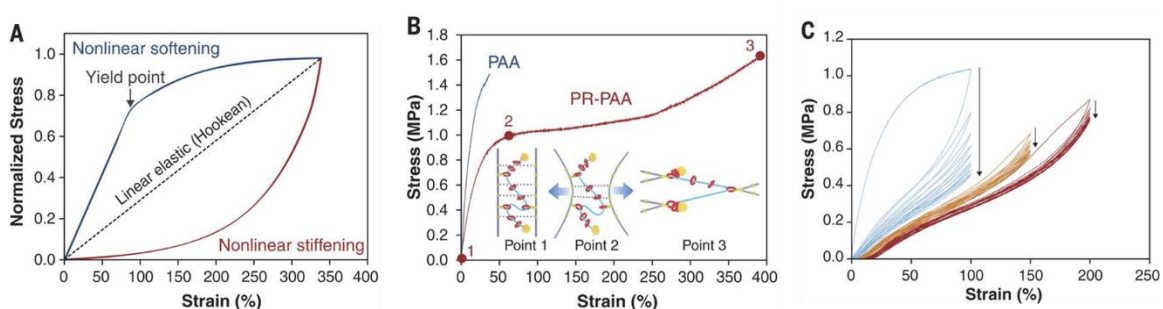


Figure 2. 6 Mechanical properties of PR-PAA and PAA. (A) Stress-strain behaviors of three representative modes. (B) Comparison of stress-strain curves of PR-PAA and PAA films at three strain points. (C) Stress-strain curves of PR-PAA for 10 stretch-recovery cycles with different strain limits. Ref [56]

Figure 2-6 shows the mechanical property of pure cross-linked polymer binder PR-PAA film⁵⁶. As shown in Figure 2-6B, the PAA film exhibits an r-shaped curve in strain-stress curve, and it ruptures at a strain of 37%. In comparison, the PR-PAA can tolerate much larger strain of 390% until rupture. The strain-stress curve of PR-PAA exhibits two regions: in the first region between point 1 and point 2, the PAA chain can rearrange along the load direction with some breaking of hydrogen bonds; in the second regions between point 2 and point 3, the ring sliding of polyrataxanes starts to happen and it can largely release the loading stress. The entropic repulsion between agglomerated α -CD rings endows the polymer film with sufficient resilience to follow the same trajectory in the opposite direction of strain. When the stretch-recovery cycles were repeated

in the sequence of 100, 150, and 200% strain limits, the PR-PAA film showed robust behavior in Figure 2-6C.⁵⁶

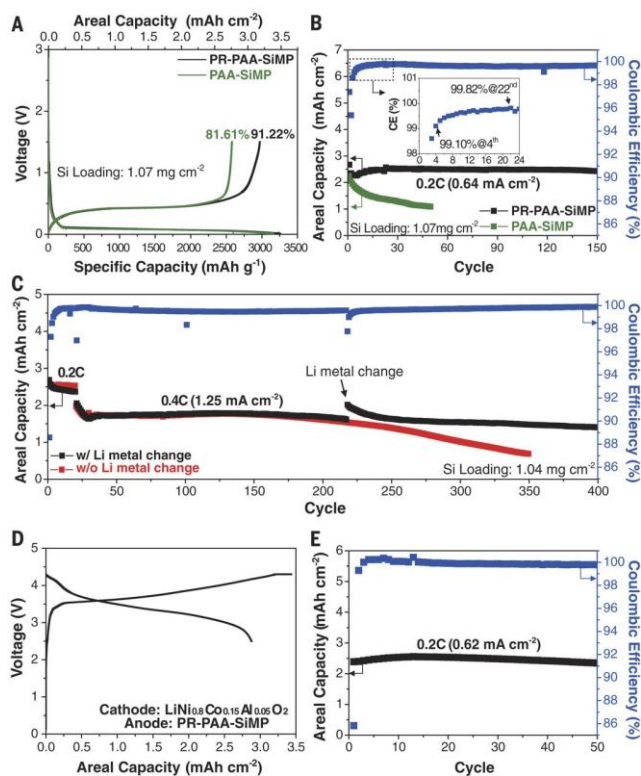


Figure 2. 7 Electrochemical performances of SiMP electrodes with PR-PAA and PAA as binders. (A) Voltage profiles of half-cell for the first cycle. (B) Cycling performance at 0.2C and the CE of electrode with PR-PAA binder. (C) Cycling performance at 0.4C with/without lithium metal change after 200 cycles. (D) The initial charge-discharge profile of the SiMP- LiNi_{0.8}Co_{0.15}Al_{0.05}O₂ full-cell at 0.03C (1C = 190 mA g⁻¹ NCA) and (E) its cycling performance at 0.2C. The n/p ratio based on the capacities of both electrodes is 1.15. Ref [56]

The PR-PAA binder enables Si microparticles anode with excellent half-cell cycling stability⁵⁶. In **Figure 2-7A**, the electrode with PR-PAA binder shows high areal capacity of 3.18 mAh cm⁻² with high first cycle CE of 91.6%, while the electrode with PAA binder shows a first cycle CE of 86.1%. In Figure 2-7B, the electrode with PR-PAA binder shows a stable areal capacity

of 2.6 mAh cm⁻² for 150 cycles, while the electrode with PAA binder fast to 1.0 mAh cm⁻² within 50 cycles. More interestingly, after replacing with a new lithium foil in Figure 2-7C, the electrode with PR-PAA binder shows even longer cycling stability to 400 cycles. In Figure 2-7D, when paring the Si anode with NCA cathode at an N/P ratio of 1.15, the full-cell show high discharge capacity of 2.9 mAh cm⁻² with a first cycle CE of 86%. More Figure 2-7E shows decent cycling stability with 98% capacity retention after 50 cycles. One interesting question is how the long-term cycling stability of the full-cell. If the full-cell started to fade after 50 cycles, it indicated that the SEI layer starts to crack and the formation of new SEI layer result in large amounts of lithium irreversible loss⁵⁶.

2.2 How to improve electrode structure integrity for long-term cycling?

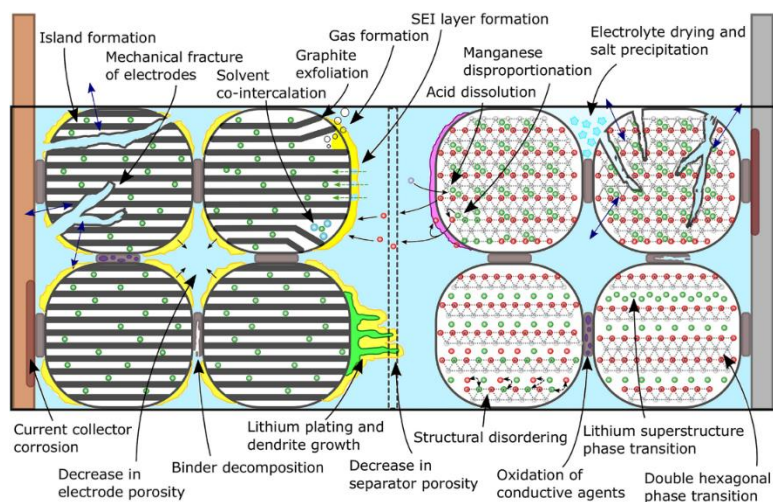


Figure 2. 8 Schematic of key degradation mechanisms in a lithium-ion battery. Graphitic carbon negative electrode on the left. Lithium metal oxide structure on the right. Separator mesh layer in the middle. Green for lithium. Red for metal. Blue for electrolyte. Ref [57]

The electrode structure integrity is of great importance on long-term cycling stability for both cathode and anode of Li-ion battery. The working mechanism of Li-ion battery requires lithium ions diffusion between cathode and anode electrodes, lithium ion diffusion within cathode/anode electrodes, and the electrons transportation within cathode/anode electrodes to external circuit, as shown in **Figure 2-8**.⁵⁷ Both the cathode and anode electrodes consist of thousands of particles of active material and conductive carbon with polymer binder binding them together. The tap density of electrode is lower than the true density even after mechanical pressing on electrode. As a result, the electrode always has some porosity that can be filled with liquid electrolyte for lithium ions conduction. Meanwhile, the uniform mixing of conductive carbons and active material forms three dimensional conductive network for electrons conduction within the electrode⁵⁷. The raw electrode always has good electrode structure integrity for both lithium ions conduction and electrons transportation.

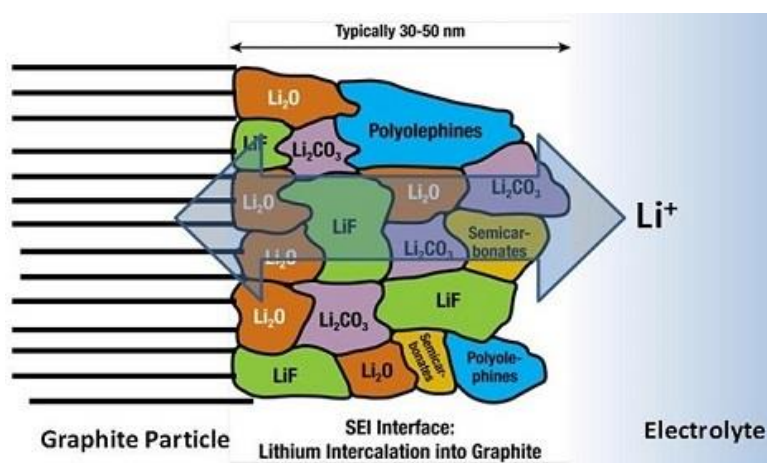


Figure 2. 9 Schematic solid electrolyte interphase (SEI) layer on graphite anode. Ref [59]

However, when charging Li-ion battery full-cell to high cut-off voltage, the electrochemical potential of anode goes below 0.1 V (Vs. Li⁺/Li), which is lower than the reduction potential of liquid electrolyte, then liquid electrolyte will decompose to form a passivation layer on outer and inner surface of whole electrode⁵⁸. The passivation layer is called SEI (solid electrolyte interphase) layer. As shown in **Figure 2-9**, the SEI layer is composed of inorganic lithium salts and some organic species⁵⁹. It can prevent electrolyte from further decomposition on anode, when the thickness grows to 30-50 nm. For graphite anode, the volume change during charge/discharge process is only 10%. By carefully tune the electrolyte composition with certain types of electrolyte additives, after several formation cycles and aging process, the SEI layer can be very stable against its volume change during following cycles. As a result, the full-cell CE can reach as high as 99.98% and the capacity retention drops below 80% after 1115 cycles.

However, for Si-based anode, the volume change during charge/discharge process is 400% for Si and 150% for SiO. The SEI layer cannot tolerate such large volume change that it will crack and new SEI layer will form on the freshly exposed active material surface. At particle level, in **Figure 2-10a**, the large volume change will generate large strain and stress that cause particle

pulverization after many cycles⁶⁰. At electrode level, in Figure 2-10b, the large volume change will cause large change in electrode thickness. The uneven strain distribution within the electrode will cause electrode to crack. Both particles pulverization and electrode cracking will generate new active material surface, as shown in Figure 2-10c. The new SEI layer will form in each charge/discharge cycles, leading to low full-cell CE. The continuous SEI layer cracking and formation of new SEI layer will damage electrode structure integrity: some parts of electrode will delaminate from bulk electrode and then they will be fully covered with insulate SEI layer; the accumulated growth of SEI layer will increase interfacial impedance and block lithium ions transport⁶⁰. Either loss of electrical conduction pathway or Li^+ ions conduction pathway will damage electrode structure integrity.

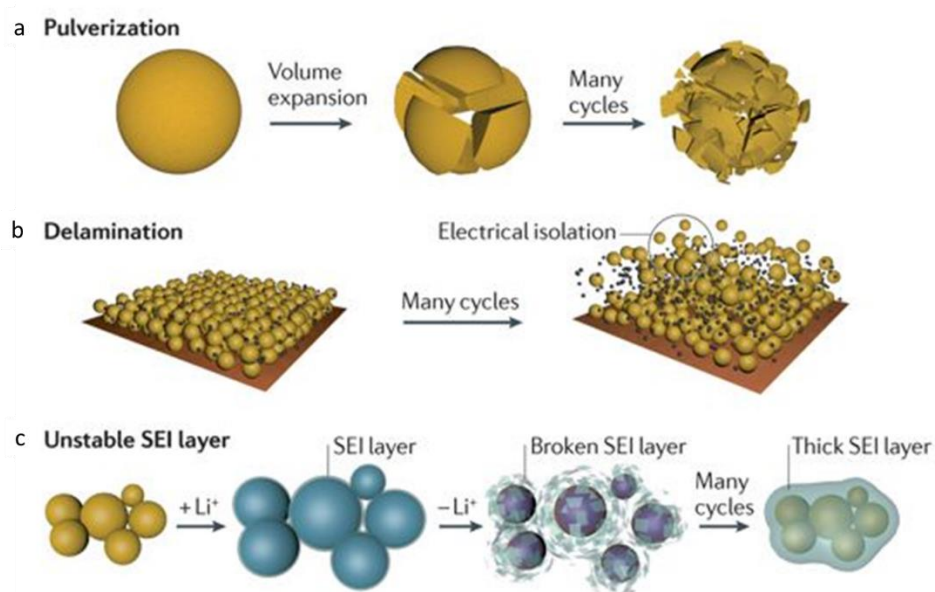


Figure 2. 10 Damage of electrode structure integrity. (a) Particle pulverization; (b) Electrode cracking and delamination; (c) Accumulated growth of SEI layer. Ref [60]

The damage of electrode structure integrity not only exists on anode side with large volume change, but also exists on cathode side. When charging Li-ion battery full-cell to high cut-off voltage, the electrochemical potential of cathode goes above 4.2 V (Vs. Li^+/Li). Although it is still

below the oxidation potential of liquid electrolyte (4.5 V), the liquid electrolyte will decompose to form a passivation layer on whole cathode via some catalytic reactions⁶¹. The passivation layer is called CEI (cathode electrolyte interphase), as shown in **Figure 2-11**.

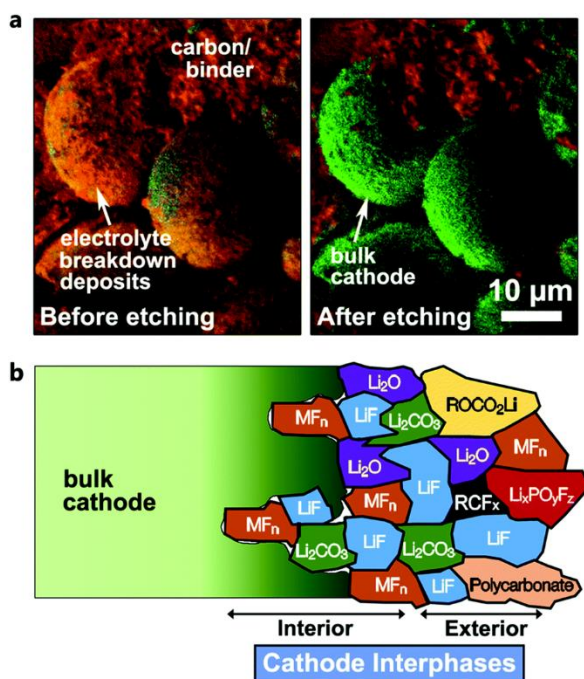


Figure 2. 11 Morphology and composition of cathode electrolyte interphase (CEI) at cathode surface: (a) TOF-SIMS mapping on $\text{LiNi}_{0.7}\text{Co}_{0.15}\text{Mn}_{0.15}\text{O}_2$ composite electrode after cycling, and (b) a schematic illustration. Ref [61]

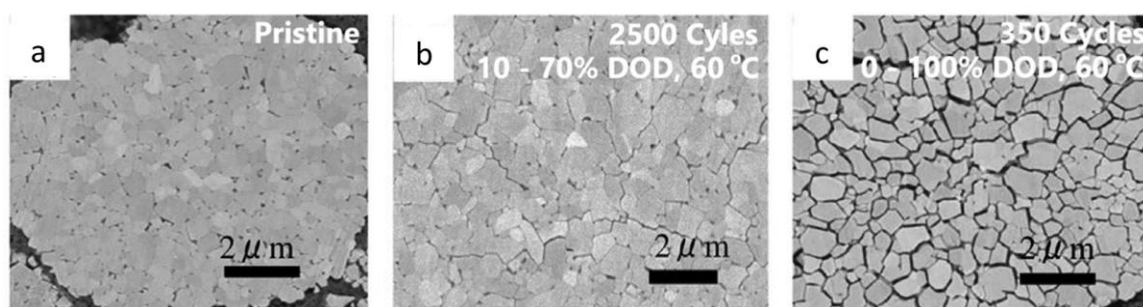


Figure 2. 12 Crack formation and pulverization of $\text{LiNi}_{0.76}\text{Co}_{0.14}\text{Al}_{0.10}\text{O}_2$ cathode at different depth of discharge (DOD) cycles. (a) pristine cathode; (b) cathode after 2500 cycles with 10-70% DOD at 60 °C; (c) cathode after 350 cycles with 0-100% DOD at 60 °C. Ref [61]

The NCM cathode is composed of secondary particles which consists of primary single crystals with an average size 0.5 μm . The secondary particles show lots of grain boundaries and voids space, as shown in **Figure 2-12a**. One challenge of NCM cathode is that the anisotropic volume change arise non-uniform strain during charge/discharge cycles⁶¹. The non-uniform stain will generate stress to the secondary particles during charge/discharge cycles. After repeated cycles, as shown in Figure 2-12b and 2-12c, the secondary particles tend to crack and undergo pulverization, which will damage the electrode structure integrity: the pulverized particles show new active surface to react with liquid electrolyte to form new cathode electrolyte interface (CEI) layer; the continuous formation of CEI layer will finally block lithium ions transportation and electrons conduction⁶¹.

In order to improve electrode structure integrity, one effective way is to prevent electrode particles from cracking through a robust and strong coating strategy. However, as to Si particles, the volume change during charge/discharge process is 400%, while the volume change of cathode is only 5-10%. The coating layer cannot tolerate such large volume change of Si. Thus the coating strategy may not work for Si. To make it work, people have developed a yolk-shell structure of Si nanoparticles embedding in a robust carbon or TiO_2 shell^{31-33,39,40}. The designed void space allow Si particles to expand/shrink without damage the protective shell. The coating shell can be carbon or TiO_2 .

As shown in **Figure 2-13a**, the Si@TiO_2 yolk-shell structure is prepared via three steps: in the first step, Si nanoparticles are coated with amorphous carbon using glucose as carbon resource via hydrothermal reaction; in the second step, the carbon coated Si nanoparticles are coated with TiO_2 precursor; in the third step, after calcination at high temperature in air, the carbon shell is gone and the TiO_2 precursor turn into anatase shell, as shown in Figure 2-13c and Figure 2-13g. The yolk-shell structure is characterized with STEM element mapping in Figure 2-13b. The weight ratio between Si and TiO_2 is 73:27.³⁹

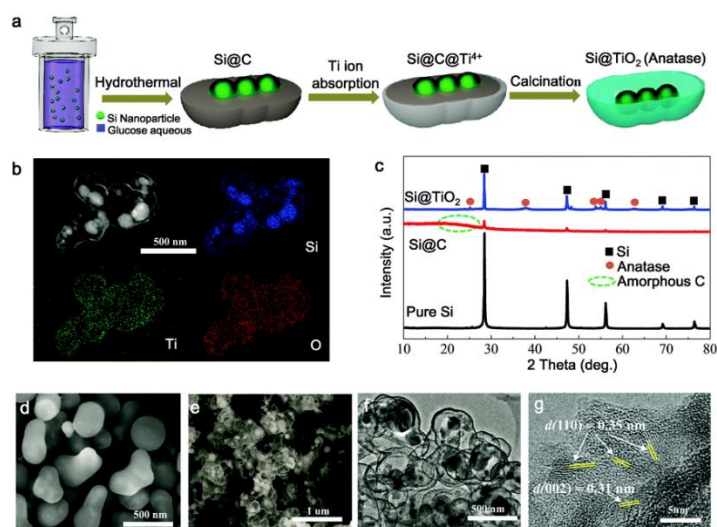


Figure 2. 13 Fabrication and characterization of the yolk–shell Si@TiO₂ cluster electrode. (a) Schematic of the synthesis of the yolk–shell Si@TiO₂ cluster. (b) STEM image and elemental mapping of Ti, O and Si, confirming the yolk–shell structure. (c) XRD data of the commercial silicon nanocrystals, Si@C after hydrothermal treatment and the as-obtained Si@TiO₂ after 550 °C heat treatment in air. (d) SEM image of Si@C@TiO₂ after titanium ion adsorption. (e and f) SEM and TEM images of the yolk–shell Si@TiO₂ cluster after heating at 550 °C in air for 2 h. (g) High resolution TEM image of TiO₂ shell. Ref [39]

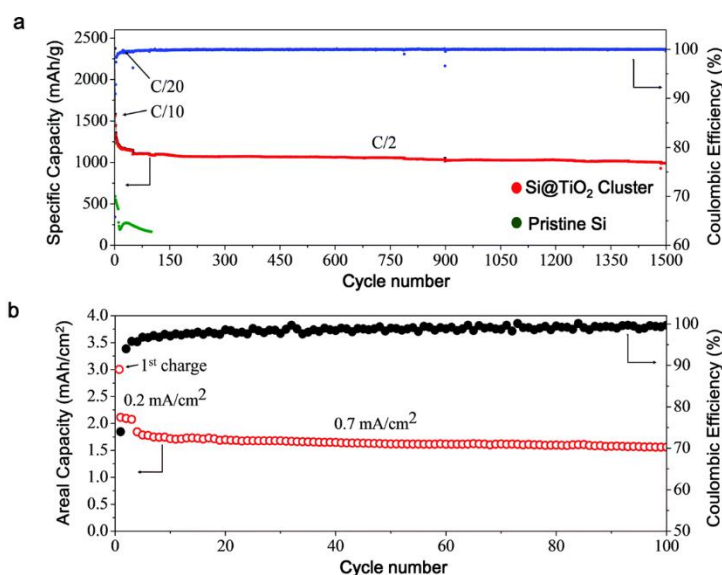


Figure 2. 14 Electrochemical characterization of the Si@TiO₂ yolk-shell anode. (a) Half-cell cycling performance and the corresponding coulombic efficiency for 1500 cycles. The mass loading of all active materials was about 0.8 mg cm⁻². (b) Full-cell performance of the Si@TiO₂ yolk-shell anode (2.1 mg cm⁻²) paired with a lithium cobalt oxide cathode. Ref [39]

The electrochemical performance of Si@TiO₂ yolk-shell anode is shown in **Figure 2-14a**. The half-cell shows first discharge capacity of 2374 mAh g⁻¹ and charge capacities of 1562 mAh g⁻¹, respectively, giving an initial cycle CE of 65.8%. The low first cycle CE indicates that liquid electrolyte still can penetrate into TiO₂ shell and Si nanoparticles have large surface area to react with liquid electrolyte. The half-cell shows good cycling stability with 950 mAh g⁻¹ after 1500 cycles. In Figure 1-14b, the Si@TiO₂ yolk-shell anode is paired with LiCoO₂ cathode. The first charge capacity is as high as 3.0 mAh cm⁻². But it drops quickly to 2.0 mAh cm⁻² due to the low first cycle CE of Si@TiO₂ yolk-shell anode. Then the full-cell capacity drops to 1.6 mAh cm⁻² after 100 cycles with 80 % capacity retention³⁹.

The design of yolk-shell structure helps to improve electrode structure integrity, while it encounter some issues. Firstly, the first cycle CE is low, as liquid electrolyte can penetrate into shell and react with Si active material to form large amount of SEI layer. Secondly, the full-cell CE is low, because the Si nanoparticles undergo pulverization and the liquid electrolyte can still reach to pulverized particles to form new SEI layer.

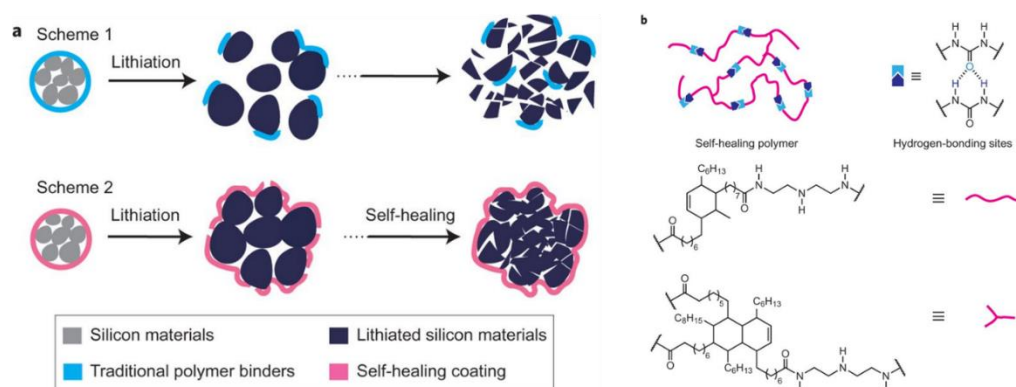


Figure 2. 15 (a) Scheme 1: schematic illustration of the design and behavior of a conventional silicon electrode. Scheme 2: schematic illustration of the design and behavior of the stretchable self-healing electrode. (b) Chemical structure of the self-healing polymer (SHP). Ref [63]

Another strategy to improve electrode structure integrity is to coat polymer layer on the top of Si electrode. For example, a self-healing polymer is adopted on Si microparticles electrode^{62,63}. As shown in Figure 2-15, when Si particles undergo large volume during

lithiation/delithiation and get pulverized after many cycles, the conventional polymer binder cannot bind and keep the pulverized particles integrated; while the self-healing polymer can help maintain the pulverized particles integrated without losing conductive network⁶³.

The self-healing polymer mixing with conductive carbons was coated on the Si electrode via heating it to melt at high temperature and pressing it into electrode with a sharp blade⁶³. The pristine electrode was composed of Si microparticles with average size of 4.2 μm . After polymer coating, the electrode showed a flat morphology and the cross-sectional SEM images showed that the polymer layer exists both on the top of electrode and go into the electrode. After 20 electrochemical cycles, the electrode surface became rough and had a continuous wave-like structure, which is caused by Si microparticles large volume expansion and extraction during lithiation/delithiation⁶³. The electrode crack started heal itself after resting it for 5 hours.

The design self-healing chemistry is effective on maintaining electrode integrity. However, the polymer coating amount is too much ($0.5\text{-}0.7\text{ mA cm}^{-2}$) which is the same weight to the loading Si active material. As a result, the electrode cannot cycle well at high current density and shows poor rate performance. Also, the coating process is difficult for large-scale production of electrode.

Chapter 3

A stretchable intra-electrode cushion for high-loading silicon monoxide anodes in lithium-ion batteries

Abstract

Si-based anode has been considered as next generation of advanced anode material to improve the specific energy and energy density of Li-ion battery. However, high-areal-capacity Si-based anode still encounters fast capacity fading issue, because large volume change of Si upon lithiation/delithiation will damage electrode structure integrity and arise accumulated growth of SEI (solid electrolyte interface) layer. Here we develop an elastic and stretchable polyurethane-urea (PUU) gel polymer electrolyte (GPE) coating strategy to improve cycling stability of high-areal-capacity SiO anode. The PUU GPE functions as intra-electrode cushion to accommodate the volume change of SiO electrode. It can alleviate electrode thickness change, inhibit electrode cracking, and improve electrode adhesion strength on Cu current collector. The improved electrode structure integrity reduces the continuous growth of SEI layer. The half-cell of SiO electrode with PUU coating shows a reversible capacity of 3.0 mAh cm⁻² for 280 cycles. When paring with commercial cathode, the full-cell shows a reversible capacity of 2.1 mAh cm⁻² for 200 cycles and 80% capacity retention for 500 cycles with improved full-cell Coulombic efficiency of 99.9%.

3.1 Introduction

Nowadays lithium-ion battery has been widely used in portable electronics, electric vehicles, and grid energy storage devices^{2,64,65}. To increase the energy density of lithium-ion battery, great efforts has been devoted to develop high-capacity cathode and anode materials^{13,15,66}. Silicon is one type of promising anode material, as it shows a high theoretic capacity of 4200 mAh g⁻¹, which is 10 times higher than that of conventional graphite anode (370 mAh g⁻¹); meanwhile it also shows a relatively low average potential (0.4 V vs. Li⁺/Li)^{24,66}. However, huge volume change of Si particle (>300%) during repeated lithiation/delithiation process will arise particle pulverization, electrode cracking or delamination, and continuous growth of SEI layer, resulting in damage of electrode structure integrity and fast capacity fading.

Last decade has witness tremendous efforts and progress to improve cycling stability of Si-based anode. Careful optimization has been undertook for all electrode components, including Si active material^{21,67-70}, polymer binder⁴¹⁻⁵³, conductive carbon, and current collector⁷¹. The nanostructured Si active material, including nanoparticles^{23,24}, nanowires¹⁰, porous Si²⁵⁻²⁹, porous Si/carbon composite³⁰⁻³⁸, and yolk-shell structure of Si nanoparticles embedding in a robust carbon or TiO₂ shell^{31-33,39,40}, are designed to accommodate volume change of Si, alleviate particle pulverization, and stabilize SEI layer to improve cycling stability. Besides, polymer binder also play an important role to tightly bind Si active material and maintain electrode structure integrity⁴²⁻⁴⁶. Recently, a highly elastic binders integrating polyrotaxanes and polyacrylic acid binder can accommodate the large volume change of Si microparticles and keep even pulverized Si particles coalesced without disintegration, enabling stable cycle life for high-areal-capacity anode in both half-cell and full-cell tests⁵⁶.

However, for high-areal-capacity Si-based anode, it exhibits large change in electrode thickness during charge/discharge process. The electrode cracking or delamination starts to happen

when interparticle displacement is large and polymer binder cannot pull back active particles to their original position. The repeated electrode swelling and contraction will damage electrode structure integrity: Si particle pulverization is unavoidable; some pulverized particles may lose conductive network and some parts of electrode may get cracked or delaminate; the unavoidable particle pulverization and electrode cracking or delamination will generate new active surface to react with liquid electrolyte to form new SEI layer. Either loss of electrical conduction pathway or Li^+ ions conduction pathway will damage electrode structure integrity and lead to fast capacity fading. The accumulative growth of SEI layer will trap lots of lithium ions and cause large irreversible capacity loss, resulting in fast capacity fading in full-cell with limited amount of Li^+ ions.

To maintain electrode structure integrity and stabilize SEI layer, a self-healing polymer has been applied to coat on the top of Si microparticles electrode enabling stable cycling at 3.0 mAh cm^{-2} for 120 cycles, however, the rate performance is not good and the relative amount of coating polymer is too much^{62,74}. Another example is to embedding nanostructured Si embedding within 3D carbon matrix for conduction of both electrons and Li^+ ions, however it requires lots of polymer for the carbonization which is not cost-effective^{70,75,76}.

Here we design an elastic and stretchable PUU (polyurethane-urea) polymer cushion and evenly distribute it within SiO electrode via simple slurry coating approach. The elasticity and stretchability of PUU polymer cushion is determined by its unique molecular structure with repeated soft and hard domains. It functions as intra-electrode cushion to accommodate large volume change of electrode and help improve electrode structure integrity. At electrode level, it can alleviate electrode thickness change during repeated electrode swelling and contraction; it can prevent electrode cracking or delamination; it can improve the electrode adhesion strength on Cu current collector to prevent electrode peel-off. The PUU coating can restrict the pulverized particles and conductive carbon in electrical contact to prevent loss of conductive network. The improved

electrode structure integrity inhibits the formation of new particle surface and electrode surface, accompanied by less formation of new SEI layer. Hence the PUU polymer cushion enables SiO electrode with a stable areal capacity of 3 mAh cm^{-2} for 280 cycles. More interestingly, the full-cell of NMC ($\text{LiNi}_{0.5}\text{Mn}_{0.3}\text{Co}_{0.3}\text{O}_2$) / prelithiated SiO electrode shows a reversible capacity of 2.1 mAh cm^{-2} for 200 cycles and 80% capacity retention for 500 cycle.

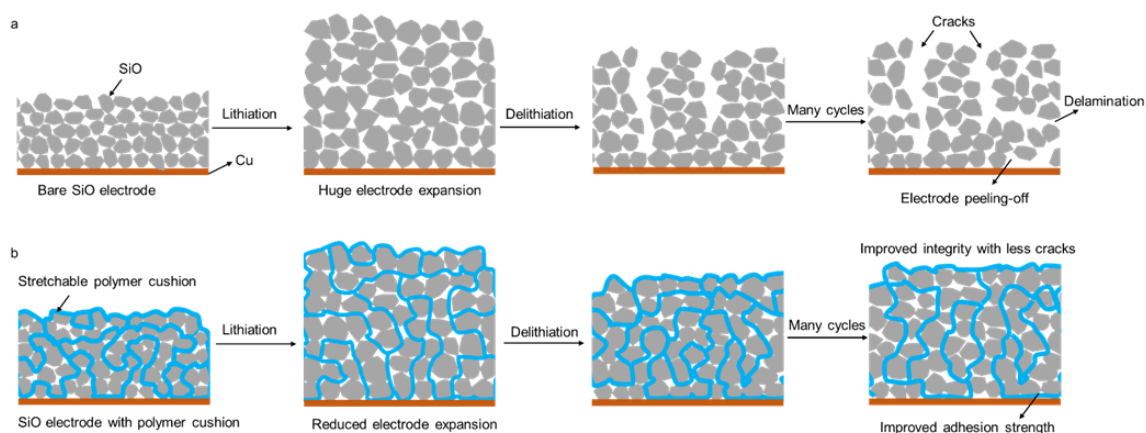


Figure 3. 1 Schematic illustration of the improved integrity of a SiO electrode enabled by the use of a PUU polymer cushion. (a) For bare SiO electrode, large volume change arises a huge electrode expansion upon lithiation, causes electrode cracking, and even peeling-off current collector after many cycles. (b) The stretchable PUU polymer cushion can reduce the electrode expansion upon lithiation, alleviate electrode cracking and delamination, and prevent electrode peeling-off from current collector after many cycles.

3.2 Characterization of PUU polymer

The PUU polymer was synthesized via chain condensation reaction between isocyanate and hydroxyl/amine groups (details in **Figure 3-2** and experimental section) following two steps: firstly, 2 mmol of methylene diphenyl diisocyanate (MDI) and 1 mmol of poly(tetramethylene ether) glycol (PTMG, $M_w = 2900$) was mixed in dimethylacetamide (DMAc) and the solution was kept at 80°C for 4h to form PTHF-2DMI with two isocyanate end groups; secondly, after cooling the solution to room temperature, equal mole ethylene diamine(EDA) was added under vigorous

stirring and the solution was heated up and kept at 80 °C for 4h. The molecular structure of PUU polymer is shown in Figure 2-2 and the given chemical identity was verified by its Fourier transform infrared (FTIR) spectrum (**Figure 3-3**). The existence of urethane and urea groups and disappearance of isocyanate groups indicated reaction between isocyanate and hydroxyl/amine groups. Also the solution viscosity became very high after the addition of EDA and sometimes it turned into gel. Besides, the GPC (gel permeation chromatography) analysis showed that the PUU polymer has a molecular weight of 4.0×10^4 with a polydispersity index of 2.94.

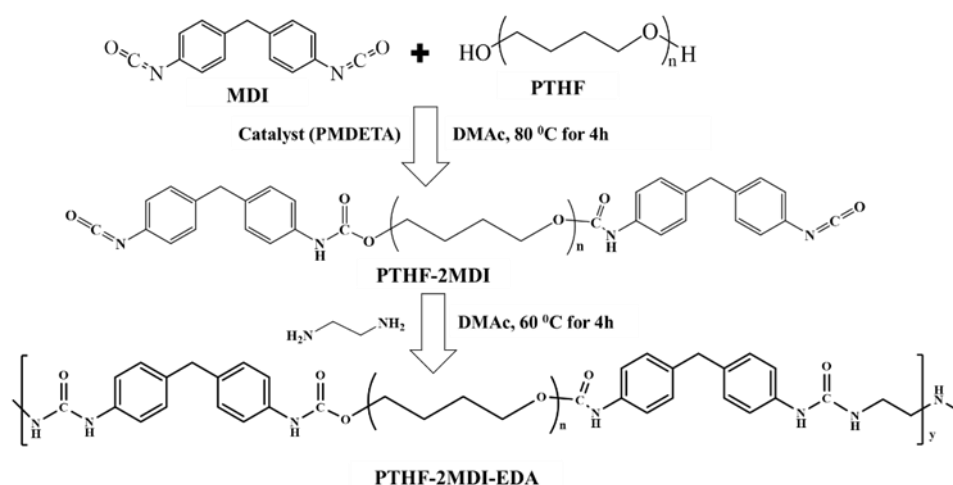


Figure 3. 2 Schema of synthesis of polyurethane-urea (PUU) polymer.

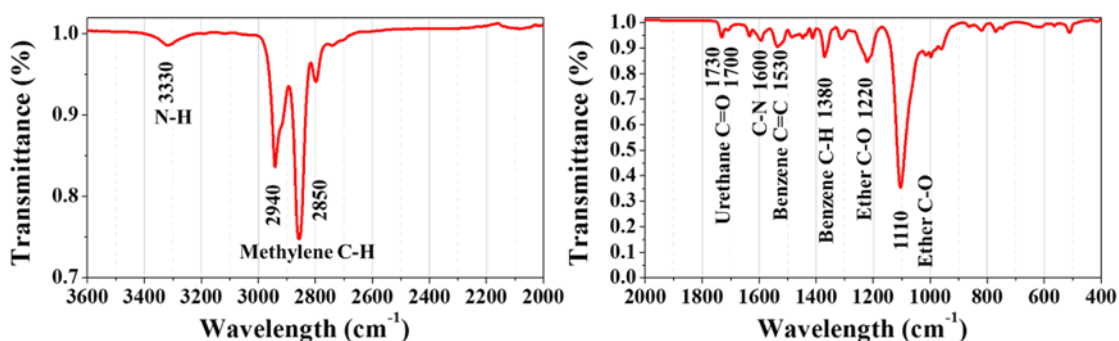


Figure 3. 3 Fourier transform infrared (FTIR) spectrum of PUU polymer.

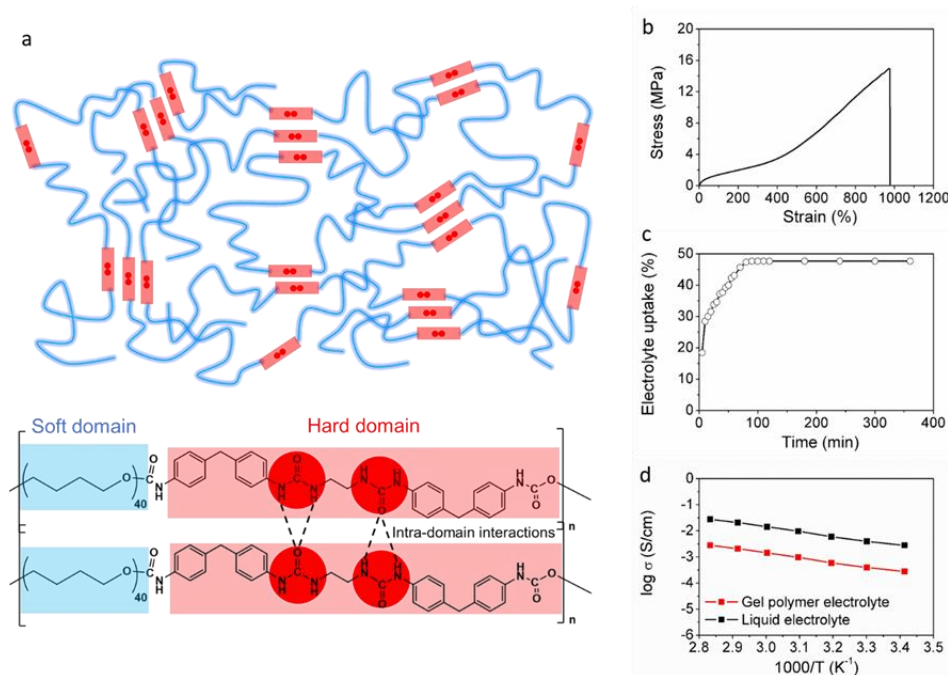


Figure 3. 4 Structure and mechanical and physical properties of PUU cushion polymer. (a) Structure of PUU cushion polymer, which contains poly(tetramethylene ether) glycol (PTMG) as soft domains and (4,4'-methylene diphenyl diisocyanate)-ethylenediamine (MDI-EDA) as hard domains. There are intra-domain interactions (hydrogen bonding and π - π interactions) between hard domains. (b) Stress-strain curve of PUU cushion polymer. (c) Swelling experiment of PUU cushion polymer membrane in a 1 M LiPF₆ in EC/DEC electrolyte. (d) Ionic conductivity of the formed gel polymer electrolyte and liquid electrolyte as a function of temperature.

The molecular structure of PUU cushion polymer is shown in **Figure 3-4a**, it is composed of two domains: the soft long-chain poly(tetramethylene ether) glycol (PTMG) domain can swell in carbonate electrolyte to form gel polymer electrolyte with good ionic conductivity; the hard domain contains lots of carbamate and urea groups to form hydrogen bonds with each other. The unique molecular structure of repeated soft and hard domains enables PUU cushion polymer with good elasticity and stretchability. Upon stretching, the coiled PTMG chains are aligned along the elongation direction. Once the elongation force is released, the strong hydrogen bonds between urethane and urea groups in hard domains enable polymer chain to return to its original dimension.

As shown in Figure 3-4b, the strain-stress curve shows the rubbery property of PUU membrane, which can tolerate more than 900% elongation upon stretching.

Figure 3-4c shows swelling experiment of PUU cushion polymer in liquid electrolyte of 1M LiPF₆ in EC/DEC (1:1 v/v). The weight of PUU cushion polymer increased quickly within 100 minutes and then got saturated with liquid electrolyte. The PUU cushion polymer can swell and uptake 48 wt% liquid electrolyte. The resistance of PUU cushion polymer GPE was measured via AC impedance method (**Figure 3-5**). The ionic conductivity (σ) is calculated based on Ohm's Law. In Figure 3-4d, the PUU cushion polymer GPE shows an ionic conductivity of $2.4 \times 10^{-4} \text{ S cm}^{-1}$ at room temperature, which is than comparable to that of corresponding liquid electrolyte.

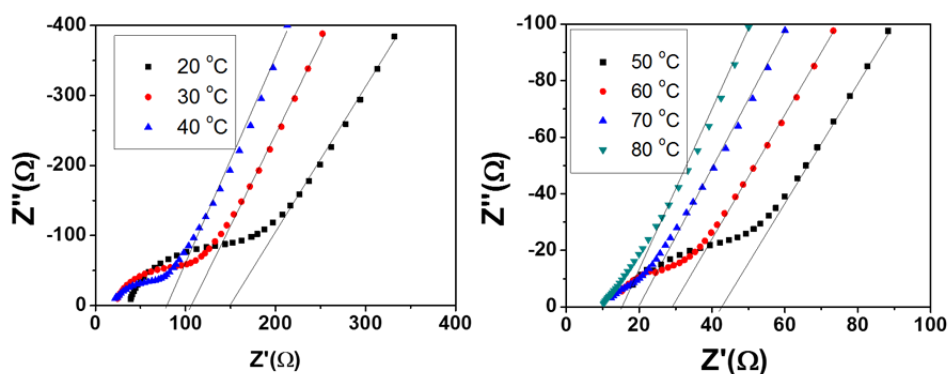


Figure 3. 5 Electrochemical impedance of PUU cushion polymer gel polymer electrolyte at different temperature (500 μm in thickness and 1.2 cm^2 in area).

Figure 3-6 shows wide electrochemical stability window of PUU cushion polymer GPE. When the voltage reaches below 0 V (versus Li⁺/Li) to -0.2 V, lithium begins to deposit on stainless steel working electrode; when the voltage increases to above 0 V, the deposited lithium depletes from working electrode. Thus the PUU cushion polymer GPE is stable with lithium metal. Moreover, the PUU cushion polymer GPE is also stable at 4.5 V, which is similar to that of liquid electrolyte.

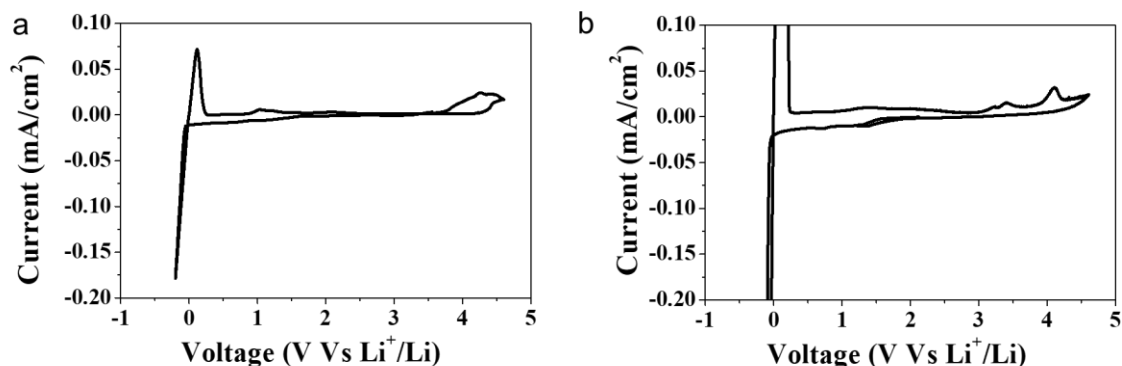


Figure 3. 6 Cyclic voltammetry of PUU cushion polymer GPE (a) and liquid electrolyte (1M LiPF₆/EC-DEC) (b) with stainless steel working electrode and lithium metal counter electrode at a scan rate of 0.5 mV s⁻¹ between -0.2 V and 4.6 V.

The designed PUU cushion polymer GPE shows moderate ionic conductivity for lithium ion transport in electrochemical cell, good electrochemical stability at low electrochemical potential around 0 V vs Li⁺/Li, as well as good elasticity and stretchability to accommodate large volume change of SiO particles and electrode.

3.3 Characterization of SiO electrode with PUU polymer cushion

Here we use SiO as active material, because SiO delivers a reversible capacity of 1000-1300 mAh g⁻¹, which shows much smaller volume change of 100% than that of Si (300%). Upon lithiation/delithiation, SiO can form a homogeneous mixture of active Si phase and inactive silica (lithium silicate) phase, in which the inactive phase can buffer the volume change of active Si phase, restrict particle pulverization and help maintain electrode structure integrity. The SiO electrode is prepared by mixing micro-sized SiO particles, conductive carbon, and PAA (polyacrylic acid)-PVA (polyvinyl alcohol) binder to form a slurry and then coating it on Cu current collector. The PUU cushion polymer coating is made by pouring PUU solution in DMAc (5 wt%) on the top of

SiO electrode and evenly spreading it with the help of doctor blade (**Figure 3-7**). After slowly evaporating solvent, the PUU cushion polymer is uniformly distributed within the electrode. The amount polymer coating can be carefully tuned from 0.3-0.8 mg cm⁻² by optimizing the concentration of polymer solution and the gap of doctor blade. For SiO electrode with 2 mAh cm⁻² and 3 mAh cm⁻², 5 wt% PUU solution is coated on the top with a blade gap of 100 μm; the PUU mass loading is 0.3-0.4 mg cm⁻². For SiO electrode with 4 mAh cm⁻², 5 wt% PUU solution is coated on the top with a blade gap of 200 μm; the PUU mass loading is 0.6-0.7 mg cm⁻².

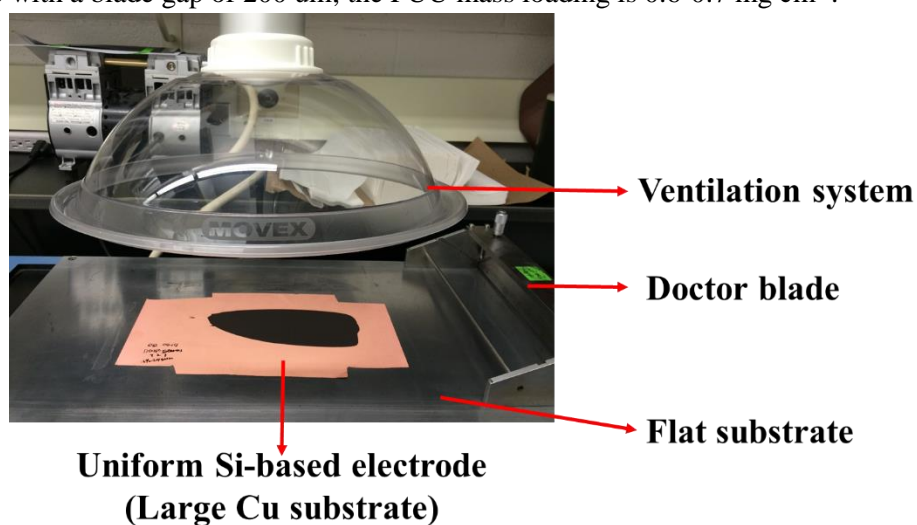


Figure 3. 7 Schema of coating PUU solution on SiO electrode.

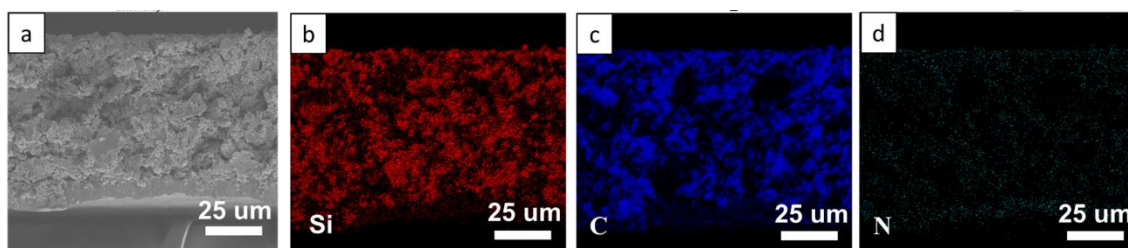


Figure 3. 8 Cross section SEM image (a) and EDS mapping of pristine SiO electrode with PUU coating for corresponding elements of (b) Si, (c) C, and (d) N.

The PUU cushion polymer is evenly distributed within the whole SiO electrode. The PUU cushion polymer coating exhibits not only on the top surface of electrode, but also goes inside electrode to function as intro-electrode cushion. As shown in **Figure 3-8**, the EDS mapping of

pristine SiO electrode with PUU cushion polymer shows even distribution of Si, C, and N element. N is characteristic element of polymer while the SiO electrode has no N element, thus the even distribution of N indicates uniform distribution of PUU cushion polymer within the whole electrode.

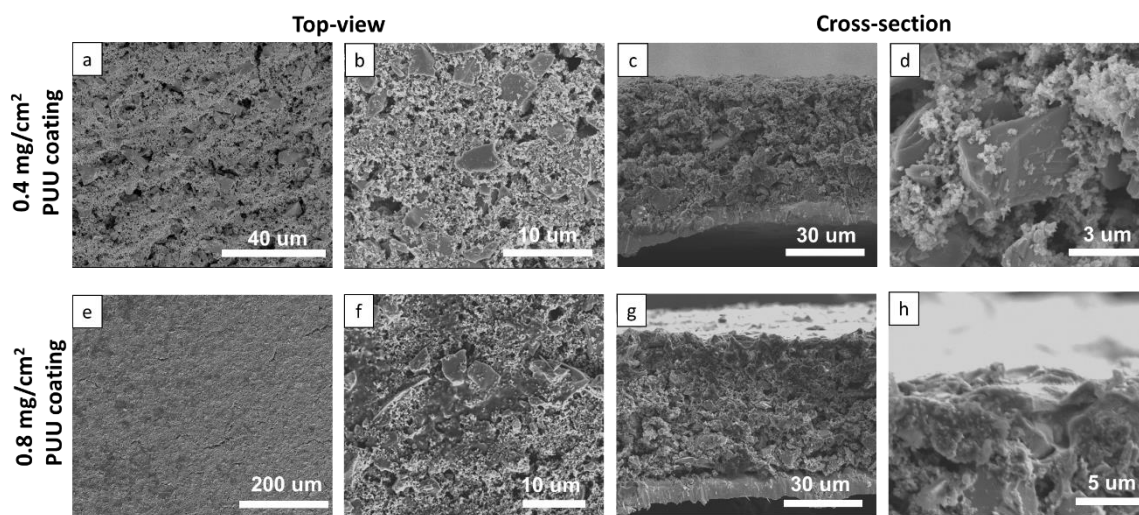


Figure 3. 9 SEM characterization of pristine SiO electrode with different amount of PUU coating: (a-d) 0.4 mg cm⁻²; (e-h) 0.8 mg cm⁻². (a), (b), (e) and (f) are the top-view images; (c), (d), (g), and (h) are cross-section images.

In **Figure 3-9**, it shows the SEM images of pristine SiO electrode with different amount of PUU cushion polymer. In Figure 3-9a and 3-9b, when the PUU coating amount is 0.4 mg cm⁻², the electrode morphology is similar to that of bare SiO electrode and the void space between conductive carbons is clear, while the SiO particle surface has a thin layer of polymer coating. In Figure 3-9e and 3-9f, when the amount of PUU cushion polymer is 0.8 mg cm⁻², the electrode top surface becomes very smooth, the void space between conductive carbons is blurred, and the SiO particle surface has a thick layer of polymer coating, which can be seen from cross-section SEM images in Figure 3-9g and 3-9h.

In **Figure 3-10**, it shows the AFM height images of pristine bare SiO electrode and SiO electrode with PUU polymer cushion. For pristine bare SiO electrode, the electrode surface is rough, which exist lots of peaks and valley. As a comparison, the PUU polymer cushion can partially fills

into valley and covers the electrode surface uniformly, thus the electrode surface with PUU polymer cushion becomes smooth.

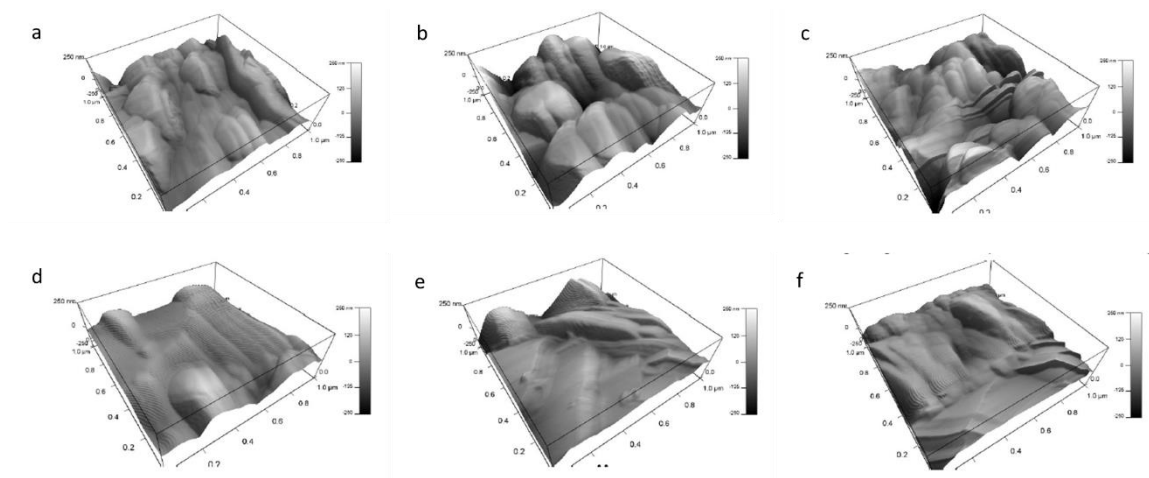


Figure 3.10 The atomic force microscope (AFM) height images pristine bare SiO electrode (a-c) and pristine SiO electrode with PUU cushion polymer (d-f).

The XPS results in **Figure 3-11** further confirm the uniform coating of PUU polymer cushion on SiO electrode. In Figure 2-11b, the sample of PUU polymer shows a characteristic peak of N (2s) at peak of 399.6 eV, as shown from the polymer structure in Figure 2-4a. In Figure 2-11e, the pristine bare SiO electrode shows no N (2s) peak, but two typical Si (2p) peaks at 100.3 eV (Si) and 104.2 eV (SiO_x); while in Figure 2-11b, the pristine SiO electrode with PUU polymer cushion shows a typical N (2s) peak from PUU, but no Si (2p) peaks. Besides, the C (2s) peak for pristine SiO electrode with PUU polymer cushion in Figure 2-9g shows typical C-C bonds at the peak of 284.6 eV and the C-O bonds at peak of 286.0 eV, which is similar to that of PUU polymer in Figure 2-11a. In comparison, the C (2s) peak for pristine SiO electrode without PUU coating in Figure 2-11d shows not only the existence of C-C (284.6 eV) and C-O (286.0 eV) bonds, but also the ester group (-COO-) at the peak of 288.2 eV and 288.8 eV, which are coming from polymer binder. For SiO electrode with PUU coating, the existence of characteristic N 1s peak and disappearance of Si

2p peaks further confirms that the top surface of SiO electrode is uniformly coated with PUU, especially the SiO particle surface is covered with PUU polymer.

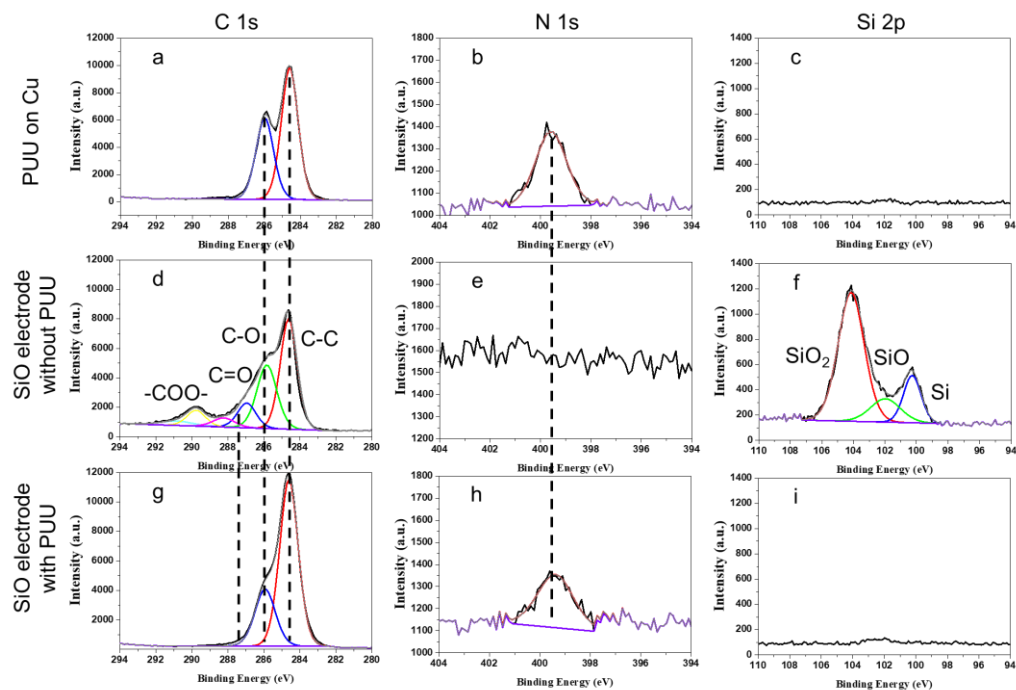


Figure 3. 11 X-ray photoelectron spectroscopy (XPS) analysis of SiO electrode without/with PUU polymer cushion. (a), (b), and (c) pure PUU; (d), (e), and (f) pristine SiO electrode without PUU polymer cushion; (g), (h), and (i) pristine SiO electrode with PUU polymer cushion.

To summarize, the cast coating of PUU polymer solution onto SiO electrode enables uniform coating of PUU both on the electrode surface, but also evenly distributes with the whole electrode. The SiO electrode with PUU polymer cushion shows a smooth surface from AFM and XPS results.

3.4 PUU polymer cushion can help maintain electrode structure integrity

The electrode structure integrity defines the pathways of lithium ions diffusion and electrons conduction. Either loss of lithium ion diffusion pathway or block of electrons conduction will lead to capacity fading of electrode. For high-areal-capacity Si-based anode, it exhibits large change in electrode thickness during charge/discharge process. The electrode cracking or delamination starts to happen when particles displacement is large and polymer binder cannot pull back active particles to their original position. The repeated electrode swelling and contraction will damage electrode structure integrity: Si particle pulverization is unavoidable; some pulverized particles may lose conductive network and some parts of electrode may get cracked or delaminate; the unavoidable particle pulverization and electrode cracking or delamination will generate new active surface to react with liquid electrolyte to form new SEI layer. The accumulative growth of SEI layer will trap lots of lithium ions and cause large irreversible capacity loss, resulting in fast capacity fading in full-cell with limited amount of Li⁺ ions.

The PUU polymer cushion can improve electrode structure stability upon discharge/charge process. Firstly, the PUU polymer cushion can alleviate the thickness expansion/contraction of SiO electrode upon cycling. **Figure 3-12a** shows in-situ electrode thickness change upon discharge/charge process. The PUU polymer cushion can accommodate large volume changes upon lithium insertion and extraction. In the first discharge cycle, there exists two regions for the corresponding electrode thickness change: in Stage 1, when SiO electrode undergoes lithiation, the electrode thickness shows no obvious change, because the initial porosity of SiO electrode allows SiO particles to expand within the whole electrode; in Stage 2, when SiO electrode undergoes further lithiation, the electrode thickness increased dramatically. In first charge cycle, the electrode thickness will not go back to the initial thickness, because the SiO shows low first cycle coulombic to due to the formation of SEI layer and inactive Li₂O and lithium silicate phase. The SiO electrode

without PUU coating shows a large electrode thickness change of 95% in the 1st discharge state (fully lithiated), whereas the electrode thickness change for SiO electrode with PUU coating decreased to 53%. For the 2nd and 3rd discharge, the relative thickness change for SiO electrode without PUU coating is still as large as 83% and 72%, while the PUU coating can decrease the electrode thickness change to 52% and 51%.

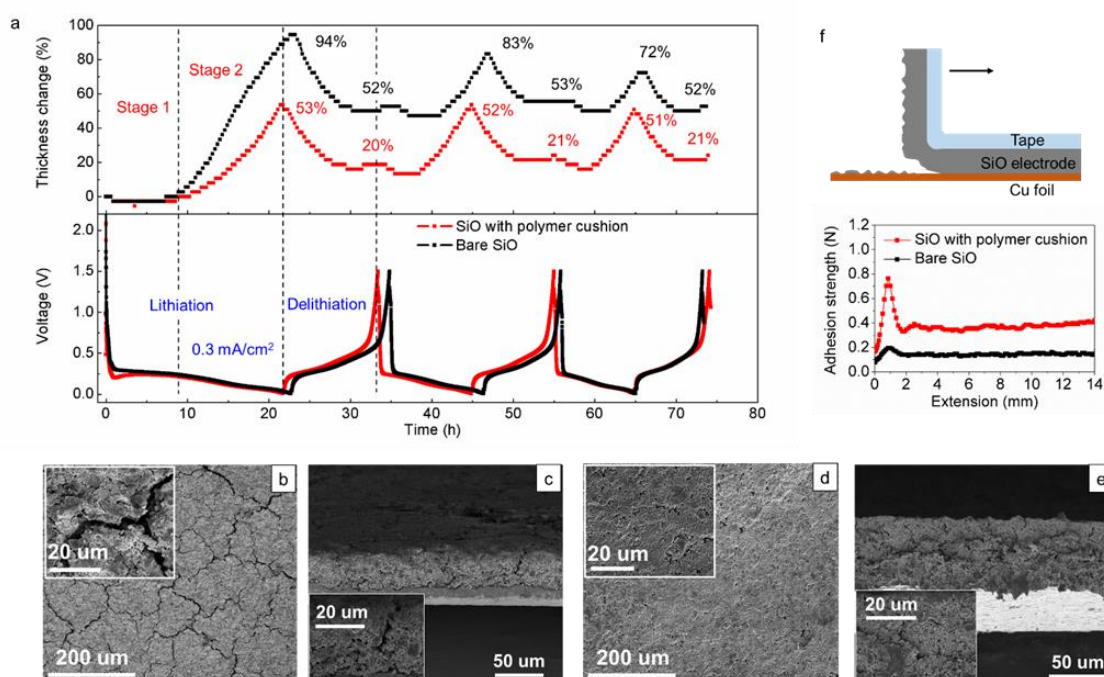


Figure 3. 12 Characterization of SiO electrodes with PUU polymer cushion. (a) In-situ measurement of thickness changes of a bare SiO electrode and a SiO electrode with PUU polymer cushion in the initial three lithiation/delithiation cycles at current density of 0.3 mA cm⁻² between 0.01 V and 1.5 V. (b,c) Top-view (b) and cross-sectional (c) SEM images of the bare SiO electrode after 10 cycles. (d and e) Top-view (d) and cross-sectional (e) SEM images of the SiO electrode with polymer cushion after 10 cycles. (f) Peel adhesion test of SiO electrodes with and without polymer cushion, which were peeled-off from Cu foil using a 90 degree dragging force.

The large change in electrode thickness arises plastic deformation of electrode and leads to lots of electrode cracking or delamination. As shown Figure 3-12b and 3-12c, the SiO electrode without PUU polymer cushion showed large cracks after 10 discharge/charge cycles; while the SiO electrode with PUU coating after 10 discharge/charge cycles showed much less and smaller cracks.

Figure 3-13 shows electrode morphology change after 1 cycle, 10 and 20 cycles. All SiO electrode with PUU polymer cushion showed less and smaller cracks than that of SiO electrode without PUU coating. The elastic PUU coating can serve as intra-electrode cushion to accommodate the volume change of electrode.

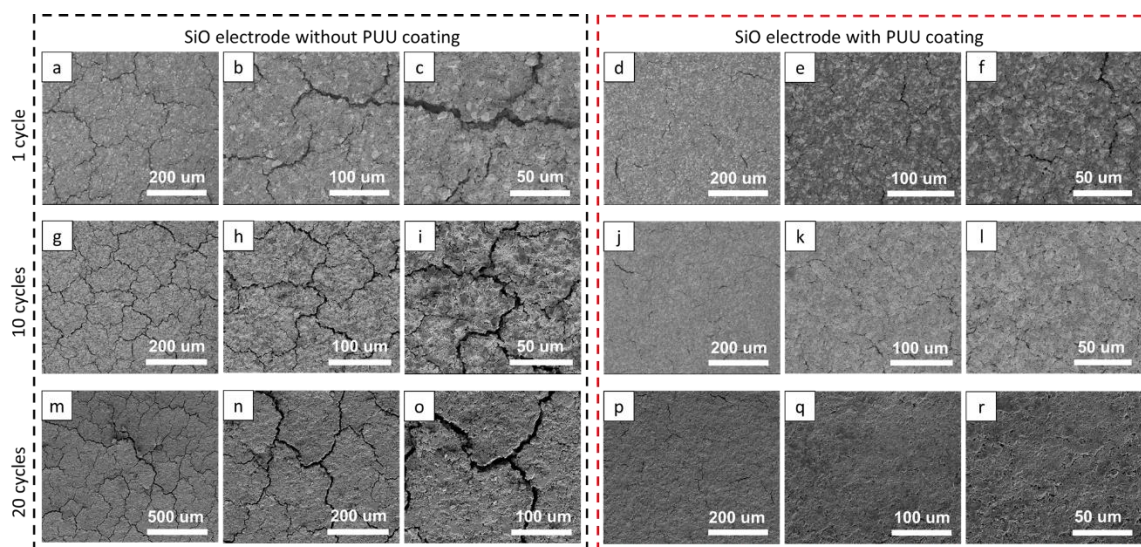


Figure 3. 13 Morphology characterization of SiO electrode after different cycles. (a-c) SEM images of SiO electrode without PUU polymer cushion after 1 discharge/charge cycle; (d-f) SEM images of SiO electrode with PUU polymer cushion after 1 discharge/charge cycle; (g-i) SEM images of SiO electrode without PUU polymer cushion after 10 discharge/charge cycles; (j-k) SEM images of SiO electrode with PUU polymer cushion after 10 discharge/charge cycles; (m-o) SEM images of SiO electrode without PUU polymer cushion after 10 discharge/charge cycles; (p-r) SEM images of SiO electrode with PUU polymer cushion after 10 discharge/charge cycles.

Figure 3-12f shows the result of 90 degree adhesive peel strength test, which measure adhesion strength between electrode and Cu current collector. The SiO electrode with PUU polymer cushion showed improved adhesion strength of 0.4 N, which is twice than that of bare SiO electrode. Besides, for SiO electrode with PUU polymer cushion, the maximum adhesion strength reached as large as 0.8 N, which indicates the strong interaction between PUU and Cu current collector. Thus

PUU polymer cushion coating can prevent electrode peel off or delaminate from current collector and help maintain electrons conduction between SiO electrode and Cu current collector.

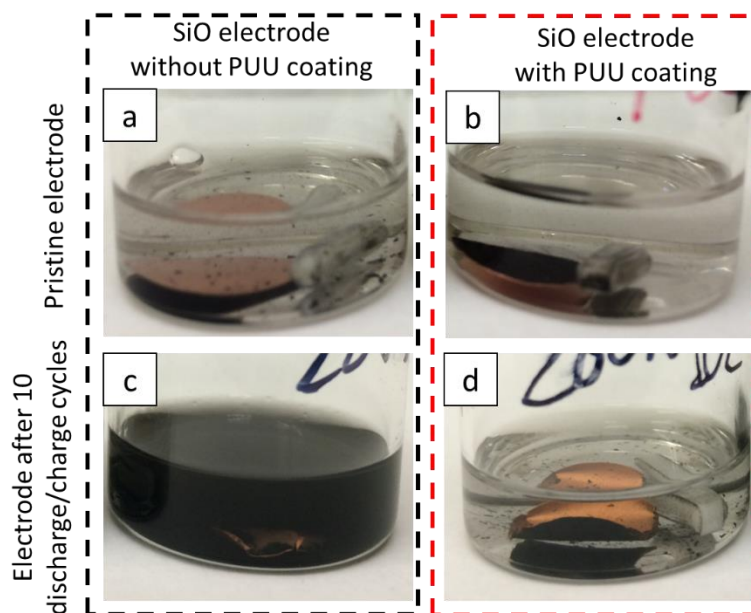


Figure 3. 14 Electrode stability test under magnetic stirring: SiO electrode without PUU coating (a) pristine electrode and (c) electrode after 10 discharge cycles; SiO electrode with PUU coating (b) pristine electrode and (d) electrode after 10 discharge cycles.

To get a direct view of electrode stability, the electrode was soaked in a liquid electrolyte and vigorous stirring was applied to delaminate electrode from current collector. As shown **Figure 3-14**, in control experiment, both the fresh electrodes with/without PUU polymer cushion were stable in liquid electrolyte under vigorous stirring, as the polymer binder can bind SiO particles and conductive carbon tightly. However, after 10 discharge-charge cycles, the SiO electrode without PUU polymer cushion was seriously damaged under vigorous stirring as the transparent liquid electrolyte turns into dark black. As a comparison, the SiO electrode with PUU polymer cushion was stable in liquid electrolyte under vigorous stirring. As mentioned before, the SiO electrode without PUU polymer cushion has lots of large cracks upon cycling and some parts delaminate from current collector. The delaminated electrode and pulverized particles will disperse in liquid electrolyte

under vigorous stirring. The PUU polymer cushion can only alleviate electrode cracking, but also improve the electrode adhesion strength on current collector. The PUU coating can restricted the pulverized SiO particles in a localized space and help maintain the electrode structure integrity.

The elastic and stretchable PUU polymer cushion can conformably accommodate volume change of SiO particle and electrode, and it also contributes to SEI layer and help stabilize SEI layer. In **Figure 3-15b** and 3-15e, after 10 discharge/charge cycles, the electrode with PUU polymer cushion shows a characteristic N (2s) peak at 399.8 eV, while the electrode without PUU coating show no N (2s) peak, which indicates that the PUU polymer cushion is still on the top surface of electrode. The PUU polymer cushion is elastic and stretchable to withstand the volume change of particle expansion/shrinkage and electrode expansion/contraction. Besides, the PUU polymer cushion also contributes to SEI layer and help stabilize SEI layer. For SiO electrode with PUU polymer cushion after 10 discharge/charge cycles, Figure 3-15a shows small C (2s) peaks at 287.7eV, 288.9 eV, and 290.1 eV, which are ascribed to alkyl carbonate from carbonate electrolyte decomposition products; it also shows large peaks at 284.6 eV and 286.0 eV, which are ascribed to C-C and C-O bonds from PUU polymer. As a comparison, for SiO electrode without PUU polymer cushion after 10 discharge/charge cycles, Figure 3-15d shows relatively larger C (2s) peaks at 287.7eV, 288.9 eV, and 290.1 eV, which are the major decomposition products of carbonate electrolyte from SEI layer; besides, the F (2s) in Figure 3-15f shows a large peak for LiF at 684.8 eV and a small peak for $\text{Li}_x\text{PO}_y\text{F}_z$ at 686.2 eV, which comes from the decomposition products of

FEC additive and LiPF_6 salts. The PUU polymer cushion contributes to SEI layer, and it also helps stabilize SEI layer.

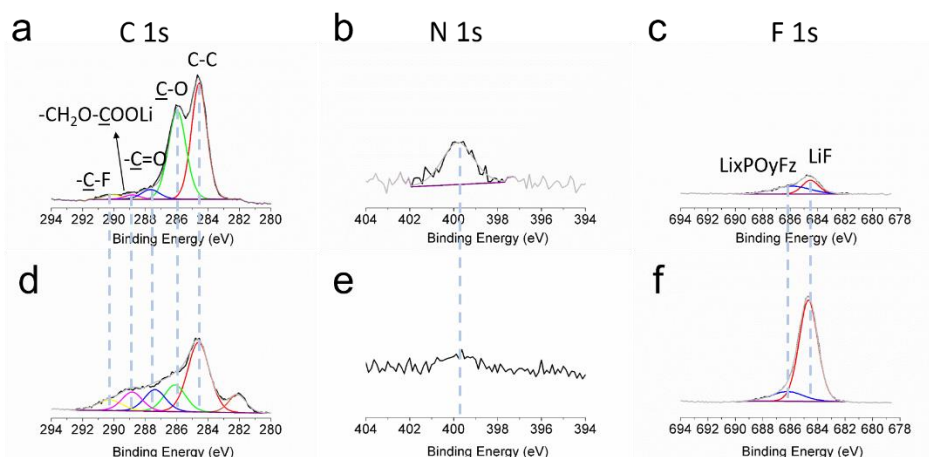


Figure 3.15 X-ray photoelectron spectroscopy (XPS) analysis of SiO electrode without/with PUU polymer cushion: (a-c) SiO electrode without PUU polymer cushion after 10 discharge/charge cycles; (d-f) SiO electrode with PUU polymer cushion after 10 discharge/charge cycles.

In **Figure 3-16a**, for the 1st cycle, both the SiO electrode with/without PUU polymer cushion showed similar impedance of 40 Ohm. The typical Nyquist plot consists of two semicircles and one 45° linear diffusion drift. It is generally accepted that the high-frequency semicircle arises from the formation of SEI layer, and the middle-frequency semicircle comes from the charge transfer reaction at the interface of electrolyte and SiO electrode. Due to activation process of SiO active material at 1st discharging process, both electrode shows very large SEI layer resistance and charge transfer resistance. However, after 10 cycles, the impedance of SiO electrode with PUU polymer cushion largely decreases from 43 Ohm to 19 Ohm, while the impedance of SiO electrode without PUU coating is still as large as 37 Ohm. More interestingly, for SiO electrode without PUU polymer cushion, the impedance gradually increases from 50 cycles (29 Ohm) to 100 cycles (35 Ohm); for SiO electrode with PUU polymer cushion, the impedance is stable from 50 cycles to 100

cycles (13 Ohm) and it is much smaller than that of SiO electrode without PUU polymer cushion at the same cycles.

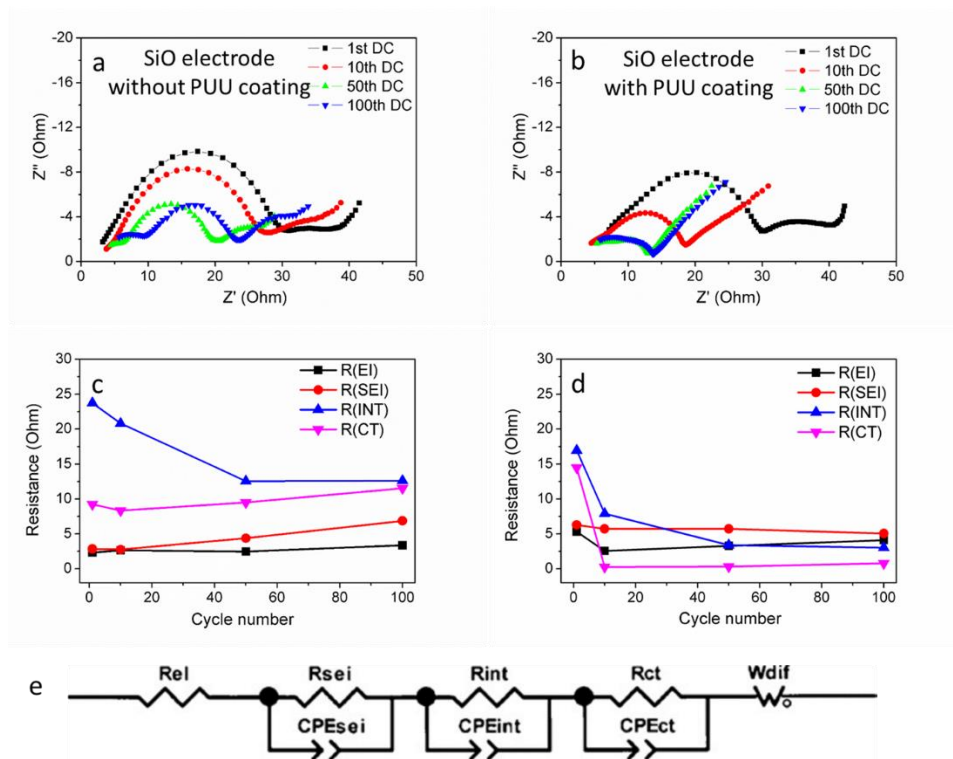


Figure 3. 16 Electrochemical impedance spectroscopy (EIS) of SiO electrode without (a) and with (b) PUU polymer cushion at 1 cycle, 10, 50, and 100 cycles; (c) and (d) are the detailed analysis of each impedance data following equivalent circuit (e).

Moreover, for SiO electrode without PUU polymer cushion after 50 cycles, the impedance showed three semicircles. The first high-frequency semicircle arises from the formation of SEI layer. The high-frequency semicircle could be interpreted as the resistance of the interphase electronic contacts between the current collector and the conductive additive/binder system. This equivalent circuit consists of a series of three resistors and constant phase elements (CPE) in parallel and a Warburg diffusion element to account for the SEI film resistance (first high-frequency semicircle), interphase electronic contact resistance (second high-frequency semicircle) and charge transfer resistance (mid-frequency semicircle). After fitting the impedance data, the SEI resistance (R_{SEI}), interphase electronic contact resistance (R_{INT}), and charge transfer resistance (R_{CT})

at different charge/discharge cycles were obtained in Figure 3-16c and 3-16d. For SiO electrode without PUU polymer cushion, the R_{CT} gradually increase from 10 cycles (8.4 Ohm), 50 cycles (9.5 Ohm), to 100 cycles (11.5 Ohm); for electrode with PUU polymer cushion, the R_{CT} shows little change from 10 cycles (0.3 Ohm), 50 cycles (0.3 Ohm), to 100 cycles (0.8 Ohm). As to R_{SEI} , for electrode without PUU coating, it also gradually increases from 10 cycles (2.7 Ohm), 50 cycles (4.4 Ohm), to 100 cycles (6.9 Ohm); for electrode with PUU polymer cushion, it is stable from 10 cycles (5.7 Ohm), 50 cycles (5.7 Ohm), to 100 cycles (5.1 Ohm). For electrode without PUU polymer cushion, the increasing impedance comes from the new SEI layer. For SiO electrode with PUU polymer cushion, the stable impedance from 50 cycles to 100 cycles indicates that the SEI layer is relatively stable during cycling and less new active surface is generated to prevent accumulated growth of SEI layer. Thus the PUU polymer cushion helps stabilize SEI layer, which can be further confirmed from half-cell and full-cell electrochemical performance below.

In summary, the PUU polymer cushion is uniformly coated within the whole electrode; it can accommodate volume change during discharge/charge process and help improve electrode structure integrity; it also contributes to SEI layer and help stabilize SEI layer.

3.5 Electrochemical performance of half-cell and full-cell

Figure 3-17a showed the half-cell electrochemical performance of SiO electrode with/without PUU polymer cushion. Both SiO electrode with/without PUU polymer cushion showed a first cycle Coulombic efficiency of 62 %, due to the formation of SEI and lithium silicate phase. The SiO electrode without PUU polymer cushion showed a stable areal capacity of 3 mAh cm^{-2} (or around 1200 mAh g^{-1} SiO) for 100 cycles, and then it started to drop quickly. After 100 cycles of repeated particle expansion/shrinkage and electrode expansion/contraction, the electrode structure integrity is seriously damaged: some pulverized particles and some parts of delaminated

electrode will lose conductive network and become electrochemically inactive. Interestingly, the SiO electrode with PUU polymer cushion was stable at of 3 mAh cm⁻² for 250 cycles. The elastic and stretchable PUU polymer cushion can accommodate large volume change, restrict the pulverized particles in a localized space to alleviate loss of conductive network, and help maintain the structure integrity.

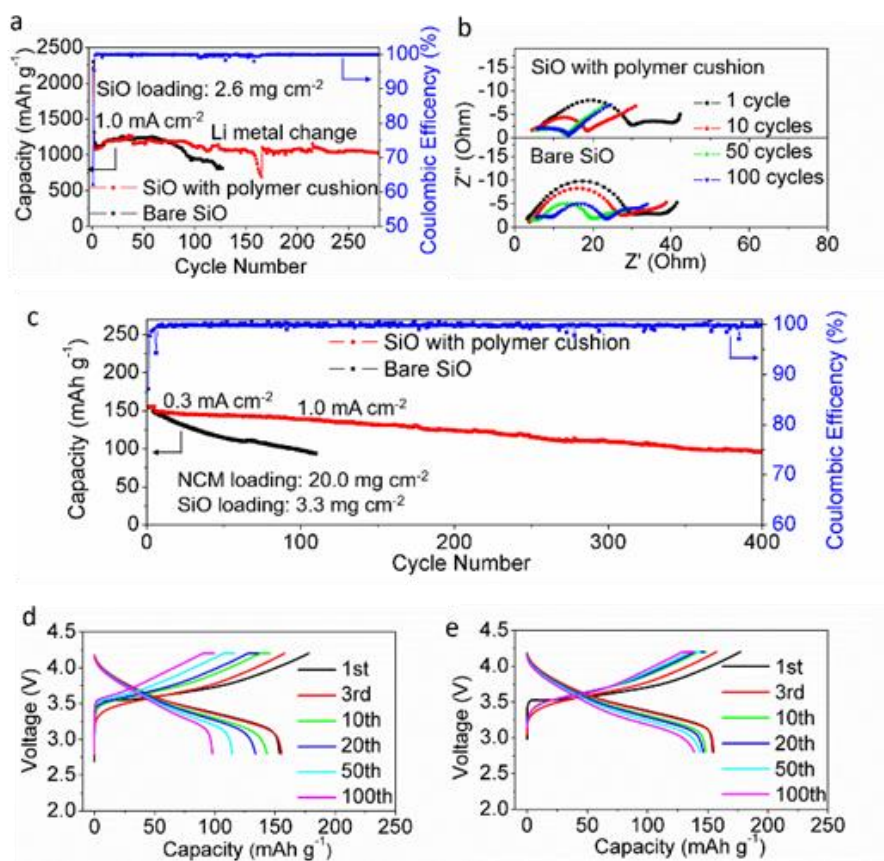


Figure 3. 17 Electrochemical performance of SiO anodes. (a) Half-cell discharge capacities of a bare SiO electrode and a SiO electrode with polymer cushion at 0.3 mA cm⁻² for the first cycle and 1.0 mA cm⁻² for rest cycles between 0.01 and 1.5 V, along with the Coulombic efficiency of SiO electrode with polymer cushion. (b) Electrochemical impedance spectroscopy (EIS) of a bare SiO electrode and a SiO electrode with polymer cushion after 1, 10, 50, and 100 cycles. (c) Full-cell discharge capacities of bare SiO|NCM 523 and SiO with polymer cushion|NCM 523 cells at 0.3 mA cm⁻² for the initial 3 cycles and 1.0 mA cm⁻² for rest cycles between 2.8 and 4.2 V, along with the Coulombic efficiency of SiO with polymer cushion|NCM 523 cell. (d and e) Corresponding voltage profiles of SiO|NCM 523 cells without (d) and with (e) polymer cushion. The SiO electrodes were precycled for full cell assembling.

In Figure 3-17b, the EIS spectra of SiO electrode without PUU polymer cushion showed gradually increasing impedance from 50 cycles to 100 cycles. The increasing impedance comes from the new SEI layer: the new active surface of pulverized particles and cracked electrode get in contact with liquid electrolyte and react with liquid electrolyte to form new SEI layer. Interestingly, for SiO electrode with PUU polymer cushion, the cell shows stable impedance from 50 cycles to 100 cycles and it is smaller than that of SiO electrode without PUU coating.

To confirm that PUU coating can help maintain electrode structure integrity and stabilize SEI layer, both SiO electrode with/without PUU polymer cushion were paired with NMC ($\text{LiNi}_{0.5}\text{Co}_{0.25}\text{Mn}_{0.25}\text{O}_2$) cathode in full-cell test. In half-cell test, the lithium metal anode provides excessive lithium ions; while in full-cell test, it has limited amount of lithium ions provided by the cathode. In each charge/discharge process, the SiO electrode will generate some new active surfaces to form new SEI and it will trap some lithium ions that cannot shuttle between cathode and anode. The irreversible capacity loss in each cycle determine full-cell capacity fading rate. In **Figure 3-18**, it showed the full-cell capacity retention as a function of full-cell Coulombic efficiency (CE): if the CE is 99.5%, the capacity retention drops below 80% after 46 cycles; if the CE is 99.7%, the capacity retention drops below 80% after 76 cycles; if the CE is 99.9%, the capacity retention drops below 80% after 225 cycles. The full-cell CE represents the irreversible Li^+ ions loss in each cycle.

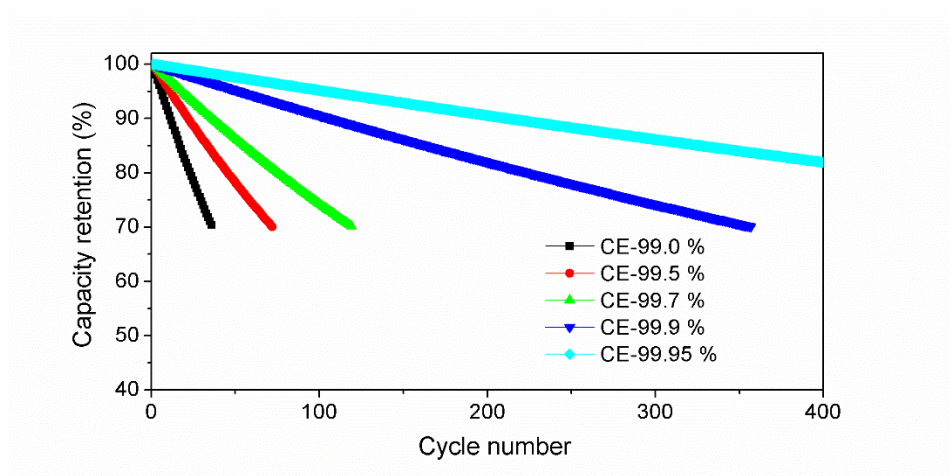


Figure 3. 18 The full-cell capacity retention as a function of Columbic efficiency (CE) and cycle number: 99.5% is full-cell of NCM/SiO electrode without PUU coating; 99.9% is full-cell of NCM/SiO electrode with PUU coating; 99.95% is full-cell of commercial NCM/Graphite cell.

As the SiO electrode showed very large first cycle irreversible capacity loss, SiO electrode was prelithiated before full-cell test. In Figure 3-17d and 3-17e, the SiO electrode was cycled for one discharge/charge cycle to compensate the first cycle irreversible capacity loss. In Figure 3-18c, the capacity retention for SiO electrode with PUU polymer cushion|NCM full-cell was 70% after 400 cycles, while the bare SiO electrode|NCM full-cell showed 70% of capacity retention after 80 cycles. The electrode with PUU polymer cushion shows smaller electrode thickness increase and less electrode cracking upon charge/discharge process, thus decreasing new particle/electrode surface for SEI formation. The irreversible capacity loss in each cycle is largely reduced with the help of PUU polymer cushion. The fast capacity fading of bare SiO electrode|NCM full-cell is due to the relative low average Columbic efficiency of 99.6%. On the other hand, the PUU polymer cushion can improve the full cell Columbic efficiency to 99.9%.

Figure 3-19 showed improved cycling stability of NCM/SiO full-cell with both pre-cycled NCM cathode and SiO anode. The NCM cathode was cycled for 5 charge/discharge cycles and it was on delithiated state with areal capacity of 2.2 mAh/cm². The SiO anode was cycled for 10

discharge/charge cycles to compensate the first cycle irreversible capacity loss and form a stable SEI layer; the SiO anode was on lithiated state with an areal capacity of 2.9 mAh/cm². The SiO anode was reserved with 30% excessive lithium ions to compensate the irreversible lithium ion in full-cell cycling. The pre-cycled SiO electrode without PUU polymer cushion|pre-cycled NCM full-cell showed a stable areal capacity of 2.1 mAh cm⁻² for 80 cycles. When the reserved excessive Li ions in the SiO anode was consumed, the capacity started to fade fast with 80% capacity retention after 150 cycles. On the other hand, the pre-cycled SiO electrode with PUU polymer cushion|pre-cycled NCM/ cell showed a stable areal capacity of 2.1 mAh/cm² for 170 cycles and then the capacity dropped slowly with 80% capacity retention after 500 cycles.

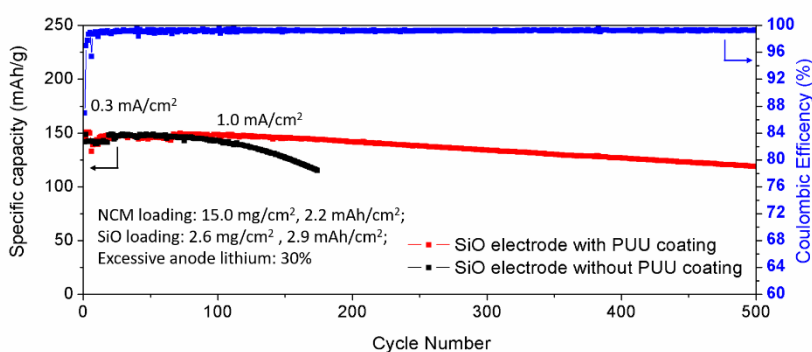


Figure 3. 19 Electrochemical performances of pre-cycled NCM cathode paired with pre-cycled SiO electrode with/without PUU polymer cushion: NCM cathode on discharged state (5 cycles, 2.2 mAh cm⁻²) and pre-cycled SiO anode on lithiated state (10 cycles, 2.9 mAh cm⁻²), with a current density of 0.3 mA cm⁻² for the 3 cycles and 1.0 mA cm⁻² for rest cycles, between 3.8-4.2 V.

For SiO electrode with the PUU polymer cushion, the improved half-cell cycling stability, stable electrochemical impedance, and as well as the improved full-cell capacity retention, indicate that that the PUU coating can help to maintain electrode structure integrity and stabilize SEI layer.

3.6 Discussion

We demonstrate a general polymer coating strategy on SiO electrode to improve electrode structure integrity and stabilize SEI layer. The polymer coating function as intra-electrode cushion to accommodate the volume change of Si active material during charge/discharge cycles. The practical pouch cell requires that cell deformation ratio should be less than 20% during charge/discharge cycles. For the first cycle discharging process, the SiO electrode with PUU polymer cushion undergoes smaller electrode thickness increase (53%) than that of SiO electrode without PUU polymer cushion (94%). Moreover, the coating strategy is simple and easy to scale up via the slurry coating technique, which has been widely used in lithium-ion battery electrode fabrication process. Also PUU polymer is of low cost and it has been produced millions of tones every year for clothing industry. This coating strategy is promising for further application of anode with large volume change in lithium-ion battery system. In order to make the coating strategy work well in lithium-ion battery, some key parameters need to be carefully considered.

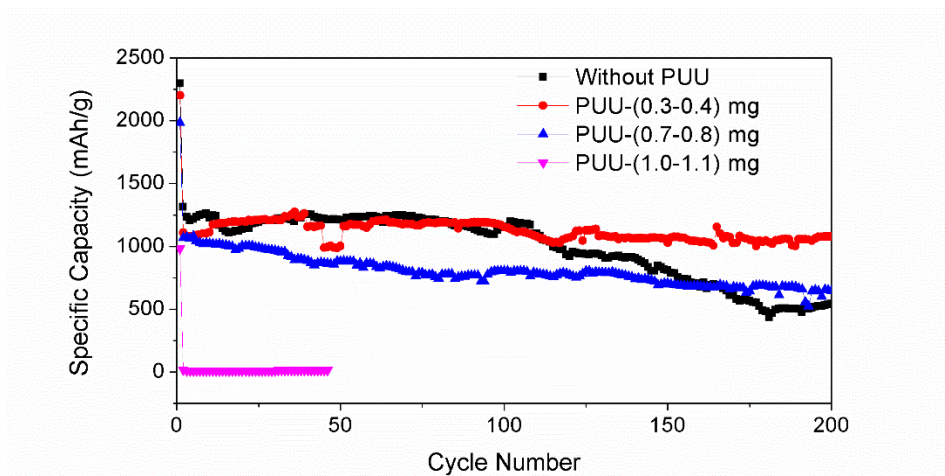


Figure 3. 20 Electrochemical performance of SiO electrode with different amount of PUU polymer cushion (the mass loading of SiO is 2.6 mg cm^{-2}) at a current density of 0.3 mA cm^{-2} for the first cycle and 1.0 mA cm^{-2} for rest cycles between 0.01-1.5 V.

The first parameter is how the amount of polymer cushion affect cycling stability. In **Figure 3-20**, when the amount of PUU polymer cushion was 0.3-0.4 mg cm⁻² (mass loading of SiO electrode was 3.6 mg cm⁻²), the SiO electrode showed a stable capacity at 3 mAh cm⁻² for 280 cycles; when the PUU polymer cushion amount increased to 0.7-0.8 mg cm⁻², the capacity was low and dropped fast; when he PUU polymer cushion amount increased to 1.0-1.1 mg cm⁻², the electrode showed little capacity after the first cycle. The result shows that the PUU polymer cushion amount should be optimized to accommodate the volume change of SiO particle. The excessive coating of PUU will decrease electrode porosity and prevent SiO particle from expansion, thus resulting in little capacity.

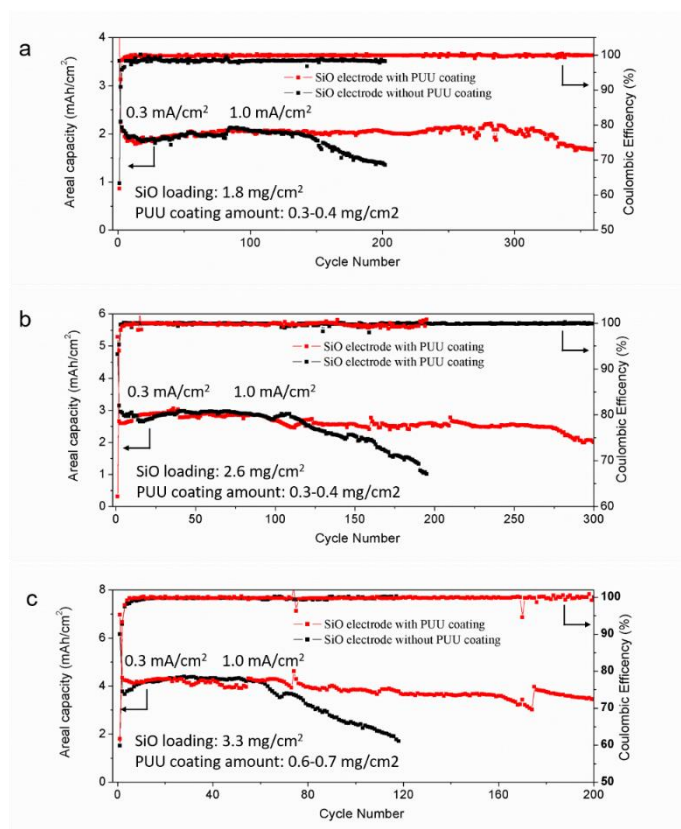


Figure 3. 21 Electrochemical performance of SiO electrode with/without PUU polymer cushion at different areal capacity: (a) 2 mAh cm⁻², the mass loading of SiO is 1.8 mg cm⁻², the PUU coating is 0.3-0.4 mg cm⁻²; (b) 3 mAh cm⁻², the mass loading of SiO is 2.6 mg cm⁻², the PUU coating is 0.3-0.4 mg cm⁻²; (c) 4 mAh cm⁻², the mass loading of SiO is 3.3 mg cm⁻², the PUU coating is 0.6-0.7 mg cm⁻².

For the electrode with different mass loading of SiO, the amount of PUU polymer cushion has been optimized as shown in **Figure 3-21**. In Figure 3-21a, the SiO electrode without PUU polymer cushion showed a stable areal capacity of 2 mAh/cm² (or specific capacity around 1200 mAh/g SiO) for 150 cycles. The PUU polymer cushion could stabilize the capacity to 330 cycles, when the PUU coating amount was 0.3-0.4 mg/cm². In Figure 3-21b and 3-21c, the structure integrity was damaged much faster with increasing mass loading and areal capacity. When SiO mass loading was 3.3 mg/cm² and the amount of PUU polymer cushion was 0.6-0.7 mg/cm², the SiO electrode showed a stable areal capacity of 4 mAh/cm² for 160 cycles, while the SiO electrode without PUU polymer cushion showed a stable capacity for only 60 cycles. With increasing mass loading of SiO, the optimized amount of PUU coating is also increased.

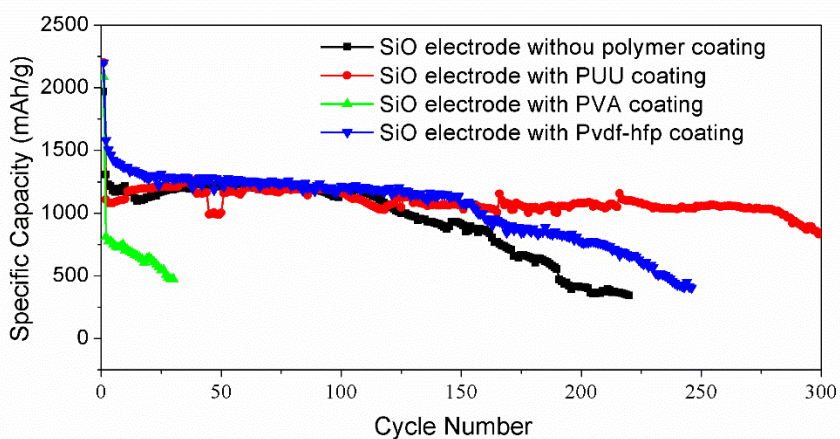


Figure 3. 22 Electrochemical performance of SiO electrode with different polymer coating and the polymer coating amount is fixed to 0.3-0.4 mg cm⁻² (the mass loading of SiO is 2.6 mg cm⁻², at a current density of 0.3 mA cm⁻² for the first cycle and 1.0 mA cm⁻² for rest cycles).

The second parameter is the uniqueness of PUU polymer cushion: it can swell in carbonate electrolyte to form a gel polymer electrolyte; it is elastic and stretchable due to the unique molecular structure with repeating soft and hard domains. In **Figure 3-22**, the PUU shows the best result

compared with other polymer coatings. The SiO electrode without polymer coating shows stable capacity of 1200 mAh g⁻¹ for 100 cycles and starts to drop quickly. The Pvdh-hfp coating showed some improvement that the electrode capacity was stable for 150 cycles. The commercial lithium-polymer battery utilize porous Pvdh-hfp as scaffold and it can absorb liquid electrolyte to form gel polymer electrolyte. Pvdh-hfp is a plastic with high young's modulus of 1.1 GPa and it can tolerate 200% elongation at break. The Pvdh-hfp gel polymer electrolyte can prevent liquid electrolyte leakage, inhibit lithium dendrite growth and thus improve battery safety. However, the Pvdh-hfp is not elastic and it cannot accommodate the volume change of SiO electrode upon cycling. As a result, the SiO electrode still shows capacity fading after 150 cycles. Moreover, the coating of PVA deteriorated the cycling stability with even low specific capacity of 700 mAh g⁻¹. Because, the PVA coating can form chemical bonds with PAA at high temperature during drying process. The electrode becomes rigid to prevent electrode from volume expansion. The elastic and stretchable PUU coating shows better results compared with Pvdh-hfp and PVA coating.

The third parameter is the selectivity of PUU coating on different active material of Si-based anode: whether or not PUU coating can improve the cycling stability of Si electrode and Si-graphite composite electrode. Here we choose Si microparticles electrode as an example: the Si microparticle is of low cost and it shows high first cycle Coulombic efficiency. The Si microparticles electrode is prepared following the same method using PAA-PVA as crosslinked polymer binder. The mass loading of Si is 2.0 mg cm⁻² with an areal capacity above 6 mAh cm⁻² upon lithiation process. Then Si microparticles electrode is paired with NCM cathode with a mass loading of 15.0 mg cm⁻², as shown in **Figure 3-23**. Thus Si is not fully lithiated during the first charge process and the volume change of Si particle is smaller. In Figure 3-23b, the first cycle showed a charge capacity of 2.88 mAh cm⁻² and discharge capacity of 2.51 mAh cm⁻², and the first cycle Coulombic efficiency was 86.9%. In Figure 3-23c, the Si microparticles electrode was coated with 0.3 mg cm⁻² PUU, the first cycle showed a charge capacity of 2.98 mAh cm⁻² and discharge

capacity of 2.50 mAh cm^{-2} , and the first cycle Coulombic efficiency was 84.0%. Both cells show high first cycle Coulombic efficiency. In Figure 3-24a, for bare Si microparticle electrode, the full-cell capacity dropped below 1.3 mAh cm^{-2} after 30 cycles with low Coulombic efficiency of 97.0%; for Si microparticle electrode with PUU polymer cushion, the full-cell capacity dropped below 1.8 mAh cm^{-2} after 60 cycles with improved Coulombic efficiency of 98.5%. The PUU coating can accommodate partially accommodate the volume change Si microparticle during charge/discharge cycles and improve the full-cell cycling stability. However, the volume change of Si microparticle is too large and the PUU polymer cushion cannot fully maintain electrode structure integrity; the SEI layer still crack and form new SEI layer, thus trapping certain amount of lithium ions and resulting low full-cell Coulombic efficiency of 98.5%. The PUU coating on Si-graphite electrode is still under investigation.

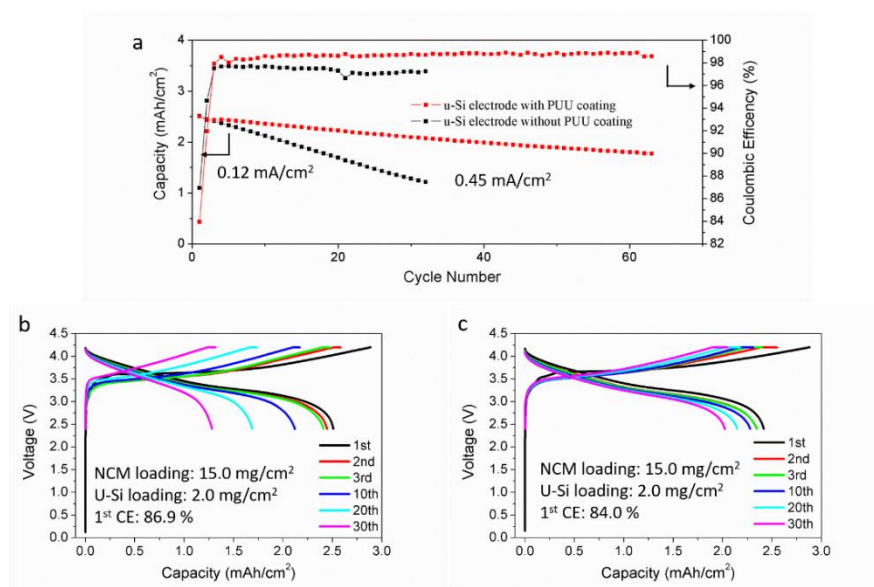


Figure 3. 23 Electrochemical performance of full-cell of Si microparticle electrode without/with PUU polymer cushion|NCM. (a) full-cell cycling performance at 0.12 mA cm^{-2} for the first cycle and 0.45 mA cm^{-2} for rest cycles under constant-current-constant-voltage mode between 2.4-4.2 V; Voltage profiles of (b) bare Si microparticles electrode|NCM full-cell and (c) Si microparticles electrode with PUU polymer cushion |NCM full-cell.

We demonstrated a copolymer, serving as an intra-electrode cushion to improve the integrity of SiO electrode with high mass loadings (above 2.5 mg cm⁻²). The polymer cushion contains a soft domain and a domain, therefore enabling good stretchability of the whole electrode and close contact with the SiO particles surface. The use of the polymer cushion can effectively alleviate electrode cracking, reduce the thickness increase of electrode, and prevent electrode peeling-off from current collector. Significantly improved battery performances were achieved under high-mass-loading and high-capacity conditions.

3.7 Methods

Preparation of cushion polymer membrane. Firstly, MDI (4,4'-methylene diphenyl diisocyanate, Sigma-Aldrich) (2.0 mmol) and PTMG (poly(tetramethylene ether) glycol, Mw = 2900, Sigma-Aldrich) (1.0 mmol) were added in an anhydrous dimethylacetamide (Sigma-Aldrich) solution (20 ml), and the mixture was heated at 80 °C for 4 h under inert argon gas to form isocyanate capped PTMG intermediate. After cooling to room temperature, EDA (ethylenediamine, Sigma-Aldrich) (1.0 mmol) was added to the solution under vigorous stirring, and the mixture was heated to 70 °C for 4 hours. The pure polymer can be obtained by pouring the solution on a Teflon mode and evaporating the solvent at 60 °C.

Preparation of SiO anode and NCM cathode electrodes. The SiO electrodes were prepared by mixing SiO powder (~10 μm, OTC), conductive carbon (Timical), and polyacrylic acid - polyvinyl alcohol (PAA-PVA) binder with a mass ratio of 7:2:1 to form a slurry. The solid content of the slurry was ~30 wt%. The slurry was cast on a copper foil using a doctor blade. The electrode was dried at 100 °C for 2 hours and 150 °C for 2 hours under vacuum. The mass loadings of SiO electrode for half and full cells were 2.6 mg cm⁻² and 3.3 mg cm⁻² (the corresponding discharge capacity is 3.0 mAh cm⁻² and 4.0 mAh cm⁻²), respectively. The SiO electrodes with polymer cushion were prepared by a solution cast coating method. A polymer solution (5 wt% in dimethylacetamide) was cast on a SiO electrode using a doctor blade, and then it can self-infuse into the entire electrode. The solvent was evaporated at room temperature overnight, and the electrode was further dried at 120 °C for 2 h under vacuum. The polymer coating amount was 0.3-0.7 mg cm⁻². For a SiO electrode with a mass loading of 2.6 and 3.3 mg cm⁻², the polymer coating amount was 0.3-0.4 and 0.6-0.7 mg cm⁻², respectively. NCM cathodes were prepared by mixing NCM 523 powder (Umicore), conductive carbon (Timical), and polyvinylidene fluoride (PVDF) (Sigma-Aldrich) at a mass ratio of 90:5:5 in N-methyl-2-pyrrolidone (Sigma-Aldrich) to form a

slurry. The solid content of slurry was ~45 wt%. After casting the solution on an aluminum foil, the electrode was dried at 100 °C under vacuum for 12 hours. The mass loading of NCM 523 active material was 20 mg cm⁻².

Electrochemical tests. Half-cell tests were performed in a CR 2016 type coin cell assembled with lithium metal (250 μm) as the counter electrode. The electrolyte was 1 M LiPF₆ in EC/DEC (v/v 1:1, BASF) with 10 wt% fluoroethylene carbonate (FEC, BASF) additive. Galvanostatic cycling test was carried out at 0.3 mA cm⁻² for first cycle and 1.0 mA cm⁻² for rest cycles between 0.01 V and 1.5 V on a BT2000 battery testing system (Arbin Instruments, USA). The specific capacity was calculated on the SiO active material. For full-cell tests, the SiO anode was lithiated and delithiated for one cycle with a current density of 0.3 mA cm⁻². The pre-cycled SiO electrodes (3.3 mg cm⁻² with a delithiation capacity of 4.0 mAh cm⁻²) were paired with NCM cathodes (20 mg cm⁻² with a delithiation capacity of 3.4 mAh cm⁻²) with an N/P ratio of 1.18. The full cell was cycled between 2.8 V and 4.2 V at small current density of 0.3 mA cm⁻² for 3 cycles and then cycled at 1.0 mA cm⁻² under a constant current-constant voltage mode. At the end of each charge cycle, the cell was hold at 4.2 V until the current density drops below 0.3 mA cm⁻². To conduct the swelling test, the polymer membrane was cut into a round disk (40 mg, 12 mm in diameter and 500 μm in thickness) and then immersed to a 1 M LiPF₆ in EC/DEC (v/v 1:1, BASF) electrolyte in an argon-filled glovebox. The membrane weights were measured after various time periods. To measure the ionic conductivity, the saturated membrane was assembled in a coin cell with two stainless steel spacers as working and counter electrode, respectively. The ionic conductivity was measured as a function of temperature using electrochemical impedance spectroscopy (0.1 Hz-105 Hz). For cyclic voltammetry test, the cushion polymer membrane was sandwiched between a stainless steel working electrode and a lithium metal counter electrode in a coin cell. The cell was cycled between -0.2 V and 4.6 V at a scan rate of 0.2 mV s⁻¹.

Characterizations. Fourier-transform infrared spectroscopy (FT-IR) was performed using a Bruker IFS 66/S FT-IR spectrometer and Spectra-Tech Collector II DRIFTS accessory. The 90-degree peel adhesion tests were conducted in [input]. The in-situ electrode thickness changes were tested using [input]. The electrochemical impedance and cyclic voltammetry were tested in Solartron 1260 equipment. X-ray photoelectron spectroscopy (XPS) was conducted with a Kratos Analytical Axis Ultra XPS using an air-sensitive holder. The surface morphologies and thickness of the SiO electrodes before and after cycling were investigated with a NanoSEM 630 scanning electron microscope. The electrode surface roughness was measured with atomic force microscopy (AFM) by the tip indentation technique.

Chapter 4

Development of stable high-capacity carbon-coated SiO_x/Graphite composite anode for lithium ion battery

Abstract

SiO has been considered as high-capacity anode material to improve the energy density of Li-ion batteries. However, it shows low first cycle Columbic efficiency (50-60%) due to formation of inactive phase (Li₂O and lithium silicate) and solid electrolyte interphase (SEI). Also, when paring with commercial cathode, the large volume change of SiO during lithiation/delithiation process causes large amounts of irreversible loss and leading to poor full-cell cycling stability. Here we demonstrate chemical vapor deposition growth of carbon layer on SiO_x (C-SiO_x). It can not only increase the electronic conductivity, but also decrease the amount of electrolyte decomposition, thus improving the first cycle CE to 74.1%. Moreover, when blending C-SiO_x with graphite anode, the composite anode shows high first cycle CE of 86.4%. The full-cell performance is still under investigation.

4.1. Introduction

With the growing market of electric vehicles, it requires development of high-energy Li-ion battery to achieve longer driving miles per charge. In order to increase the energy density to 300 Wh kg^{-1} , great efforts have been devoted to high-capacity cathode and anode material. However, when pairing graphite anode with high-nickel cathode (NCM-811 or NCA), the Li-ion battery energy density can only reach $250\text{-}260 \text{ Wh kg}^{-1}$. To further increase energy density, high-capacity anode is of significant importance to push it to $300\text{-}350 \text{ Wh kg}^{-1}$.^{13,15,66} Si is one type of alloying anode with high theoretical capacity of 4200 mAh g^{-1} , which ten times higher than that of graphite anode. It also shows low electrochemical potential of 0.4 V (Vs. Li^+/Li)^{24,66}. However, the volume change of Si during lithiation/delithiation is around 400% , which cause serious issues of particles pulverization, electrode cracking or delamination, and accumulated growth of SEI layer.

SiO is being considered as another type of promising anode for Li-ion battery. The SiO shows amorphous structure and the valance state is Si (Si^{2+}). The microstructure of SiO is still under study and it is proposed that there exist random distribution of nanodomain of $\text{Si}(\text{Si}^0)$ and $\text{Si}(\text{Si}^{4+})$ ⁷⁷⁻⁷⁹. The inactive SiO_2 phase can buffer volume change of Si phase during lithiation/delithiation, alleviate the stress, and inhibit Si active phase pulverization⁸⁰. Compared with Si, one advantage of SiO is its relative low specific capacity of $1000\text{-}1400 \text{ mAh/g}$, with corresponding smaller volume change of $50\text{-}70\%$ at particle level^{79,80}. However, the inactive phase of SiO_2 can also undergo irreversible lithiation to form inactive Li_2O and lithium silicate phase, which results in low first cycle Coulombic efficiency of $50\text{-}60\%$.⁷⁸

Here we develop a chemical vapor deposition (CVD) growth of carbon on SiO particles surface via thermal decomposition of acetylene at $900 \text{ }^\circ\text{C}$ to form C-SiOx. The carbon coating is composed of graphene layers, which can improve electronic conductivity of SiO particles. Also the dense carbon coating can accommodate the volume change SiOx during lithiation/delithiation and

decrease the amount of electrolyte decomposition, thus improving the first cycle Coulombic efficiency to 74.1%. Moreover, when blending C-SiOx with graphite, the composite anode shows high first cycle Coulombic efficiency of 86.4%. The full-cell performance is still under investigation.

4.2. Characterization of graphene wrinkles

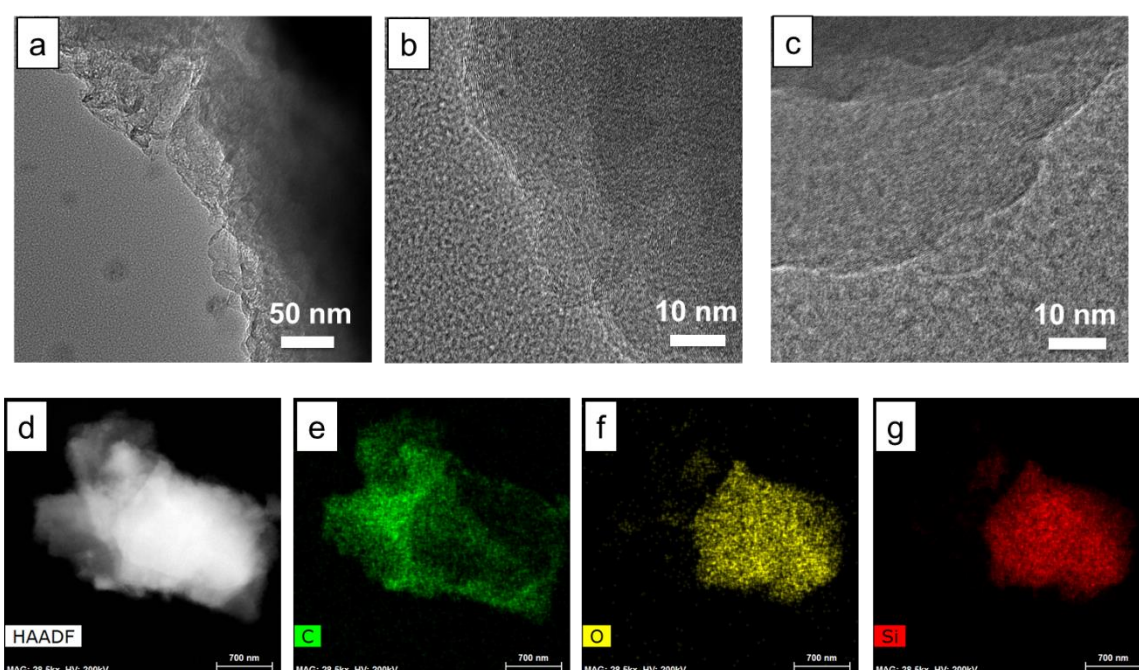


Figure 4. 1 Microscopic characterization of carbon coated SiOx (C-SiO). (a) (b) TEM and (c) high-resolution TEM images of graphene wrinkles. (d) STEM image and (e-g) EDS elemental mapping of C-SiOx.

The CVD growth of carbon coating was conducted via thermal decomposition of acetylene carbon resource at 900 °C. Before reaching 900 °C, the raw SiO undergoes disproportionation reaction to form Si and SiO₂.⁸¹ The outer SiO₂ shell can function as nucleation sites for CVD growth of carbon layers. After reaction at 900 °C for 2 hours, the raw brown SiO samples turned into dark black. Meanwhile, the weight of SiO increase by 8 wt%, indicating that the weight percentage of carbon in C-SiOx is 8 wt%.

Figure 4-1a and 4-2b showed the morphology of carbon coating on SiO_x. From the high resolution transmission electrons microscopy (HRTEM) observation in **Figure 4-1c**, the carbon coating showed layered structure. To probe the composition and spatial distribution of elements, we carried out energy-dispersive X-ray spectroscopy (EDS) under scanning transmission electron microscopy (STEM). **Figure 4-2e-g** shows elemental mapping of C, Si, and O in C-SiO_x, which indicates the uniform distribution of carbon on SiO_x to form core-shell structure and the carbon coating layer is hundreds of nanometer in thickness.

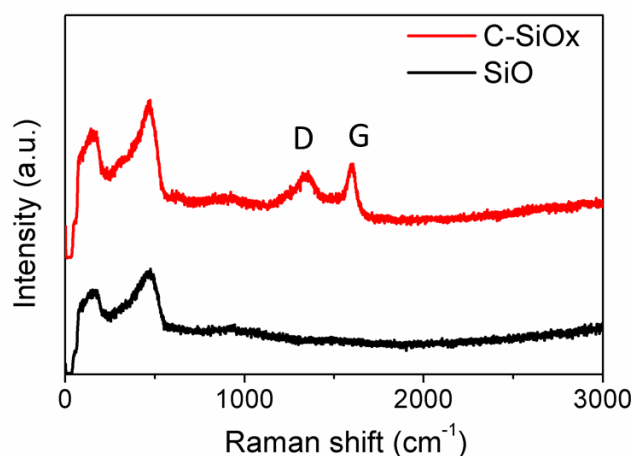


Figure 4. 2 Raman spectra of raw SiO and C-SiO_x.

To characterize the structure of graphene carbon coating layer, the Raman spectrum of C-SiO_x shows characteristic signals of graphene (D peak: $\sim 1350\text{ cm}^{-1}$ and G peak: $\sim 1580\text{ cm}^{-1}$) (**Figure 4-2**)⁸¹. The peaks at 520 and 950 cm^{-1} is from SiO. The D peak is related to the disordered

structure of graphene, which caused by the edges and defects of graphene wrinkles. G-band arises from the stretching of the C-C bond in graphitic materials.

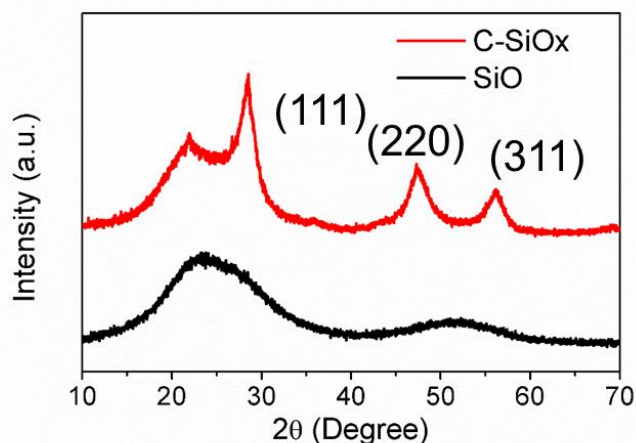


Figure 4. 3 X-ray diffraction of raw SiO and C-SiOx.

To prove the crystal structure of C-SiOx, we carried out X-ray diffraction (XRD) in **Figure 4-3**. From the XRD pattern, the C-SiOx shows three peaks, which are well indexed as Si (111), (220), and (311) diffraction peaks. Following Debye Scherrer equation, the domain size of crystalline Si is around 5 nm. The XRD result confirmed that SiO underwent disproportionation reaction to form Si nanocrystals within SiO₂ matrix.

4.3. Electrochemical performance of C-SiOx

The C-SiOx electrode was prepared by mixing C-SiOx, conductive carbons, and PAA-PVA polymer binder at a ratio of 7:2:1 to form a slurry and then coated it on Cu foil. The electrode got cross-linked at 150 °C for 2h. **Figure 4-4** showed the electrochemical performance of SiO electrode and C-SiOx electrode. In Figure 4-5a, the SiO electrode had a discharge capacity of 2114 mAh g⁻¹ and a charge capacity of 1314 mAh g⁻¹ for the first cycle, with a first cycle CE of 62.1%. The C-

SiOx electrode showed a discharge capacity of 1909 mAh g⁻¹ and a charge capacity of 1415 mAh g⁻¹, with a first cycle CE of 74.1%. The discharge voltage of C-SiOx was around 0.1 V, which comes from the lithiation potential of crystalline Si nanocrystals. The improved first cycle CE of C-SiOx electrode is possibly that the carbon coating layer can accommodate the volume change of SiOx particles during lithiation/delithiation and the decomposition of liquid electrolyte in SEI layer is less than that of SiO electrode. In Figure 4-4b, the C-SiOx shows stable capacity at 1200 mAh g⁻¹ for 100 cycles; while SiO electrode shows capacity sudden fading after 12 cycles and the capacity is stable at 1000 mAh/g for 100 cycles.

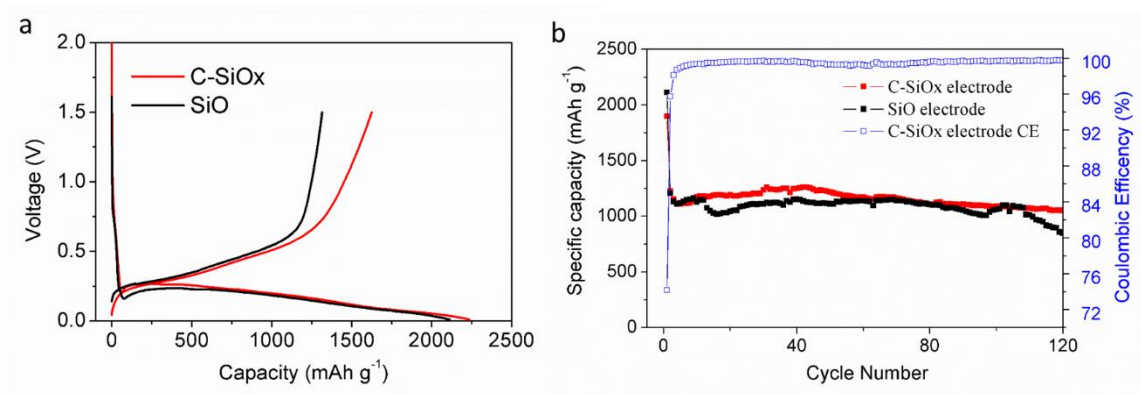


Figure 4.4 Electrochemical performance of C-SiOx electrode. (a) Voltage profile of SiO electrode and C-SiOx electrode for the first cycle. (b) Discharge capacity of SiO electrode and C-SiOx electrode with the corresponding CE. The mass loading electrode is 2.6 mg cm⁻².

Although the C-SiOx electrode shows improved first cycle CE of 74.1%, it is far below the CE of graphite anode (92.9%). When comparing C-SiOx anode with commercial cathode, the irreversible lithium ion loss in the first cycle is still very huge and it will significantly decrease the full-cell capacity. One effective method to further improve the first cycle CE is to add certain amount of C-SiOx to graphite anode to form composite anode. The composite anode shows high first CE of above 85%, which is prerequisite to pair with commercial cathode (it has a first cycle CE of 86-87%). Also, the capacity of composite anode is lower than that of C-SiOx anode, the electrode exhibits smaller volume change, and the cycling stability is better.

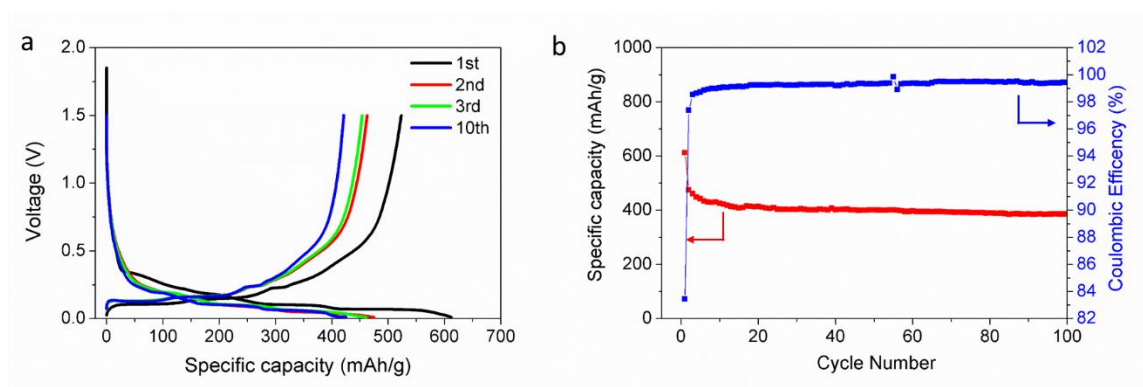


Figure 4. 5 Electrochemical performance of C-SiOx/graphite composite anode. (a) Voltage profile of SiO/graphite composite anode and C-SiOx/graphite composite anode for the first cycle. (b) Discharge capacity of SiO/graphite composite anode and C-SiOx/graphite composite anode with the corresponding CE. The mass loading electrode is 6.0 mg cm^{-2} .

To evaluate the cycling performance of C-SiOx/graphite composite anode, we prepared composite anode with specific capacity of $450\text{-}600 \text{ mAh g}^{-1}$. The slurring was composed of C-SiOx, graphite, conductive carbons, and NaCMC at a mass ratio of 10:80:5:5. **Figure 4-5** showed the electrochemical performance of composite anodes. In Figure 4-6a, the C-SiOx/graphite composite anode showed higher first cycle CE of 86.4%. However, in Figure 4-5b, while the capacity of SiO/graphite composite anode dropped fast to 400 mAh g^{-1} in 20 cycles.

In summary, we utilized the thermal decomposition of acetylene on SiO at high temperature to form carbon coating layer. The carbon coating was composed of dense graphene layers. Also, SiO underwent disproportionation reaction at $1000 \text{ }^{\circ}\text{C}$ to form Si nanocrystals embedded within SiO_2 matrix. The C-SiOx anode showed improved first cycle Coulombic efficiency of 74.1 %. When blending with graphite anode, the composite anode had a high first cycle Coulombic efficiency of 86.1 % and stable capacity at 450 mAh g^{-1} for 100 cycles. The full-cell pairing with composite anode is still under research.

Chapter 5

Seeded growth of lithium metal on LixSi-gel polymer electrolyte composite protection film

Abstract

Lithium metal anode is promising for further rechargeable lithium batteries, as it has high specific capacity and low electrochemical potential. However, one big challenge for lithium metal anode is lithium dendrite growth, which will cause serious safety issue and consume lots of liquid electrolyte. Here we design a composite LixSi/gel polymer electrolyte composite protection film on the top of lithium metal via simple cast coating approach. The LixSi functions as seeds for lithium nucleation and it has large surface area, thus it can reduce local current density and prevent lithium dendrite growth. When pairing with lithium iron phosphate cathode, the cell with composite protection films shows stable capacity at 2.0 mAh cm⁻² for 400 cycles.

5.1. Introduction

Lithium metal has been considered as the ‘holy grail’ of anode material for lithium-ion battery, due to its high specific capacity (3860 mAh/g) and its low electrochemical potential (-3.04 vs. standard hydrogen potential)^{9,82-86}. When replacing graphite anode with lithium metal anode for commercial Li-ion batteries, the cell energy density will increase to 300-400 Wh/kg⁸⁷. Meanwhile, for novel new electrochemical cells of Li-S and Li-O₂ battery, a reliable lithium metal anode is essential to achieve the potential high energy density^{3,60}. However, the practical application of lithium metal anode is encountering two major challenges: low Coulombic efficiency during each lithium deposition/depletion process and lithium dendrite growth (mossy lithium deposition)⁸⁶.

Lithium metal has very high chemical and electrochemical reactivity, thus it is thermodynamically unstable with organic solvent. Once it gets in touch with organic solvent, a passivation layer (SEI) will form immediately. However, the SEI layer is only tens of nanometer thick and it is too fragile to accommodate the huge volume change of lithium metal during lithium deposition/depletion process^{85,88}. The repeated SEI break and growth leads large amount of irreversible lithium ions loss in each cycle, resulting in low Coulombic efficiency and even consumption of liquid electrolyte for long-term cycling. Another challenge of lithium metal anode is lithium dendrite growth⁸⁹⁻⁹¹. The lithium dendrite growth is caused by microscopically local uneven current density, as a result of the defects, impurity and pin-hole of SEI layer on the surface of lithium metal. Once the dendrite nucleates, the lithium ions prefer to deposit on the protrusion area. The dendrite morphology of lithium deposit has a large surface area and thus large amounts of liquid electrolyte are accessible to react with lithium metal. Moreover, during lithium depletion, the bottom of dendrite dissociates much faster than other part, leading to the loss of electric contact and formation of ‘dead lithium’. The lithium dendrite may also pierce through the separator, short-circuit the battery, and cause serious safety issue.

To prevent lithium dendrite growth, one effective strategy is to apply polymer or polymer/ceramic composite protection film with high shear modulus to preventing lithium piercing through the protection film⁹²⁻⁹⁶. However, due to limited lithium ions diffusion in composite protection film, the rate performance of lithium metal anode is limited. Another strategy is to form an artificial SEI layer on lithium metal anode via electrolyte additives⁹⁷⁻⁹⁹, pretreatment with reactive chemicals¹⁰⁰⁻¹⁰², and new electrolyte design¹⁰³⁻¹⁰⁷. However, the generated composited protection has poor electrons or lithium ions conductivity and poor mechanical property, thus it cannot tolerate lithium metal anode with high areal capacity. Moreover, three dimensional current collector is also reported to reduce local current density and prevent lithium dendrite growth¹⁰⁸⁻¹¹². However, the 3D structure has large pore volume and large electrode thickness, which has to be filled lots of liquid electrolyte and sacrifice cell energy density.

Here we design a composite protection film on lithium metal anode via solution cast coating approach. It is composed Li_xSi embedding within polymer matrix of poly(poly(propylene oxide)-co-polyimide) (PPOPI), which can swell in carbonate electrolyte to form gel polymer electrolyte with good mechanical property. During drying process, the Si nanocrystals undergo lithiation to Li_xSi . The conductive Li_xSi can function as seeds for lithium nucleation and it has large surface area to reduce local current density. In electrochemical cell with LFP cathode, the lithium metal anode with composite protection film shows stable capacity of 2.0 mAh cm^{-2} for 400 cycles.

5.2. Preparation of PPOPI gel polymer electrolyte

The PPOPI polymer is prepared via two steps (**Figure 5-1**): firstly, 3,3',4,4'-biphenyltetracarboxylic dianhydride aromatic dianhydride (BPDA, $x+y$ mol) was added stepwise to mixture solution of 4,4'-oxydianiline (ODA, x mol) and poly(propylene oxide) diamine (PPO-diamine, y mol) in dimethylacetamide at 0 °C under inert Ar gas for 12 hours to form viscous polyamic acid solution; secondly, the polyamic acid solution was cast onto a glass Petri dish, kept at 80 °C overnight for evaporation of the solvent, and finally treated at 200 °C for 6 hours for complete imidization. The ratio between PPO-diamine and ODA is tuned from 1:1, 1:2, to 1:3. The corresponding PPOPI was named as PPOPI-11, PPOPI-12, and PPOPI-13.

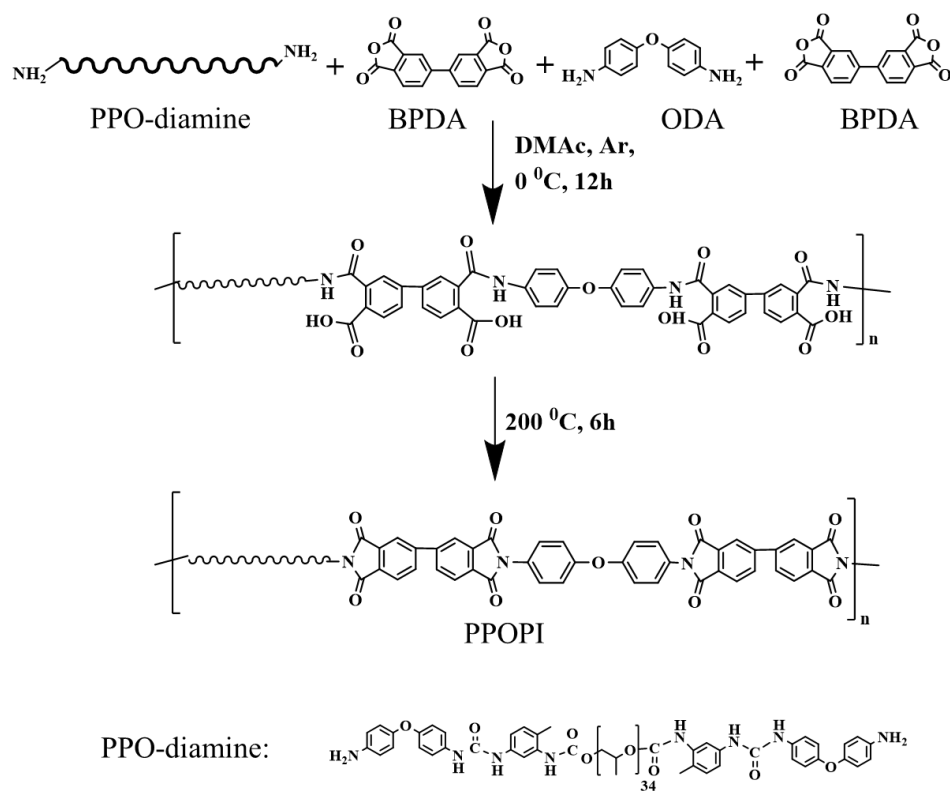


Figure 5. 1 Schema of synthesis of PPOPI polymer.

The PPOPI polymer is composed of repeated soft polypropylene oxide and rigid polyimide domains. The soft polyether chains can swell in carbonate electrolyte and provide

lithium ion conductivity. The rigid polyimide domains shows good chemical resistance and excellent mechanical properties. By tuning the ratio of soft to rigid domains, the PPOPI polymer shows adjustable electrolyte uptake amount as well as tunable mechanical properties. **Figure 5-2** showed swelling results of PPOPI membrane in carbonate electrolyte, including the change of membrane thickness, diameter, and weight. The sample of PPOPI-11 could swell and uptake 290 wt% of carbonate electrolyte with an increase of 50% in diameter and 30% in thickness. With increasing amount of PI content, the electrolyte uptake amount decreased to 119 wt% for sample of PPOPI-13, and the change of membrane thickness and diameter was also smaller, compared with sample of PPOPI-11 and PPOPI-12. Moreover, as the sample of PPOPI-11 swell so much liquid electrolyte that the obtained gel polymer electrolyte became very soft. While the sample of PPOPI-13 swell moderate amount of liquid electrolyte and the obtained gel polymer electrolyte still maintained its mechanical property.

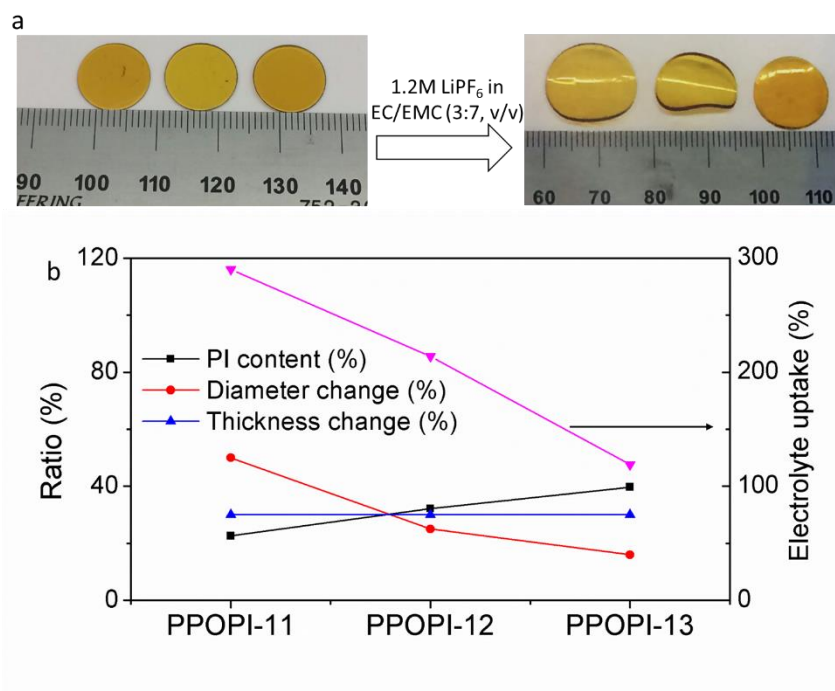


Figure 5. 2 Swelling experiments of PPOPI membrane in carbonate electrolyte (a) and the corresponding change in polyimide (PI) content, membrane thickness, membrane diameter, and electrolyte uptake amount.

To measure the ionic conductivity of corresponding gel polymer electrolyte membrane, the membrane was assembled between two stainless steel in a coin cell to measure its electrochemical impedance. As shown in **Figure 5-3**, the ionic conductivity of gel polymer electrolyte was measured at different temperature. The sample of PPOPI-11 gel polymer electrolyte showed the highest ionic conductivity of $3.7 \times 10^{-4} \text{ S cm}^{-1}$ at room temperature, as a result of large amount of electrolyte uptake. With increasing amount of PI content, the electrolyte uptake amount decreased to 119 wt% for sample of PPOPI-13 and the obtained gel polymer electrolyte had a smaller ionic conductivity of $3.7 \times 10^{-4} \text{ S cm}^{-1}$ at room temperature.

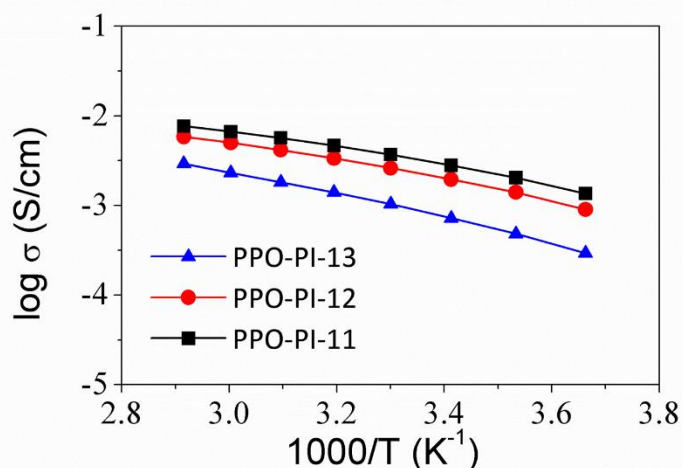


Figure 5. 3 Ionic conductivity of PPOPI gel polymer electrolyte at different temperature.

To above, the PPOPI membrane can swell and uptake tunable amount of liquid electrolyte by tuning the ratio of PPO and PI. With decreasing PI content, the membrane shows more amount of electrolyte uptake amount to form gel polymer electrolyte with higher ionic conductivity, but the mechanical property is also seriously damaged. The sample of PPOPI-13 shows moderate amount of electrolyte uptake to obtain gel polymer electrolyte with good ionic conductivity and mechanical property.

5.3. Preparation of Li_xSi /PPOPI composite protection film

The Li_xSi /PPOPI composite protection film was prepared via cast coating method. Firstly, the PPOPI-13 membrane was dissolved in anhydrous N-methyl-2-pyrrolidone and certain amounts of silicon nanocrystals was added to above solution. The weight ratio between PPOPI-13 and Si was 9:1, 8:2, and 7:3. The concentration was fixed to 2 wt% based on total weight of polymer and Si. The composite solution was further treated in an ultrasonic bath for 2 hours to disperse Si nanocrystals. Secondly, 100 mg solution was dropped on a lithium metal chip (16 mm in diameter) and the solvent was removed at room temperature under vacuum for 12 hours (**Figure 5-4**). During the drying process, the composite protection film was yellow brown at beginning 2 hours, which showed similar color to that of Si nanocrystals. Interestingly, after further drying for 12 hours, the composite protection film became dark black. In this process, the Si nanocrystals formed lithiated Si (Li_xSi) when they got in touch with lithium metal.

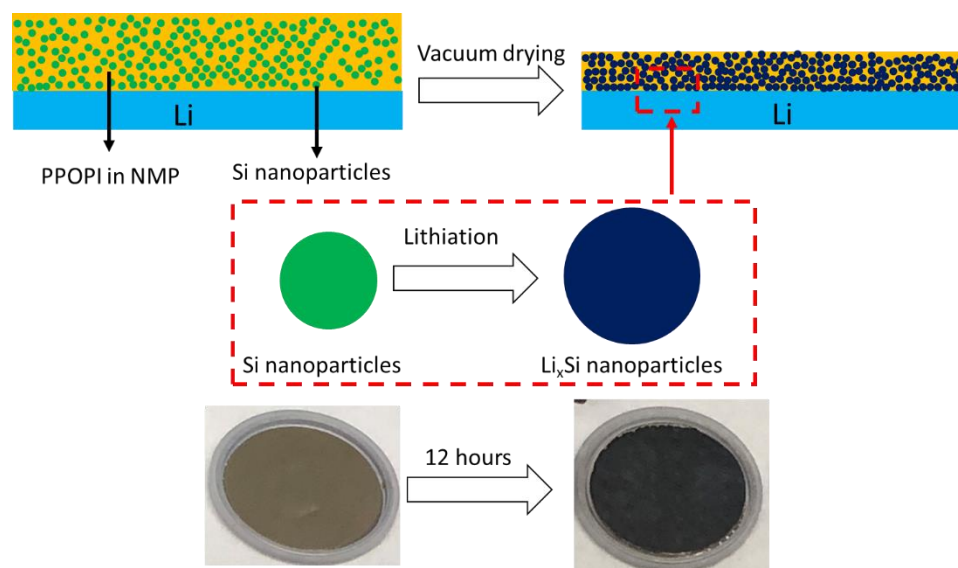


Figure 5. 4 Shema of coating composite protection film on lithium meal.

To further understand the color change of composite protection film, we use X-ray powder diffraction (XRD) to characterization the structure change of Si during drying process. In **Figure 5-5a**, three samples composite protection film were coated on stainless steel following the same coating and drying procedure. All the three samples shows two sets of characteristic peaks: one is for stainless steel substrate, the other is for crystalline Si peaks. In comparison, in figure 5-5b, the samples coated on lithium metal chips showed only one set of characteristic peaks for lithium metal while the characteristic peaks for Si nanocrystals disappeared, which indicated that the crystalline Si became amorphous Li_xSi .

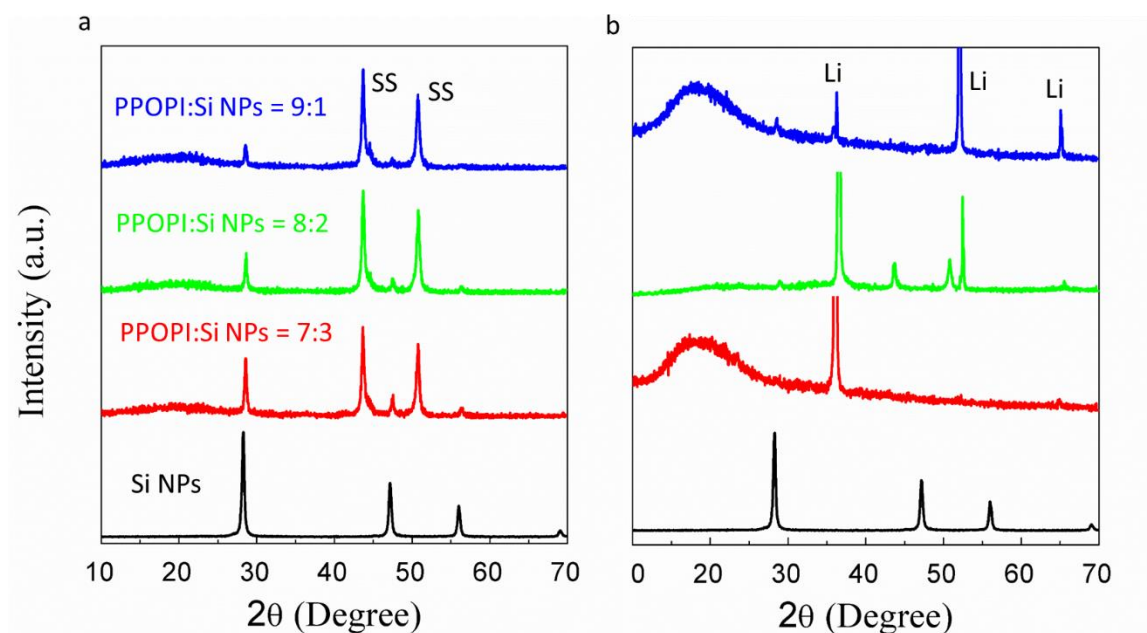


Figure 5. 5 XRD patterns of composite protection film coated on stainless steel (SS) and lithium metal chip.

In Figure 5-6, the morphology of composite protection film was characterized with SEM. The top-viewed SEM images showed that the composite protection film was composed of Si nanocrystals aggregates of about 1 μm in diameter which are uniformly embedded within polymer matrix. The cross-sectional SEM images showed that the composite protection film was around 5 μm in thickness.

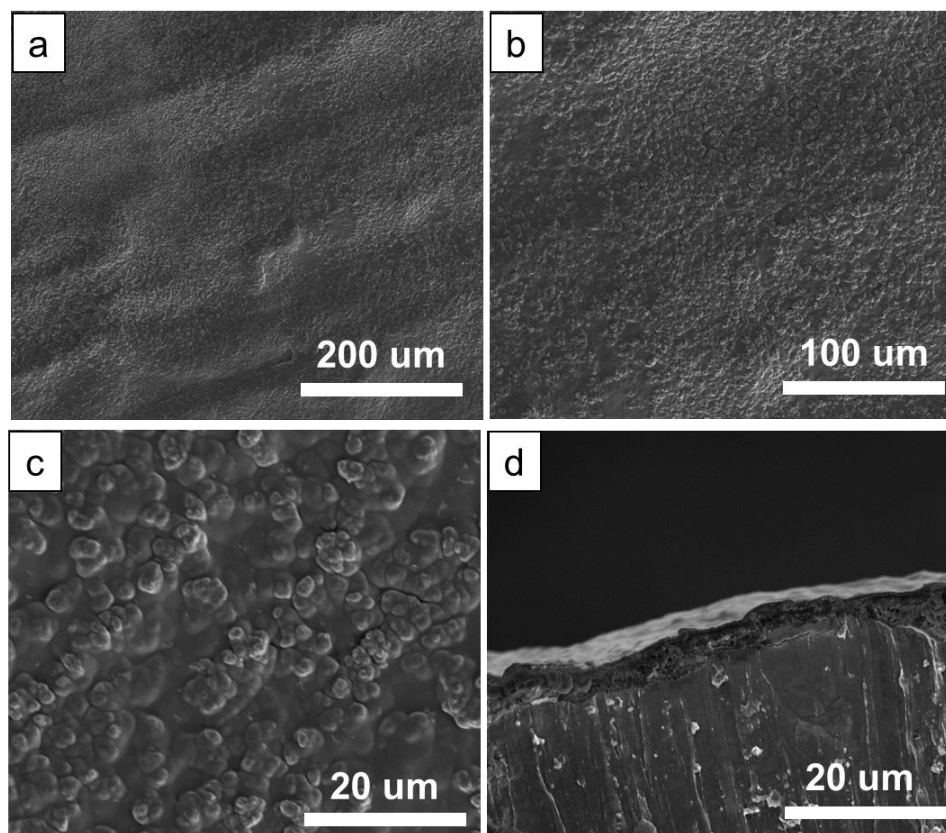


Figure 5. 6 Morphology characterization of composite of protection on lithium metal chip. (a-c) Top-viewed SEM images and (d) Cross-sectional SEM images.

5.4. Lithium deposition morphology

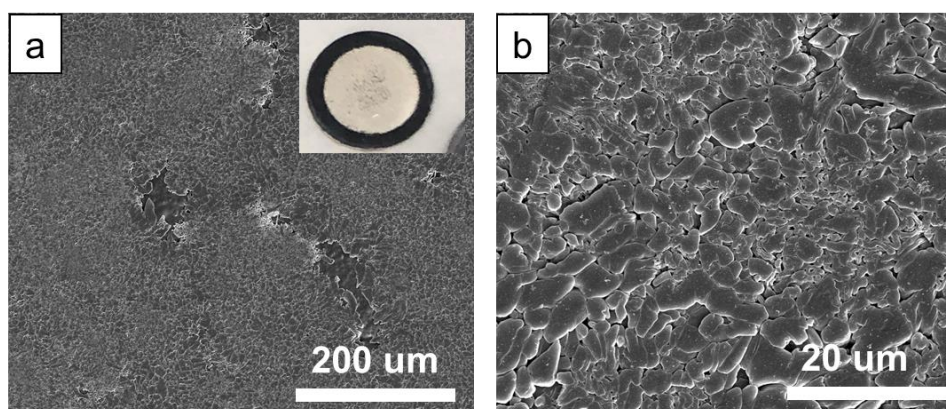


Figure 5. 7 Characterization of lithium deposition morphology in LFP cell after 10 cycles.

The Li_xSi was a good electronic conductor. The Li_xSi can function as seeds for lithium to nucleate due to the reduced nucleation energy and uniform distribution of conductive Li_xSi within composite protection film¹¹³. The Li_xSi has much large surface area than that of lithium metal chip, thus it can reduce local current density to prevent lithium dendrite growth. Figure 5-7 showed lithium deposition morphology after 10 charge/discharge cycles in a half cell with LFP cathode with an areal capacity of 2.0 mAh cm^{-2} . The shiny lithium metal deposited on the top of composited protection film instead of beneath it. The SEM images showed that the deposited lithium was composed of large granular lithium particles, which were closely packed with each other.

5.5. Electrochemical performance

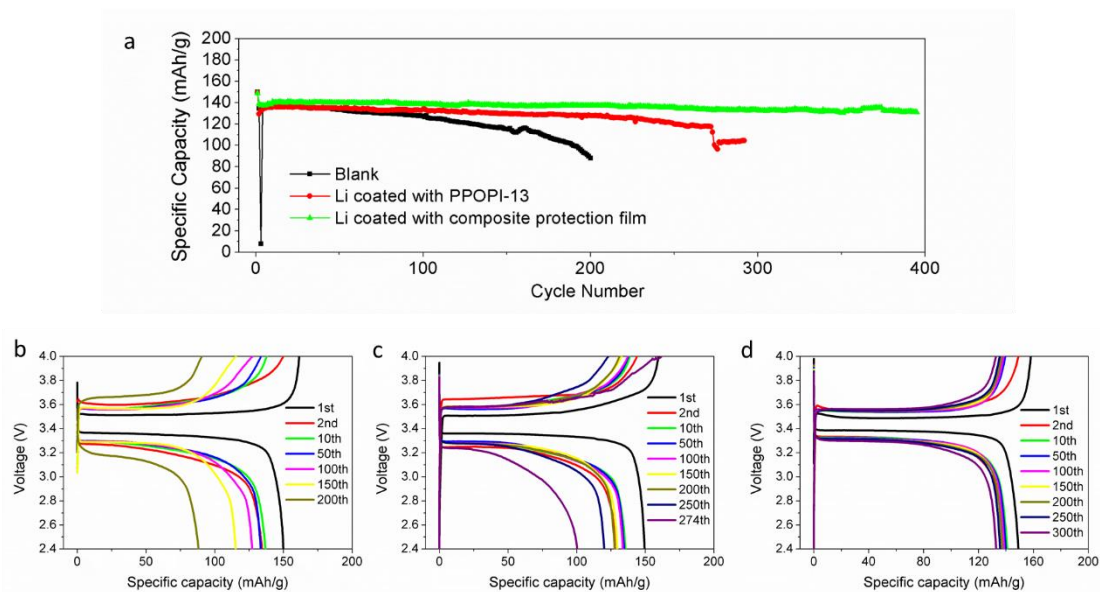


Figure 5. 8 Electrochemical performance of LFP cathode pairing different lithium metal anode (a) and the corresponding voltage profile of LFP cell with blank lithium (b), lithium coated with PPOPI-13 polymer, and lithium coated with composite protection film(c). The mass loading of LFP cathode is 15 mg cm^{-2} with an areal capacity of 2.0 mAh cm^{-2} .

The electrochemical performance of electrode with composite protection film was evaluated in a half-cell pairing with lithium iron phosphate (LFP) cathode with an areal capacity of

2.0 mAh cm⁻². In **Figure 5-8a**, for bare lithium metal, the LFP cell capacity was stable for 100 cycles and then it started to drop quickly; for lithium metal coated with pure PPOPI-13 polymer, the LFP cell capacity was stable for 250 cycles; for lithium metal with composite protection film, the LFP cell capacity was stable for 400 cycles. Meanwhile, in Figure 5-8b and Figure 5-8c, the LFP cells with bare lithium metal and lithium metal coated with pure polymer showed large polarization upon cycling, while the cell with composite protection film showed little polarization upon cycling.

5.6. Discussion

In conclusion, we reported a composite protection film with Si nanocrystals embedded within a robust PPOPI polymer matrix. The PPOPI could swell in carbonate electrolyte to form gel polymer electrolyte. During drying process, the Si nanocrystals underwent lithiation to form Li_xSi, which was electronic conductive and functioned as seeds for lithium nucleation and growth. It has large surface area to reduce local current density so as to inhibit lithium dendrite growth. The protected Li metal anode was stable in LFP cell with an areal capacity of 2.0 mAh cm⁻² for 400 cycles.

Reference

- (1) Xu, K.; About, M.; Article, T. Nonaqueous Liquid Electrolytes for Lithium-Based Rechargeable Batteries Nonaqueous Liquid Electrolytes for Lithium-Based Rechargeable Batteries. **2004**, *104*, 4303–4418.
- (2) Dunn, B.; Kamath, H.; Tarascon, J.-M. Electrical Energy Storage for the Grid: A Battery of Choices. *Science (80-.)*. **2011**, *334*, 928–935.
- (3) Bruce, P. G.; Freunberger, S. a.; Hardwick, L. J.; Tarascon, J.-M. Li–O₂ and Li–S Batteries with High Energy Storage. *Nat. Mater.* **2011**, *11*, 172–172.
- (4) Environ, E. Environmental Science Challenges in the Development of Advanced Li-Ion Batteries : A Review. **2011**, 3243–3262.
- (5) Nitta, N.; Wu, F.; Lee, J. T.; Yushin, G. Li-Ion Battery Materials : Present and Future. *Biochem. Pharmacol.* **2015**, *18*, 252–264.
- (6) Golubkov, A. W.; Fuchs, D.; Wagner, J.; Wiltsche, H.; Stangl, C.; Fauler, G.; Voitic, G. RSC Advances Batteries with Metal-Oxide and Olivin-Type Cathodes. **2014**, 3633–3642.
- (7) Environ, E. Environmental Science Prospective Materials and Applications for Li Secondary Batteries. **2011**, 1986–2002.
- (8) Kasavajjula, U.; Wang, C.; Appleby, a. J. Nano- and Bulk-Silicon-Based Insertion Anodes for Lithium-Ion Secondary Cells. *J. Power Sources* **2007**, *163*, 1003–1039.
- (9) Lin, D.; Liu, Y.; Cui, Y. Reviving the Lithium Metal Anode for High-Energy Batteries. *Nat. Publ. Gr.* **2017**, *12*, 194–206.
- (10) Kennedy, T.; Brandon, M.; Ryan, K. M. Advances in the Application of Silicon and Germanium Nanowires for High-Performance Lithium-Ion Batteries. *Adv. Mater.* **2016**, 5696–5704.
- (11) Zuo, X.; Zhu, J.; Müller-buschbaum, P.; Cheng, Y. Nano Energy Silicon Based Lithium-Ion Battery Anodes : A Chronicle Perspective Review. *Nano Energy* **2017**, *31*, 113–143.
- (12) Kim, S.; Sun, Y. Nickel-Rich Layered Cathode Materials for Automotive Lithium-Ion Batteries: Achievements and Perspectives. **2017**.
- (13) Etacheri, V.; Marom, R.; Elazari, R.; Salitra, G.; Aurbach, D. Challenges in the Development of Advanced Li-Ion Batteries: A Review. *Energy Environ. Sci.* **2011**, *4*, 3243–3262.
- (14) Nitta, N.; Yushin, G. High-Capacity Anode Materials for Lithium-Ion Batteries: Choice of Elements and Structures for Active Particles. *Part. Part. Syst. Charact.* **2014**, *31*, 317–336.
- (15) Luo, F.; Liu, B.; Zheng, J.; Chu, G.; Zhong, K.; Li, H.; Huang, X.; Chen, L. Review—Nano-Silicon/Carbon Composite Anode Materials Towards Practical Application for Next Generation Li-Ion Batteries. *J. Electrochem. Soc.* **2015**, *162*, A2509–A2528.
- (16) Chae, S.; Ko, M.; Kim, K.; Ahn, K.; Cho, J. Confronting Issues of the Practical Implementation of Si Anode in High-Energy Lithium-Ion Batteries. *Joule* **2017**, *1*, 47–60.
- (17) Zuo, X.; Zhu, J.; Müller-Buschbaum, P.; Cheng, Y. J. Silicon Based Lithium-Ion Battery Anodes: A Chronicle Perspective Review. *Nano Energy*, 2017, *31*, 113–143.
- (18) Luo, W.; Chen, X.; Xia, Y.; Chen, M.; Wang, L.; Wang, Q.; Li, W.; Yang, J. Surface and Interface Engineering of Silicon-Based Anode Materials for Lithium-Ion Batteries. *Advanced Energy Materials*, 2017, *7*, 1–28.
- (19) Feng, K.; Li, M.; Liu, W.; Kashkooli, A. G.; Xiao, X.; Cai, M. Silicon-Based Anodes for Lithium-Ion Batteries : From Fundamentals to Practical Applications. **2018**, 1702737.
- (20) Son, I. H.; Hwan Park, J.; Kwon, S.; Park, S.; Rummeli, M. H.; Bachmatiuk, A.; Song, H. J.; Ku, J.; Choi, J. W.; Choi, J.; *et al.* Silicon Carbide-Free Graphene Growth on Silicon for Lithium-Ion Battery with High Volumetric Energy Density. *Nat. Commun.* **2015**, *6*, 7393.
- (21) Wu, H.; Cui, Y. Designing Nanostructured Si Anodes for High Energy Lithium Ion Batteries. *Nano Today* **2012**, *7*, 414–429.
- (22) Chae, S.; Kim, N.; Ma, J.; Cho, J.; Ko, M. One-to-One Comparison of Graphite-Blended Negative Electrodes Using Silicon Nanolayer-Embedded Graphite versus Commercial Benchmarking Materials for High-Energy Lithium-Ion Batteries. *Adv. Energy Mater.* **2017**, *7*.
- (23) Lee, W. J.; Hwang, T. H.; Hwang, J. O.; Kim, H. W.; Lim, J.; Jeong, H. Y.; Shim, J.; Han, T. H.; Kim, J. Y.; Choi, J. W.; *et al.* N-Doped Graphitic Self-Encapsulation for High Performance Silicon

- Anodes in Lithium-Ion Batteries. *Energy Environ. Sci.* **2014**, *7*, 621–626.
- (24) Son, I. H.; Hwan Park, J.; Kwon, S.; Park, S.; Rummeli, M. H.; Bachmatiuk, A.; Song, H. J.; Ku, J.; Choi, J. W.; Choi, J.-M.; *et al.* Silicon Carbide-Free Graphene Growth on Silicon for Lithium-Ion Battery with High Volumetric Energy Density. *Nat. Commun.* **2015**, *6*, 7393.
- (25) Yoo, J. K.; Kim, J.; Choi, M. J.; Park, Y. U.; Hong, J.; Baek, K. M.; Kang, K.; Jung, Y. S. Extremely High Yield Conversion from Low-Cost Sand to High-Capacity Si Electrodes for Li-Ion Batteries. *Adv. Energy Mater.* **2014**, 1–9.
- (26) Kim, H.; Han, B.; Choo, J.; Cho, J. Three-Dimensional Porous Silicon Particles for Use in High-Performance Lithium Secondary Batteries. *Angew. Chemie - Int. Ed.* **2008**, *47*, 10151–10154.
- (27) Lin, N.; Han, Y.; Wang, L.; Zhou, J.; Zhou, J.; Zhu, Y.; Qian, Y. Preparation of Nanocrystalline Silicon from SiCl_4 at 200 °C in Molten Salt for High-Performance Anodes for Lithium Ion Batteries. *Angew. Chemie Int. Ed.* **2015**, *54*, 3822–3825.
- (28) Li, X.; Gu, M.; Hu, S.; Kennard, R.; Yan, P.; Chen, X.; Wang, C.; Sailor, M. J.; Zhang, J.-G.; Liu, J. Mesoporous Silicon Sponge as an Anti-Pulverization Structure for High-Performance Lithium-Ion Battery Anodes. *Nat. Commun.* **2014**, *5*, 1–7.
- (29) Wang, W.; Favors, Z.; Ionescu, R.; Ye, R.; Bay, H. H.; Ozkan, M.; Ozkan, C. S. Monodisperse Porous Silicon Spheres as Anode Materials for Lithium Ion Batteries. *Sci. Rep.* **2015**, *5*, 8781.
- (30) Ren, J.-G.; Wu, Q.-H.; Hong, G.; Zhang, W.-J.; Wu, H.; Amine, K.; Yang, J.; Lee, S.-T. Silicon-Graphene Composite Anodes for High-Energy Lithium Batteries. *Energy Technol.* **2013**, *1*, 77–84.
- (31) Chen, S.; Gordin, M. L.; Yi, R.; Howlett, G.; Sohn, H.; Wang, D. Silicon Core–hollow Carbon Shell Nanocomposites with Tunable Buffer Voids for High Capacity Anodes of Lithium-Ion Batteries. *Phys. Chem. Chem. Phys.* **2012**, *14*, 12741.
- (32) Li, Y.; Yan, K.; Lee, H.-W.; Lu, Z.; Liu, N.; Cui, Y. Growth of Conformal Graphene Cages on Micrometre-Sized Silicon Particles as Stable Battery Anodes. *Nat. Energy* **2016**, *1*, 15029.
- (33) Liu, N.; Lu, Z.; Zhao, J.; McDowell, M. T.; Lee, H.-W.; Zhao, W.; Cui, Y. A Pomegranate-Inspired Nanoscale Design for Large-Volume-Change Lithium Battery Anodes. *Nat. Nanotechnol.* **2014**, *9*, 187–192.
- (34) Jung, D. S.; Ryou, M.-H.; Sung, Y. J.; Park, S. Bin; Choi, J. W. Recycling Rice Husks for High-Capacity Lithium Battery Anodes. *Proc. Natl. Acad. Sci. U. S. A.* **2013**, *110*, 12229–12234.
- (35) Magasinski, a; Dixon, P.; Hertzberg, B.; Kvit, a; Ayala, J.; Yushin, G. High-Performance Lithium-Ion Anodes Using a Hierarchical Bottom-up Approach. *Nat. Mater.* **2010**, *9*, 353–358.
- (36) Yi, R.; Dai, F.; Gordin, M. L.; Sohn, H.; Wang, D. Influence of Silicon Nanoscale Building Blocks Size and Carbon Coating on the Performance of Micro-Sized Si-c Composite Li-Ion Anodes. *Adv. Energy Mater.* **2013**, *3*, 1507–1515.
- (37) Yi, R.; Dai, F.; Gordin, M. L.; Chen, S.; Wang, D. Micro-Sized Si-c Composite with Interconnected Nanoscale Building Blocks as High-Performance Anodes for Practical Application in Lithium-Ion Batteries. *Adv. Energy Mater.* **2013**, *3*, 295–300.
- (38) Zhang, R.; Du, Y.; Li, D.; Shen, D.; Yang, J.; Guo, Z.; Liu, H. K.; Elzatahry, A. a.; Zhao, D. Highly Reversible and Large Lithium Storage in Mesoporous Si/C Nanocomposite Anodes with Silicon Nanoparticles Embedded in a Carbon Framework. *Adv. Mater.* **2014**, *26*, 6749–6755.
- (39) Jin, Y.; Li, S.; Kushima, A.; Zheng, X.; Sun, Y.; Xie, J.; Sun, J.; Xue, W.; Zhou, G.; Wu, J.; *et al.* Self-Healing SEI Enables Full-Cell Cycling of a Silicon-Majority Anode with a Coulombic Efficiency Exceeding 99.9%. *Energy Environ. Sci.* **2017**, *10*, 580–592.
- (40) Yang, J.; Wang, Y.; Li, W.; Wang, L.; Fan, Y.; Jiang, W.; Luo, W.; Wang, Y.; Kong, B.; Selomulya, C.; *et al.* Amorphous TiO_2 Shells: A Vital Elastic Buffering Layer on Silicon Nanoparticles for High-Performance and Safe Lithium Storage. *Adv. Mater.* **2017**, *1700523*, 1–7.
- (41) Technol, J. E. S.; Choi, N.; Ha, S.; Lee, Y.; Jang, J. Y.; Jeong, M.; Shin, W. C.; Ue, M. Recent Progress on Polymeric Binders for Silicon Anodes in Lithium-Ion Batteries. *J. Electrochem. Sci. Technol.* **2015**, *6*, 35–49.
- (42) Mazouzi, D.; Karkar, Z.; Reale Hernandez, C.; Jimenez Manero, P.; Guyomard, D.; Roué, L.; Lestriez, B. Critical Roles of Binders and Formulation at Multiscales of Silicon-Based Composite Electrodes. *J. Power Sources* **2015**, *280*, 533–549.
- (43) Choi, N. S.; Yew, K. H.; Choi, W. U.; Kim, S. S. Enhanced Electrochemical Properties of a Si-Based Anode Using an Electrochemically Active Polyamide Imide Binder. *J. Power Sources* **2008**,

- 177, 590–594.
- (44) Wu, M.; Xiao, X.; Vukmirovic, N.; Xun, S.; Das, P. K.; Song, X.; Olalde-Velasco, P.; Wang, D.; Weber, A. Z.; Wang, L. W.; *et al.* Toward an Ideal Polymer Binder Design for High-Capacity Battery Anodes. *J. Am. Chem. Soc.* **2013**, *135*, 12048–12056.
- (45) Park, S.-J.; Zhao, H.; Ai, G.; Wang, C.; Song, X.; Yuca, N.; Battaglia, V. S.; Yang, W.; Liu, G. Side-Chain Conducting and Phase-Separated Polymeric Binders for High-Performance Silicon Anodes in Lithium-Ion Batteries. *J. Am. Chem. Soc.* **2015**, *137*, 2565–2571.
- (46) Kovalenko, I.; Zdyrko, B.; Magasinski, a.; Hertzberg, B.; Milicev, Z.; Burtovyy, R.; Luzinov, I.; Yushin, G. A Major Constituent of Brown Algae for Use in High-Capacity Li-Ion Batteries. *Science (80-.)*. **2011**, *334*, 75–79.
- (47) Choi, J.; Kim, K.; Jeong, J.; Cho, K. Y.; Ryou, M.-H.; Lee, Y. M. Highly Adhesive and Soluble Co-Polyimide Binder: Improving the Long-Term Cycle Life of Silicon Anodes in Lithium-Ion Batteries. *ACS Appl. Mater. Interfaces* **2015**, *7*, 14851–14858.
- (48) Jeena, M. T.; Lee, J.-I.; Kim, S. H.; Kim, C.; Kim, J.-Y.; Park, S.; Ryu, J.-H. Multifunctional Molecular Design as an Efficient Polymeric Binder for Silicon Anodes in Lithium-Ion Batteries. *ACS Appl. Mater. Interfaces* **2014**, *6*, 18001–18007.
- (49) Magasinski, A.; Zdyrko, B.; Kovalenko, I.; Hertzberg, B.; Burtovyy, R.; Huebner, C. F.; Fuller, T. F.; Luzinov, I.; Yushin, G. Toward Efficient Binders for Li-Ion Battery Si-Based Anodes: Polyacrylic Acid. *ACS Appl. Mater. Interfaces* **2010**, *2*, 3004–3010.
- (50) Ryou, M. H.; Kim, J.; Lee, I.; Kim, S.; Jeong, Y. K.; Hong, S.; Ryu, J. H.; Kim, T. S.; Park, J. K.; Lee, H.; *et al.* Mussel-Inspired Adhesive Binders for High-Performance Silicon Nanoparticle Anodes in Lithium-Ion Batteries. *Adv. Mater.* **2013**, *25*, 1571–1576.
- (51) Kwon, T.; Jeong, Y. K.; Lee, I.; Kim, T.-S.; Choi, J. W.; Coskun, A. Systematic Molecular-Level Design of Binders Incorporating Meldrum’s Acid for Silicon Anodes in Lithium Rechargeable Batteries. *Adv. Mater.* **2014**, *26*, 7979–7985.
- (52) Yim, T.; Choi, S. J.; Jo, Y. N.; Kim, T. H.; Kim, K. J.; Jeong, G.; Kim, Y. J. Effect of Binder Properties on Electrochemical Performance for Silicon-Graphite Anode: Method and Application of Binder Screening. *Electrochim. Acta* **2014**, *136*, 112–120.
- (53) Komaba, S.; Yabuuchi, N.; Ozeki, T.; Han, Z. J.; Shimomura, K.; Yui, H.; Katayama, Y.; Miura, T. Comparative Study of Sodium Polyacrylate and Poly(Vinylidene Fluoride) as Binders for High Capacity Si-Graphite Composite Negative Electrodes in Li-Ion Batteries. *J. Phys. Chem. C* **2012**, *116*, 1380–1389.
- (54) Koo, B.; Kim, H.; Cho, Y.; Lee, K. T.; Choi, N. S.; Cho, J. A Highly Cross-Linked Polymeric Binder for High-Performance Silicon Negative Electrodes in Lithium Ion Batteries. *Angew. Chemie - Int. Ed.* **2012**, *51*, 8762–8767.
- (55) Song, J.; Zhou, M.; Yi, R.; Xu, T.; Gordin, M. L.; Tang, D.; Yu, Z.; Regula, M.; Wang, D. Interpenetrated Gel Polymer Binder for High-Performance Silicon Anodes in Lithium-Ion Batteries. *Adv. Funct. Mater.* **2014**, *24*, 5904–5910.
- (56) Choi, S.; Kwon, T.; Coskun, A.; Choi, J. W. Highly Elastic Binders Integrating Polyrotaxanes for Silicon Microparticle Anodes in Lithium Ion Batteries. *Science (80-.)*. **2017**, *357*, 279–283.
- (57) Merla, Y.; Wu, B.; Yufit, V.; Brandon, N. P.; Martinez-Botas, R. F.; Offer, G. J. Novel Application of Differential Thermal Voltammetry as an In-Depth State-of-Health Diagnosis Method for Lithium-Ion Batteries. *J. Power Sources* **2016**, *307*, 308–319.
- (58) Xu, K. Electrolytes and Interphases in Li-Ion Batteries and Beyond. **2014**.
- (59) Ramos-Sanchez, G.; Soto, F. A.; Martinez de la Hoz, J. M.; Liu, Z.; Mukherjee, P. P.; El-Mellouhi, F.; Seminario, J. M.; Balbuena, P. B. Computational Studies of Interfacial Reactions at Anode Materials: Initial Stages of the Solid-Electrolyte-Interphase Layer Formation. *J. Electrochem. Energy Convers. Storage* **2016**, *13*, 031002.
- (60) Choi, J. W.; Aurbach, D. Promise and Reality of Post-Lithium-Ion Batteries with High Energy Densities. *Nat. Rev. Mater.* **2016**, *1*.
- (61) Wang, L.; Chen, B.; Ma, J.; Cui, G.; Chen, L. Reviving Lithium Cobalt Oxide-Based Lithium Secondary Batteries-toward a Higher Energy Density. *Chem. Soc. Rev.* **2018**.
- (62) Chen, Z.; Wang, C.; Lopez, J.; Lu, Z.; Cui, Y.; Bao, Z. High-Areal-Capacity Silicon Electrodes with Low-Cost Silicon Particles Based on Spatial Control of Self-Healing Binder. *Adv. Energy*

- Mater.* **2015**, n/a-n/a.
- (63) Wang, C.; Wu, H.; Chen, Z.; McDowell, M. T.; Cui, Y.; Bao, Z. Self-Healing Chemistry Enables the Stable Operation of Silicon Microparticle Anodes for High-Energy Lithium-Ion Batteries. *Nat. Chem.* **2013**, *5*, 1042–1048.
- (64) Yang, Z.; Zhang, J.; Kintner-meyer, M. C. W.; Lu, X.; Choi, D.; Lemmon, J. P. Electrochemical Energy Storage for Green Grid. *Chem. Rev.* **2011**, 3577–3613.
- (65) Armand, M.; Tarascon, J.-M. Building Better Batteries. *Nature* **2008**, *451*, 652–657.
- (66) Huggins, R. Lithium Alloy Negative Electrodes Formed from Convertible Oxides. *Solid State Ionics* **1998**, *113–115*, 57–67.
- (67) Wang, B.; Li, X.; Luo, B.; Hao, L.; Zhou, M.; Zhang, X.; Fan, Z.; Zhi, L. Approaching the Downsizing Limit of Silicon for Surface-Controlled Lithium Storage. *Adv. Mater.* **2015**, *27*, 1526–1532.
- (68) Sun, C.; Zhu, H.; Okada, M.; Gaskell, K.; Inoue, Y.; Hu, L. Interfacial Oxygen Stabilizes Composite Silicon Anodes. *Nano Lett.* **2015**, *15*.
- (69) Hassan, F. M.; Chabot, V.; Elsayed, A. R.; Xiao, X.; Chen, Z. Engineered Si Electrode Nanoarchitecture: A Scalable Postfabrication Treatment for the Production of next-Generation Li-Ion Batteries. *Nano Lett.* **2014**, *14*, 277–283.
- (70) Hassan, F. M.; Batmaz, R.; Li, J.; Wang, X.; Xiao, X.; Yu, A.; Chen, Z. Evidence of Covalent Synergy in Silicon-Sulfur-Graphene Yielding Highly Efficient and Long-Life Lithium-Ion Batteries. *Nat. Commun.* **2015**, *6*, 1–11.
- (71) Jeon, H.; Cho, I.; Jo, H.; Kim, K.; Ryou, M.-H.; Lee, Y. M. Highly Rough Copper Current Collector: Improving Adhesion Property between a Silicon Electrode and Current Collector for Flexible Lithium-Ion Batteries. *RSC Adv.* **2017**, *7*, 35681–35686.
- (72) Klamor, S.; Schröder, M.; Brunklaus, G.; Niehoff, P.; Berkemeier, F.; Schappacher, F. M.; Winter, M. On the Interaction of Water-Soluble Binders and Nano Silicon Particles: Alternative Binder towards Increased Cycling Stability at Elevated Temperatures. *Phys. Chem. Chem. Phys.* **2015**, *17*, 5632–5641.
- (73) Han, Z.-J. Z. Z.-J. Z.-J.; Yabuuchi, N.; Hashimoto, S.; Sasaki, T.; Komaba, S. Cross-Linked Poly(Acrylic Acid) with Polycarbodiimide as Advanced Binder for Si/Graphite Composite Negative Electrodes in Li-Ion Batteries. *ECS Electrochem. Lett.* **2012**, *2*, A17–A20.
- (74) Wang, C.; Wu, H.; Chen, Z.; McDowell, M. T.; Cui, Y.; Bao, Z. Self-Healing Chemistry Enables the Stable Operation of Silicon Microparticle Anodes for High-Energy Lithium-Ion Batteries. *Nat. Chem.* **2013**, *5*, 1042–1048.
- (75) Piper, D. M.; Yersak, T. A.; Son, S. B.; Kim, S. C.; Kang, C. S.; Oh, K. H.; Ban, C.; Dillon, A. C.; Lee, S. H. Conformal Coatings of Cyclized-PAN for Mechanically Resilient Si Nano-Composite Anodes. *Adv. Energy Mater.* **2013**, *3*, 697–702.
- (76) Piper, D. M.; Evans, T.; Leung, K.; Watkins, T.; Olson, J.; Kim, S. C.; Han, S. S.; Bhat, V.; Oh, K. H.; Buttry, D. A.; *et al.* Stable Silicon-Ionic Liquid Interface for next-Generation Lithium-Ion Batteries. *Nat. Commun.* **2015**, *6*, 6230.
- (77) Miyachi, M.; Yamamoto, H.; Kawai, H.; Ohta, T.; Shirakata, M. Analysis of SiO Anodes for Lithium-Ion Batteries. **2005**, 2089–2091.
- (78) Yasuda, K.; Kashitani, Y.; Kizaki, S.; Takeshita, K.; Fujita, T.; Shimosaki, S. Thermodynamic Analysis and Effect of Crystallinity for Silicon Monoxide Negative Electrode for Lithium Ion Batteries. *J. Power Sources* **2016**, *329*, 462–472.
- (79) Zhao, H.; Lu, P.; Jiang, M.; Song, X.; Zheng, Z.; Zhou, X.; Fu, Y.; Xiao, X.; Liu, Z.; Battaglia, V. S.; *et al.* Toward Practical Application of Functional Conductive Polymer Binder for a High-Energy Lithium-Ion Battery Design Toward Practical Application of Functional Conductive Polymer Binder for a High-Energy Lithium-Ion Battery Design. **2014**.
- (80) Kajita, T.; Yuge, R.; Nakahara, K.; Iriyama, J.; Takahashi, H.; Kasahara, R.; Numata, T.; Serizawa, S.; Utsugi, K. Improvement in Cycle Performance and Clarification of Deterioration Mechanism of Lithium-Ion Full Cells Using SiO Anodes. *J. Electrochem. Soc.* **2013**, *160*, A1806–A1810.
- (81) Shi, L.; Pang, C.; Chen, S.; Wang, M.; Wang, K.; Tan, Z.; Gao, P.; Ren, J.; Huang, Y.; Peng, H.; *et al.* Vertical Graphene Growth on SiO Microparticles for Stable Lithium Ion Battery Anodes. *Nano Lett.* **2017**, *17*, 3681–3687.

- (82) Lu, Y.; Tu, Z.; Archer, L. a. Stable Lithium Electrodeposition in Liquid and Nanoporous Solid Electrolytes. *Nat. Mater.* **2014**, *advance on*, 1–9.
- (83) Qian, J.; Henderson, W. a.; Xu, W.; Bhattacharya, P.; Engelhard, M.; Borodin, O.; Zhang, J.-G. High Rate and Stable Cycling of Lithium Metal Anode. *Nat. Commun.* **2015**, *6*, 6362.
- (84) Wood, K. N.; Noked, M.; Dasgupta, N. P. Lithium Metal Anodes: Toward an Improved Understanding of Coupled Morphological, Electrochemical, and Mechanical Behavior. *ACS Energy Lett.* **2017**, *2*, 664–672.
- (85) Cheng, X.-B.; Zhang, R.; Zhao, C.-Z.; Wei, F.; Zhang, J.-G.; Zhang, Q. A Review of Solid Electrolyte Interphases on Lithium Metal Anode. *Adv. Sci.* **2016**, *3*, n/a-n/a.
- (86) Cheng, X. B.; Zhang, R.; Zhao, C. Z.; Zhang, Q. Toward Safe Lithium Metal Anode in Rechargeable Batteries: A Review. *Chem. Rev.* **2017**, *117*, 10403–10473.
- (87) Hu, Q. The Renaissance of Lithium Metal: SolidEnergy’s Role in the Future of Lithium Batteries. *Nature* **2015**, *526*, Sponsor Feature.
- (88) Xu, W.; Wang, J.; Ding, F.; Chen, X.; Nasybulin, E.; Zhang, Y.; Zhang, J.-G. Lithium Metal Anodes for Rechargeable Batteries. *Energy Environ. Sci.* **2014**, *7*, 513.
- (89) Wood, K. N.; Kazyak, E.; Chadwick, A. F.; Chen, K.-H.; Zhang, J.-G.; Thornton, K.; Dasgupta, N. P. Dendrites and Pits: Untangling the Complex Behavior of Lithium Metal Anodes Through Operando Video Microscopy. *Submitt. to Energy Environ. Sci.* **2016**.
- (90) Chen, Q.; Geng, K.; Sieradzki, K. Prospects for Dendrite-Free Cycling of Li Metal Batteries. *J. Electrochem. Soc.* **2015**, *162*, A2004–A2007.
- (91) Harry, K. J.; Hallinan, D. T.; Parkinson, D. Y.; MacDowell, A. a; Balsara, N. P. Detection of Subsurface Structures underneath Dendrites Formed on Cycled Lithium Metal Electrodes. *Nat. Mater.* **2014**, *13*, 69–73.
- (92) Choudhury, S.; Mangal, R.; Agrawal, A.; Archer, L. A. A Highly Reversible Room-Temperature Lithium Metal Battery Based on Crosslinked Hairy Nanoparticles. *Nat. Commun.* **2015**, *6*, 10101.
- (93) Tung, S.-O.; Ho, S.; Yang, M.; Zhang, R.; Kotov, N. a. A Dendrite-Suppressing Composite Ion Conductor from Aramid Nanofibres. *Nat. Commun.* **2015**, *6*, 6152.
- (94) Kim, S.-H.; Choi, K.-H.; Cho, S.-J.; Kil, E.-H.; Lee, S.-Y. Mechanically Compliant and Lithium Dendrite Growth-Suppressing Composite Polymer Electrolytes for Flexible Lithium-Ion Batteries. *J. Mater. Chem. A* **2013**, *1*, 4949.
- (95) Tu, Z.; Choudhury, S.; Zachman, M. J.; Wei, S.; Zhang, K.; Kourkoutis, L. F.; Archer, L. A. Designing Artificial Solid-Electrolyte Interphases for Single-Ion and High-Efficiency Transport in Batteries. *Joule* **2017**, *1*, 394–406.
- (96) Lu, Q.; He, Y.-B.; Yu, Q.; Li, B.; Kaneti, Y. V.; Yao, Y.; Kang, F.; Yang, Q.-H. Dendrite-Free, High-Rate, Long-Life Lithium Metal Batteries with a 3D Cross-Linked Network Polymer Electrolyte. *Adv. Mater.* **2017**, 1604460.
- (97) Cheng, X. B.; Zhao, M. Q.; Chen, C.; Pentecost, A.; Maleski, K.; Mathis, T.; Zhang, X. Q.; Zhang, Q.; Jiang, J.; Gogotsi, Y. Nanodiamonds Suppress the Growth of Lithium Dendrites. *Nat. Commun.* **2017**, *8*, 1–9.
- (98) Zheng, J.; Engelhard, M. H.; Mei, D.; Jiao, S.; Polzin, B. J.; Zhang, J.-G.; Xu, W. Electrolyte Additive Enabled Fast Charging and Stable Cycling Lithium Metal Batteries. *Nat. Energy* **2017**, *2*, 17012.
- (99) Li, W.; Yao, H.; Yan, K.; Zheng, G.; Liang, Z.; Chiang, Y.-M.; Cui, Y. The Synergetic Effect of Lithium Polysulfide and Lithium Nitrate to Prevent Lithium Dendrite Growth. *Nat. Commun.* **2015**, *6*, 7436.
- (100) Choudhury, S.; Tu, Z.; Stalin, S.; Vu, D.; Fawole, K.; Gunceler, D.; Sundararaman, R.; Archer, L. A. Electroless Formation of Hybrid Lithium Anodes for Fast Interfacial Ion Transport. *Angew. Chemie - Int. Ed.* **2017**, *56*, 13070–13077.
- (101) Liang, X.; Pang, Q.; Kochetkov, I. R.; Sempere, M. S.; Huang, H.; Sun, X.; Nazar, L. F. A Facile Surface Chemistry Route to a Stabilized Lithium Metal Anode. *Nat. Energy* **2017**, *6*, 17119.
- (102) Basile, A.; Bhatt, A. I.; O’Mullane, A. P. Stabilizing Lithium Metal Using Ionic Liquids for Long-Lived Batteries. *Nat. Commun.* **2016**, *7*, 1–11.
- (103) Fan, X.; Chen, L.; Ji, X.; Deng, T.; Hou, S.; Chen, J.; Zheng, J.; Wang, F.; Jiang, J.; Xu, K.; *et al.* Highly Fluorinated Interphases Enable High-Voltage Li-Metal Batteries. *Chem* **2018**, *4*, 174–185.

- (104) Chen, S.; Zheng, J.; Mei, D.; Han, K. S.; Engelhard, M. H.; Zhao, W.; Xu, W.; Liu, J.; Zhang, J. G. High-Voltage Lithium-Metal Batteries Enabled by Localized High-Concentration Electrolytes. *Adv. Mater.* **2018**, *30*, 1–7.
- (105) Chen, S.; Zheng, J.; Yu, L.; Ren, X.; Engelhard, M. H.; Niu, C.; Lee, H.; Xu, W.; Xiao, J.; Liu, J.; *et al.* High-Efficiency Lithium Metal Batteries with Fire-Retardant Electrolytes. *Joule* **2018**, 1–11.
- (106) Jiao, S.; Ren, X.; Cao, R.; Engelhard, M. H.; Liu, Y.; Hu, D.; Mei, D.; Zheng, J.; Zhao, W.; Li, Q.; *et al.* Stable Cycling of High-Voltage Lithium Metal Batteries in Ether Electrolytes. *Nat. Energy* **2018**, 1–8.
- (107) Fan, X.; Chen, L.; Borodin, O.; Ji, X.; Chen, J.; Hou, S.; Deng, T.; Zheng, J.; Yang, C.; Liou, S. C.; *et al.* Non-Flammable Electrolyte Enables Li-Metal Batteries with Aggressive Cathode Chemistries. *Nat. Nanotechnol.* **2018**, 1–8.
- (108) Lin, D.; Liu, Y.; Liang, Z.; Lee, H.-W.; Sun, J.; Wang, H.; Yan, K.; Xie, J.; Cui, Y. Layered Reduced Graphene Oxide with Nanoscale Interlayer Gaps as a Stable Host for Lithium Metal Anodes. *Nat. Nanotechnol.* **2016**, 1–8.
- (109) Cheng, X.-B.; Peng, H.-J.; Huang, J.-Q.; Wei, F.; Zhang, Q. Dendrite-Free Nanostructured Anode: Entrapment of Lithium in a 3D Fibrous Matrix for Ultra-Stable Lithium-Sulfur Batteries. *Small* **2014**, n/a-n/a.
- (110) Lin, D.; Zhao, J.; Sun, J.; Yao, H.; Liu, Y.; Yan, K.; Cui, Y. Three-Dimensional Stable Lithium Metal Anode with Nanoscale Lithium Islands Embedded in Ionically Conductive Solid Matrix. *Proc. Natl. Acad. Sci.* **2017**, *114*, 4613–4618.
- (111) Zhang, Y.; Luo, W.; Wang, C.; Li, Y.; Chen, C.; Song, J.; Dai, J.; Hitz, E. M.; Xu, S.; Yang, C.; *et al.* High-Capacity, Low-Tortuosity, and Channel-Guided Lithium Metal Anode. *Proc. Natl. Acad. Sci.* **2017**, *114*, 3584–3589.
- (112) Ye, H.; Xin, S.; Yin, Y. X.; Li, J. Y.; Guo, Y. G.; Wan, L. J. Stable Li Plating/Stripping Electrochemistry Realized by a Hybrid Li Reservoir in Spherical Carbon Granules with 3D Conducting Skeletons. *J. Am. Chem. Soc.* **2017**, *139*, 5916–5922.
- (113) Yan, K.; Lu, Z.; Lee, H.-W.; Xiong, F.; Hsu, P.-C.; Li, Y.; Zhao, J.; Chu, S.; Cui, Y. Selective Deposition and Stable Encapsulation of Lithium through Heterogeneous Seeded Growth. *Nat. Energy* **2016**, *1*, 16010.

VITA

Qingquan Huang

Qingquan Huang (QQ) was born in Huangshan City, Anhui, China on Aug 27th 1989. He attended Tsinghua University in 2008, where he received a Bachelor of Science in Chemistry in June 2012. After graduation, he had one gap year doing research in Dr. Xun Wang's group from Tsinghua University. Then QQ continued to pursue a PhD degree in the Department of Materials Science and Engineering at the Pennsylvania State University. He soon began his graduate studies under the guidance of Dr. Donghai Wang in August of 2013. In his following years at Penn State, he focused his research on high-capacity Si-based anode material, including design of various polymer binders, design of elastic polymer cushion for stable SiO anode, synthesis of carbon coated SiO anode, and blending it with graphite anode. He also worked on fabrication of large-format pouch types cells for several DOE projects.